Onshore sandbar migration in the nearshore

Henriquez, Martijn

DOI
10.4233/uuid:be7a3374-0349-4b9d-a9e5-8c8a98ffeb24

Publication date
2019

Document Version
Final published version

Citation (APA)
Henriquez, M. (2019). *Onshore sandbar migration in the nearshore*. [Dissertation (TU Delft), Delft University of Technology]. https://doi.org/10.4233/uuid:be7a3374-0349-4b9d-a9e5-8c8a98ffeb24

Onshore sandbar migration in the nearshore

Onshore sandbar migration in the nearshore

Dissertation

for the purpose of obtaining the degree of doctor
at Delft University of Technology
by the authority of the Rector Magnificus prof. dr. ir. T.H.J.J. van der Hagen
chair of the Board for Doctorates
to be defended publicly on
Thursday 5 December 2019 at 10:00 o'clock

by

Martijn HENRIQUEZ

Master of Science in Civil Engineering, Delft University of Technology, the Netherlands
born in Willemstad, Curaçao

This dissertation has been approved by the promotors.

Composition of the doctoral committee:

Rector Magnificus,	chairman
Prof. dr. ir. M.J.F. Stive	Delft University of Technology, promotor
Prof. dr. ir. A.J.H.M. Reniers	Delft University of Technology, promotor

Independent members:

Prof. dr. ir. J.A. Roelvink	IHE Delft Institute for Water Education
Prof. dr. J.D. Pietrzak	Delft University of Technology
Prof. dr. D.F. Foster	University of New Hampshire, USA
Dr. H.M. Schuttelaars	Delft University of Technology

Other members:

Prof. dr. B.G. Ruessink	Utrecht University

Keywords: nonlinear waves, wave bottom boundary layer, bottom shear stress, sediment transport

Print: Ridderprint | www.ridderprint.nl

Cover: Nata Alhontess, Shutterstock, www.shutterstock.com

. . . and one day closer to death

Pink Floyd

Acknowledgements

It's a while ago when this adventure started. Who I am today is because of the challenges and, more important, the people met along the way.

Two key persons who are responsible for the creation of this adventure are Marcel Stive and Ad Reniers. They gave me the opportunity and helped me out writing the proposal for a STW grant. Marcel always provided the environment for scientific creativity and professional growth. Ad demonstrated, by example, life's added value of hospitality. Staying over at the lovely Reniers family and BBQs during field experiments (remember ECORS?) are just a few examples of the many. Thank you both for all your guidance and patience.

The first few years I shared a stable and tranquil working atmosphere with Marije Smit who gave me support as roommate and friend. I am happy to see that we are now both enjoying the family life.

One full year was spent in the water lab working in the wave flume. Doing state-of-the-art experiments requires dedicated staff who need to deal with demanding scientists. Sander de Vree and Jaap van Duin always thought along with me on the problems encountered and made the experiment a success.

Part of the job is being stuck. Getting unstuck means knocking on some doors. Luckily, the doors of Judith Bosboom and Gerben de Boer were always open to pick their brains. Thank you for sharing.

After a room shuffle I ended up in a working atmosphere shuffle. Tranquility was replaced by noise and energy. Chewbacca (Chu Au), Sield and Matt were a mix of no other. These vibrant times are an inspiration for life. Thank you Chu for taking us to your home town in China. Sield for being Sierd. And Matthieu for always being there (no, not in the room).

During my time I had the opportunity to participate in many (field) experiments. I cannot think of a more educative experience for a student in terms of fun, subject matter and collaboration. Thanks Jamie, Ad, Edie, Ed, Jeff, Jenna, Diane, Meagan and Sylvia.

There are many that left an imprint on me, among others, Jaap van Thiel de Vries, Ronald Brouwer, Wim Kanning, Nicolette Volp, Roeland de Zeeuw, Tim Janssen, Joao Mill Homens, the MSc students,... In particular, Saulo Meirelles, who challenged my supervising skills and provided my life motto 'everyday is one day closer to death' which get my bearings going!

A special thanks to my wife Reina who put up with this PhD project for way too many years. Her devotion to form a stable family has allowed me to finish the project. Thank you family and friends, your support has kept me sane.

Martijn Henriquez
May 2019

Summary

This thesis is about the hydrodynamic processes that occur when a nearshore sandbar migrates towards the shore driven by the waves. These processes are relevant because process-based morphological models have difficulty simulating coastal accretion events in contrast to erosion events. Simulating accretion events is important for engineering purposes, for example, to optimize shoreface nourishment for the conservation of beach and dunes of the Netherlands. During onshore sandbar migration, sediment is dominantly transported at the bed where the orbital wave motion applies friction on the bed. This transport, known as bedload, may result in a cross-shore net transport due to various hydrodynamic processes. First off, the orbital motion under waves in the nearshore are not sinusoidal but asymmetric as waves have steep fronts and flat backs. The wave shape is reflected back in the orbital motion which has two consequences, first, the largest flow velocities are found under the wave crests, and second, the largest horizontal pressure gradients are found under the wave fronts. Numerical modeling results have shown that in the wave bottom boundary layer the shape of the orbital motion is altered due to flow deceleration. However, there have not been any observations to validate this. Another set of hydrodynamic processes are the time-averaged currents generated by the waves. In the wave bottom boundary layer these processes are 'progressive wave streaming' and 'wave shape streaming'. In addition, mass flux by waves (Stokes drift) and wave breaking processes also generate currents that have an affect on the time-averaged bottom shear stress. Although the time-averaged bed shear stress is relatively small compared to the time-varying component it may have a large impact on the net sediment transport. The accumulative effect of the aforementioned processes on the time-averaged bed shear stress is not well understood.

The hydrodynamic processes near the bed are difficult to research for several reasons: the small thickness of the wave bottom boundary layer, the proximity to the bed and the harsh environment of the nearshore. In this thesis we study these processes by conducting a laboratory wave flume experiment with observation of the flow in the wave bottom boundary layer (Chapter 2). The laboratory wave flume experiment had a rigid bottom with a single bar profile. The wave field was regular and corresponded with conditions that would force the bar onshore. Observations of the flow velocity were obtained using Particle Image Velocimetry. The measurement resolution was large enough to clearly observe the flow structure of the wave bottom boundary layer. The turbulent flow properties were obtained by ensemble averaging. In addition, vortex tubes were observed.

For the analysis of the observations we first focused on the time-varying part (Chapter 3). The bed shears stresses were derived by integrating the fluid shear stress over the 'interfacial sublayer' which is located between the crest and trough of the bottom roughness elements. From the flow observations it was evident that free-

stream velocity was transformed in the wave bottom boundary layer by becoming less asymmetric and more skewed. To study the relation between the free-stream orbital velocity and the bed shear stress the harmonics of the time series were analyzed (i.e. frequency analysis). It was found that, for every individual harmonic, the relation can be described the analytic boundary layer solution for laminar flow. However, the phase leads of the friction velocity components (w.r.t. the free-stream velocity components) were approximately 37 degrees instead of the theoretical 45 degrees, which may be related to the fact that the bed was not smooth. A similar exercise was performed on numerical modeling results of oscillatory boundary layer flow where the flow was turbulent. It appeared that the relation between free-stream velocity and bed shear stress is not quadratic and is closer to $\tau_b \sim u^{1.6}$. However, when the quadratic assumption is applied, the error made in the skewness of the bed shear stress was relatively small. Furthermore, to describe the time-series of the surface elevation or horizontal velocity of a single wave, Abreu et al. (2010) suggested a waveform parameterization where the signal asymmetry and skewness are related to the harmonic amplitudes and phases. The frequency analysis from the experimental observations also describe this relation indicating the validity of the waveform parameterization for regular waves in the nearshore.

In Chapter 4 the time-averaged currents and bed shear stresses were analyzed. The relation between net bedload and the bed shear stress was investigated by looking at the moments of the bed shear stress. Also, an analytic model was utilized to aid in the interpretation of the vertical profiles of the horizontal velocity. From the observations it was clear that the currents in the wave bottom boundary layer have a complex vertical structure and consequently the free-stream velocity was not a good proxy for the bed shear stress. The time-averaged bed shear stresses were maximal and directed onshore at the bar crest where they contributed 20% to the stress moment that is responsible for the bedload. By comparing the observations with modeling results it appeared that the analytic model was unable to reproduce the time-averaged velocity profiles when the flow was turbulent owing to the process of 'wave shape streaming' which was not incorporated in the analytic model.

The findings of this study were elucidated by applying them to a real-scale example of an onshore sandbar migration. Often, the example of the Duck94 onshore sandbar migration is choosen. However, the use of the Duck94 example is not straightforward because the onshore sandbar migration is an accumulation of different transport patterns over a tidal cycle. Therefore, we used the large-scale wave flume experiment LIP11d Test 1c were the still water level was constant. Through this example we illustrated the implementation our findings and confirm the importance thereof. In addition, it was found that wave dissipation is currently not modeled with sufficient accuracy to successfully model onshore sandbar migration.

Samenvatting

Dit proefschrift gaat over de hydrodynamische processen die zich voordoen wanneer een zandbank naar de kust toe gedreven wordt door de golven. Deze processen zijn relevant omdat proces gebaseerde morfologische modellen problemen hebben met het simuleren van kust aangroei in tegenstelling tot kusterosie. Het simuleren van kust aangroeiende gebeurtenissen is belangrijk voor technische doeleinden, bijvoorbeeld, om vooroeversuppleties te optimaliseren voor het behoud van stranden en duinen van Nederland. Tijdens de kustwaartse migratie van zandbanken, wordt sediment overwegend getransporteerd nabij de bodem, waar de orbitaalbeweging van de golven wrijving op de bodem uitoefent. Dit transport, bekend als bedload, kan resulteren in een netto sediment transport door verschillende hydrodynamische processen. Zo is de orbitaalbeweging onder golven nabij de kust niet sinusvormig maar asymmetrisch waarbij golven steile fronten en flauwe ruggen hebben. De golfvorm wordt teruggezien in de orbitaalbeweging met twee gevolgen, ten eerste, de grootste stroomsnelheden bevinden zich onder de golftoppen en ten tweede, de grootste horizontale drukgradiënten bevinden zich onder de golffronten. Numerieke model resultaten hebben aangetoond dat in de bodemgrenslaag de vorm van de orbitaalbeweging wordt gewijzigd als gevolg van stroomvertraging. Echter, tot op heden waren er geen gedetailleerde waarnemingen om dit te valideren. Een andere set van hydrodynamische processen zijn de tijdsgemiddelde stromingen door golven. In de bodemgrenslaag zijn dit de processen 'progressive wave streaming' en 'wave shape streaming'. Bovendien genereren Stokes drift (massa flux van golven) en golfbrekende processen ook stromen die een effect hebben op de tijdsgemiddelde bodemschuifspanning. Hoewel de tijdsgemiddelde bodemschuifspanning relatief klein is, in vergelijking met de tijdsvariërende component, kan deze een grote invloed hebben op het netto sedimenttransport. Het cumulatieve effect van de bovengenoemde processen op de tijdsgemiddelde bodemschuifspanning wordt nog niet goed begrepen.

De hydrodynamische processen in de buurt van de bodem zijn om verschillende redenen moeilijk te onderzoeken: de kleine dikte van de bodemgrenslaag, de nabijheid van de bodem en de ruige omgeving van de kust. In dit proefschrift bestuderen we deze processen door in een golfgoot van een laboratorium een experiment uit te voeren met observaties van de stroming in de bodemgrenslaag (hoofdstuk 2).

Het laboratorium-golfgoot experiment had een vaste bodem met een profiel van een zandbank. Het golfveld was regelmatig en correspondeerde met omstandigheden die de bank landwaarts dwingen. Waarnemingen van de stroomsnelheden werden verkregen met behulp van Particle Image Velocimetry. De meetresolutie was groot genoeg om de structuur van de stroom in de bodemgrenslaag duidelijk waar te nemen. De turbulente stroomeigenschappen werden verkregen door middeling van een ensemble. In de bodemgrenslaag werden werden vortices waargenomen.

Voor de analyse van de waarnemingen hebben we ons eerst geconcentreerd op het

tijdsvariërende deel (hoofdstuk 3). De bodemschuifspanningen werden afgeleid door de vloeistof schuifspanningsgradienten te integreren over de sublaag die zich bevindt tussen de toppen en dalen van de ruwheidselementen op de bodem. Uit de waarnemingen was het duidelijk dat de vrije stroomsnelheid werd getransformeerd in de bodemgrenslaag waardoor de orbitaalbeweging minder asymmetrisch werd. Om de relatie tussen de vrije stroomsnelheid en de bodemschuifspanning te bestuderen, zijn de harmonische van de tijdreeksen geanalyseerd (i.e. frequentieanalyse). Het bleek dat voor elke afzonderlijke harmonische component de relatie kan worden beschreven met de analytische grenslaagoplossing voor laminaire stroming. De fasen verschillen van de wrijvingssnelheid componenten ten opzichte van de vrije-stroom snelheidscomponenten waren ongeveer 37 graden in plaats van de theoretische 45 graden, wat in verband kan staan met het feit dat de bodem niet glad was. Een vergelijkbare oefening is uitgevoerd op numerieke modelresultaten van de oscillerende bodemgrenslaag waarbij de stroming turbulent was. Het bleek dat de relatie tussen de vrijestroomsnelheid en bodemschuifspanning niet kwadratisch is maar dichter bij $\tau_b \sim u^{1.6}$ lag. Echter, wanneer de kwadratische aanname wordt toegepast, was de fout die werd gemaakt in de skewness van de bodemschuifspanning relatief klein. Daarnaast, voor het beschrijven van de tijdreeksen van de oppervlakte uitwijking of de horizontale snelheid van een enkele golf suggereerde Abreu et al. (2010) een golfvorm parametrisering waar de asymmetrie en scheefheid van het signaal gekoppeld zijn aan de harmonische amplituden en fasen. De frequentieanalyse van de experimentele waarnemingen beschrijven een vergelijkbare relatie wat de geldigheid van de golfvorm parametrisering bevestigd voor regelmatige golven nabij de kust.

In hoofdstuk 4 zijn de tijdsgemiddelde stromen en bodemschuifspanningen geanalyseerd. De relatie tussen de netto bedload en de bodemschuifspanning is onderzocht door te kijken naar de (wiskundige) momenten van de bodemschuifspanning. Ook werd een analytisch model gebruikt om te helpen bij de interpretatie van de verticale profielen van de horizontale stroomsnelheid. Uit de waarnemingen was het duidelijk dat de stromingen in de bodemgrenslaag een complexe verticale structuur hadden en daardoor was de vrije stroomsnelheid geen goede proxy voor de bodemschuifspanning. De tijdsgemiddelde bodemschuifspanningen waren maximaal en kustwaarts gericht boven de top van de bank waar ze 20% bijdroegen aan het moment van de bodemschuifspanning dat verantwoordelijk was voor de bedload. Door de waarnemingen te vergelijken met de modelresultaten bleek dat het analytische model niet in staat was om de tijdsgemiddelde snelheidsprofielen te reproduceren wanneer de stroming turbulent was, wat mogelijk te wijten is aan het feit dat het 'wave shape streaming' proces niet was meegenomen in het analytische model.

De bevindingen van deze studie werden verduidelijkt door ze toe te passen op een echt voorbeeld van een kustwaartse zandbank migratie. Vaak wordt het voorbeeld van de Duck94 kustwaartse zandbank migratie gekozen. Echter, het gebruik van het Duck94 experiment is niet eenvoudig, omdat de kustwaartse zandbank migratie een opeenstapeling is van verschillende transport patronen over een getijdencyclus. Daarom is hier het LIP11d Test 1c experiment gebruikt waar het waterniveau constant was. Met dit voorbeeld hebben we de implementatie van onze bevindingen geïllustreerd en het belang ervan aangetoond. Daarnaast is vastgesteld dat momenteel

de golf dissipatie onvoldoende nauwkeurig gemodelleerd wordt om met succes een kustwaartse zandbankmigratie te modelleren.

Contents

1

Introduction

1.1. General

This thesis is about shoreward transport of sand by unbroken waves near the shore. A typical sandy shore is often made out of a beach and dune. On a prograding coastline, sediments are transported by wave-induced currents to the shoreline where after the wind blows the sediments into the dune. Many sandy shores provide safety by functioning as a barrier against storm surges and waves. In the Netherlands, 60% of the population lives below sea level who are protected against the sea by a barrier of sandy shores and dunes. On a global scale, many coastal cities (e.g. New York city) rely on the protection of sandy shores against high surges and large waves from storms, hurricanes and cyclones (Hallegatte et al., 2013). However, coastal areas are under increased pressure due to climate change effects such as sea level rise and larger storms.

Rising sea levels force the beach profile to follow upwards and this requires sediments which are sourced from the beach-dune system. This phenomenon can turn a stable coastline into an eroding coastline. To prevent coastal erosion, in e.g. the Netherlands, the beach-dune system is nourished with million cubes of sand close to shore at depths between 5 and 8 m. From experience, we know that the nourished sand is distributed over the beach and dunes by waves, tide and wind (Hillen and Roelse, 1995). However, This involves many transport processes which, at the moment, we cannot accurately predict. One critical process is the shoreward sediment transport by the waves. A better prediction would result in improved nourishment design and planning and thus reduced cost and increased safety.

1.2. Shoreward sediment transport by waves

1.2.1. Waves and currents

When waves travel through the water, the fluid particles underneath the surface make an orbital motion (see Figure 1.1). The fluid particle experiences a displacement moving 'back and forth' and 'up and down'. Thus, the fluid particle has a

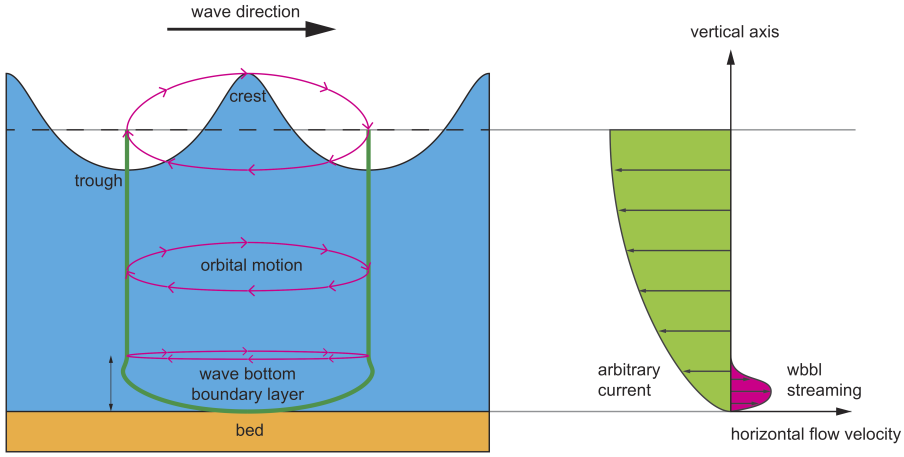

Figure 1.1: Orbital wave motion and currents under a progressive no-breaking wave.

periodic horizontal velocity, denoted with u, and a periodic vertical velocity, denoted with w, that are 90 degrees out of phase of each other. Under the wave crest we find the maximum onshore-directed velocity and under the wave trough we find the maximum offshore-directed velocity. The vertical excursion of the orbital motion will become zero at the bed.

At the bed, friction decelerates the fluid. The layer of decelerated fluid is less than a few centimeters thick and is called the 'wave bottom boundary layer' (wbbl). The friction force between the bed and the fluid is referred to as the 'bed shear stress'.

Besides the intra-wave orbital motion, progressive waves generate various types of time-averaged currents (see also Figure 1.1):

1. A relatively small net current in the wbbl commonly referred to as wbbl streaming (Longuet-Higgins, 1953; Trowbridge and Madsen, 1984). This current is result of a non-zero wave-averaged downward transport of horizontal momentum into the wave boundary layer by the vertical orbital motion which is characteristic for progressive surface waves.

2. There is another mechanism that actually drives a wbbl current against the wave direction that is coined wave shape streaming (Kranenburg et al., 2012). As the name indicates, the process is related to the wave shape which is non-sinusoidal in the nearshore (more on wave shapes will follow in Section 1.2.3. Bed friction in combination with a non-sinusoidal oscillatory water motion leads to a nonzero time-averaged wave-related turbulent stress, which drives a current in the wbbl against the direction of wave propagation(Holmedal and Myrhaug, 2009; Kranenburg et al., 2012; Trowbridge and Madsen, 1984).

3. Accompanied with the free-stream orbital motion of progressive surface waves is a mass flux in the direction of wave propagation referred to as Stokes drift (Phillips, 1977; Stokes, 1851). In case of a closed boundary, such as a shore, a return flow must exist.

4. In addition to the above mentioned currents there is the undertow and rip currents (see e.g. Dalrymple et al., 2011) associated with breaking waves which fall outside the scope of this study.

1.2.2. Sediment transport

In this study we consider sediment transport as the movement of sand particles over the horizontal space. Hereby, the particles can either be suspended in the water and move with the flow, or, the particles can roll along the bed. The first mode of transport is called 'suspended load' and the latter is called 'bedload' (Bagnold, 1966). In essence, during suspended load, sand particles are kept in suspension by turbulent fluid motions and carried along with the main flow. During bedload, sand particles are shoved over the bed by the shearing of the fluid over the bed.

Under *unbroken* waves, the fluid turbulence above the wbbl is small and hence, there is no mechanism to keep sand in suspension, however, the shearing of the orbital flow over the bed is strong enough to generate bedload. Therefore, bedload is dominant over suspended load under unbroken waves.

The friction force between the fluid and the bed (hereafter called bed shear stress τ_b) is related to the square of the flow velocity:

$$\tau_b \sim u^2 \,. \tag{1.1}$$

Empirical findings from experiments, see for example Meyer-Peter and Müller (1948) and Wilson (1987), showed that bedload was related to the bed shear stress by

$$q \sim \tau_b^{1.5} \,. \tag{1.2}$$

Therefore, it is generally accepted that bedload q has a cubed (i.e. non-linear) relationship with the horizontal flow velocity u

$$q \sim u^3 \,. \tag{1.3}$$

Bagnold (1966) came to a similar conclusion based on a physically-based derivation. Note that this relation is based on knowledge from sediment transport by 'steady' flows such as rivers and, in the absence of contrary evidence, is also applied for sediment transport by the 'unsteady' orbital wave motion (see e.g. Bailard, 1981, 1982; Bailard and Inman, 1981; Bowen, 1980; Ribberink, 1998; Roelvink and Stive, 1989).

1.2.3. Onshore bar migration

The knowledge gap becomes apparent when we try to predict the shoreward migration of bars. On many natural sandy beaches we find bars close the shore. For

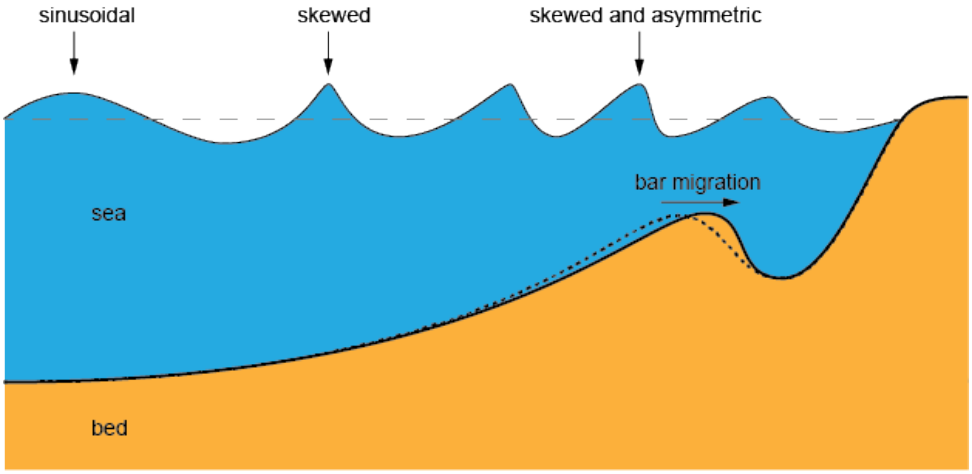

Figure 1.2: Onshore bar migration.

example, Figure 1.2 shows a coastal profile consisting of a single bar. Field observations suggest that these bars migrate shoreward when mildly-energetic unbroken waves travel over them (Aubrey, 1979; Ruessink et al., 2007a; Walstra et al., 2012; Wright and Short, 1984)

In order for the bar to migrate shoreward, the bar needs to erode on the seaward side and deposit on the shoreward side. In general, erosion happens when the sediment transport gradient is positive, and accretion when sediment transport gradient is negative. Two things can be deducted from the associated erosion and deposition pattern. First, the unbroken waves need to generate net transport, which means that more sand is transported shoreward than seaward during one orbital motion. Secondly, to comply with the associated erosion and deposition pattern, the net transport needs to have a local maximum over the bar crest.

A purely sinusoidal fluid motion can *not* generate any net transport since the shoreward part of the orbital motion is similar to the seaward part and the net result would be zero. However, waves are not sinusoidal near the shore. As waves start to feel the bed, their crest become sharper and troughs become flatter, i.e. the waves become 'skewed'. As waves travel into even shallower water depths, the waves become pitched forward, this is called 'asymmetry'. See the different wave shapes in Figure 1.2 for a visual impression. The periodic horizontal flow velocity u generated by the orbital motion has the same shape as the time evolution of the surface elevation and, therefore, will have similar skewness and asymmetry features. Skewed waves have the property that the shoreward velocity under the wave crest is larger than the seaward velocity under the wave trough. Wave asymmetry has no effect on the maximum and minimum velocity, instead, the shoreward flow accelerations become larger than the seaward flow accelerations. For an impression, see the three different velocity shapes in Figure 1.3 (shown by the black lines). Note that all three velocity signals have similar variance and that their averages are zero. However, the

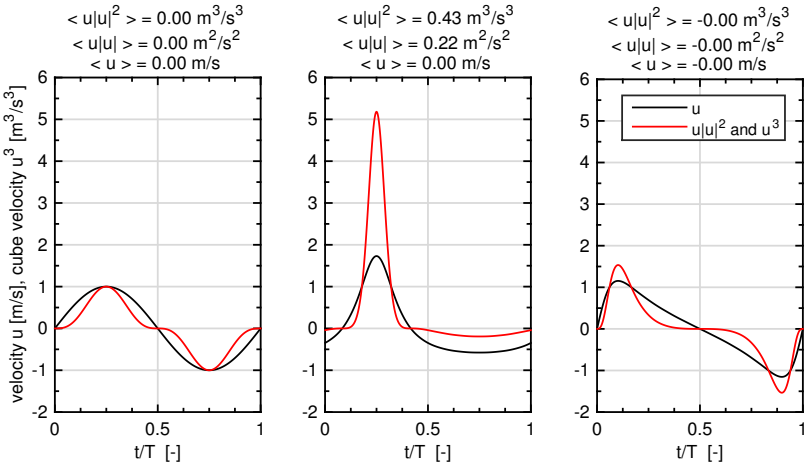

Figure 1.3: The velocity and cube velocity of a sinusoidal, skewed and asymmetric velocity signal. The titles show the first, second and third odd moments.

averaged of the cubed velocity is non-zero for the skewed signal and zero for the asymmetric signal.

During the field experiment 'Duck94' at Duck, North Carolina, USA, in 1994, an onshore bar migration was observed and the flow velocities were measured over the bar. Gallagher et al. (1998) used the measured velocities in combination with Equation 1.3 to predict the bar evolution. However, the observed onshore bar migration was not predicted. In the following section we provide a literature overview that sprouted from Gallagher et al. (1998) publication. Table 1.1 gives an overview of all the modeling attempts of the Duck94 onshore bar migration and can be a useful reference when going through the following literature.

1.2.4. Possible explanations

Pressure force by surface curvature

In 2003, Hoefel and Elgar succeeded in predicting the Duck94 onshore bar migration by including a proxy for the pressure force. The idea behind this is that the curvature of the water surface provides, besides the shearing force of fluid, also a pressure force that acts on the sediment grains. Since asymmetric waves have steeper fronts than backs, the pressure force could explain net sediment transport. Hoefel and Elgar (2003) used the flow acceleration as a proxy for the pressure force. This theory was, among others, based on the observations of a military diver (Madsen, 1974):

> Just prior to the passage of the crest of a near-breaking wave the bed seemed to explode.

Interestingly, the moment 'just prior to the passage of the crest' is at the upcrossing of the surface elevation. At that moment, the horizontal velocity by the orbital motion is zero and, based on Equation 1.3, one would not expect any sediment transport. Supported by the diver's observation and the findings of Flores and

Study	Method	Skill	Forcing	Findings	New questions
Gallagher et al. (1998)	Energetics	-0.1 (-0.23)	$u(t)$	Model was unable to predict onshore bar migration	What is the effect of fluid acceleration and phase lags between fluid and sediment?
Hoefel and Elgar (2003)	extended-energetics acceleration model (EEA)	0.80	$u(t)$	Including the flow acceleration in the energetic model predicts onshore bar migration	
Henderson et al. (2004)	2nd-order, single-phase, wave-resolving eddy-diffusive model (WRED), $k-\epsilon$ and 2nd-order sediment advection-diffusion equation	0.81	$u(t)$	Wbbl model predicts onshore bar migration on basis of bed shear stresses. Model had suspended load only. Shape of velocity changes in the wbbl. Boundary layer streaming and Stokes drift caused the onshore bar migration.	What is the effect on the bed shear stress due to the changing shape of the velocity in the wbbl? Is boundary layer streaming really that important? Or, was it the absence of bedload in the model?
Hsu et al. (2006)	Quasi-steady approach and Meyer-Peter and Müller (1948)(MPM)	0.34	$\widetilde{u}(t)$	Demeaned-velocity skewness and asymmetry have similar cross-shore variation during onshore bar migration. The comparisons of Duck94 model predictions are not sufficient to determine the dominant mechanisms of sediment transport.	What is the relation between the free-stream current and the instantaneous bed stress?
	1st-order WRED, mixing length closure and MPM	0.27	$\widetilde{u}(t)$		
	2nd-order WRED, mixing length closure and MPM	0.57	$\widetilde{u}(t)$		
	2nd-order WRED, $k-\epsilon$ and MPM	0.69	$\widetilde{u}(t)$		
	Additional impact free-stream current with quadratic friction law and MPM	-0.02	$\overline{u}(t)$		
	EEFF	0.25	$u(t), \widetilde{u}(t), \overline{u}(t)$		
Ruessink et al. (2007a)	Reniers et al. (2004a), Rienecker and Fenton (1981), MPM and nth-order time-averaged convection-diffusion equation	0.73	$H_{rms}, T_p, \theta_m, \overline{\eta}$	Onshore bar migration due to near-bed wave skewness and bedload transport with negligible effects of bound infragravity waves and near-bed streaming	
Dubarbier et al. (2015)	Reniers et al. (2004a), Abreu et al. (2010), Ruessink et al. (2012b), EEFF+EEA	0.93	$H_{rms}, T_p, \theta_m, \overline{\eta}$	Detailed inter-site comparison of best-fit model parameters shows large differences meaning that free parameters can compensate for missing physics.	
Fernández-Mora et al. (2015)	depth-averaged momentum balance, Abreu et al. (2010), Ruessink et al. (2012b), EEFF+EEA	0.82	$H_{rms}, T_p, \theta_m, \overline{\eta}$	Including either skewness or asymmetry delivers adequate skill. Including both is best for full profile.	

Table 1.1: Prediction of Duck94 between 1900 September 22 and 2200 September 27.

Sleath (1998a) and Drake and Calantoni (2001), Hoefel and Elgar (2003) argued that the pressure force played a crucial role in the transport of sediment.

Although from a physical point of view the pressure force could move sediment it does not explain the suspension event described by the diver in Madsen (1974). For a suspension event, water has to move around rapidly. Foster et al. (1994) suggested that coherent structures, known as 'vortex tubes', are generated in the wbbl and could be responsible for sediment suspension events. Carstensen et al. (2010) studied the structures in a oscillatory flow tunnel. Unfortunately, there are no measurements of vortex tubes under real waves.

Boundary layer streaming

Henderson et al. (2004) obtained similar results as Hoefel and Elgar (2003) while excluding the pressure force. Instead of using 'quasi steady' approximations such as Equation 1.3, they used a sophisticated numerical model to estimate the shearing force exerted by the fluid on the bed and combined it with a sediment advection-diffusion equation. This basically means that the sediment transport was modeled as 'suspended load' and the sediment concentration close to the bed was related to the shearing force of the fluid. From the model results Henderson et al. (2004) found that the shoreward bar migration was caused by 'wave boundary layer streaming'.

Kranenburg et al. (2013) developed a numerical model strongly similar to the one used by Henderson et al. (2004) but included feedback between turbulence and sediment concentration (stratification effects). Kranenburg et al. (2013) limited their study to sediment transport by skewed waves over a flat bed. Their findings support the relative importance of wbbl currents on net sediment transport. They found that wbbl streaming accounted for approximately 40% of the net sediment transport (when considering medium-sized sand). The other 60% of the net transport was due to the relatively larger sediment concentrations under the wave crest (compared to under the wave trough) caused by the fact that the oscillatory flow was skewed.

Henderson et al. (2004) found that the nearbed sediment transport correlated very well with the third moment of the nearbed velocity and poorly with the third moment of the velocity at the edge of the wbbl. Apparently when waves became asymmetric, the horizontal velocity close to the bed was more skewed than at the edge of the wbbl. In other words, the shape of the velocity signal changed in the wbbl and, therefore, the net sediment transport was actually related to the shape of the nearbed velocity instead of the free-stream velocity. Although an important observation, this was not the mechanism that migrated the bar shoreward. Henderson et al. (2004) remarked that this process was already noted by Nielsen (1992). Terrile et al. (2009b) further improved the description given by Nielsen (1992).

The mean current

Hsu et al. (2006) investigated, among others, the model of Gallagher et al. (1998), Hoefel and Elgar (2003) and Henderson et al. (2004). Hsu et al. (2006) showed that when only the free-stream wave orbital motion was considered (thus, no mean flow outside the wbbl) all models predicted the shoreward sandbar migration to some extent. Hsu et al. (2006) argued that the transport by the mean current outside the

wbbl and the wave orbital motion need to be estimated separately. Physically sound or not, this method basically sidelines the mean current. Since wbbl streaming, Stokes drift, wave skewness and wave asymmetry all had a local maximum over the bar crest, all models (although the underlying assumptions differ) predicted the Duck94 shoreward sandbar migration to some extend.

The argument of Hsu et al. (2006) is supported by the modeling efforts of Kranenburg et al. (2013) who showed that the return current outside the wbbl had a subordinate effect on the net transport by skewed waves. However, this was for cases were the free-stream current was smaller than 10% of the orbital velocity (Kranenburg et al., 2013).

Other modeling efforts

There are also modeling efforts of the Duck94 onshore bar migration where the model was forced by the offshore wave and water level conditions instead of the flow velocity measurements. This means that the currents forced by the waves need to be resolved. Under this category are the study by Ruessink et al. (2007a), Dubarbier et al. (2015) and Fernández-Mora et al. (2015). The hydrodynamics were modeled using the wave-averaged momentum and mass balance. The hydrodynamic model by Fernández-Mora et al. (2015) was depth-averaged while Ruessink et al. (2007a) and Dubarbier et al. (2015) used the quasi-3D flow model of Reniers et al. (2004a) to estimate the vertical velocity profile.

Ruessink et al. (2007a) estimated the intra-wave near-bed orbital velocity using the method of Rienecker and Fenton (1981) and only included wave skewness and no wave asymmetry. Dubarbier et al. (2015) and Fernández-Mora et al. (2015) estimated the intra-wave near-bed orbital velocity on the basis of the analytic wave form by Abreu et al. (2010) and used the parameterized estimates of wave skewness and asymmetry given by Ruessink et al. (2012a).

Ruessink et al. (2007a) estimated bedload with a Meyer-Peter Mueller power law (MPM) (Meyer-Peter and Müller, 1948), which is approximately similar to Equation 1.3. Dubarbier et al. (2015) and Fernández-Mora et al. (2015) estimated bedload with the extended energetics friction factor (EEFF) model of Hsu et al. (2006) in combination with the acceleration-driven bedload model of Hoefel and Elgar (2003). Note that the EEFF model of Hsu et al. (2006) is in essence also approximately similar to Equation 1.3, however, bedload by the mean current and orbital motion are considered separately.

All three models predicted the Duck94 onshore bar migration with good skill ranging from 0.73 to 0.93. The onshore bar migration could be modeled by either including wave skewness or asymmetry, however, including both works best for the whole cross-shore profile. Furthermore, free model parameters leave enough room to compensate for missing physics.

1.2.5. Status quo

All the aforementioned studies could not successfully pinpoint the dominant mechanisms of sediment transport during onshore bar migration (Dubarbier et al., 2015; Fernández-Mora et al., 2015; Hsu et al., 2006; Ruessink et al., 2007a). However, fo-

cused research questions can be formulated based on their findings and suggestions.

- Does the horizontal pressure gradient contribute to sediment transport (besides bed shear stress)?
- What is the relation between the periodic bed shear stress and the *nonlinear* orbital wave motion?
- How large is the time-averaged bottom shear stress due to mass flux, wave breaking, Longuet-Higgens streaming and wave shape streaming?

The onshore bar migration during the field experiment at Duck, North Carolina, USA, in 1994, was the only occurrence where the flow velocities and sediment concentrations were measured over a cross-shore transect that included the bar. Despite the close position of instruments to the bed, the measurements did not measure the flow in the wbbl. Therefore, the Duck94 data set cannot provide the answer to these research questions.

The absence of experimental data can be attributed to the difficulty of measuring them. The small wbbl thickness in combination with the rough environment of the nearshore make it difficult to conduct measurements. In addition, despite recent advances in acoustic measuring devices, there is no device commercially available that can measure flow velocities and/or sediment concentrations of the bedload with sub-millimeter spatial coverage (Chassagneux and Hurther, 2014).

The rough coastal environment can be avoided by resorting to the controlled environment of a laboratory wave flume. This does not solve the limitations imposed by the measuring devices. However, in clear water, i.e. without the obstruction of moving sediment particles, optical based techniques can adequately measure the flow velocities in the wbbl. A suitable optical-based technique called 'Particle Image Velocimetry' (Westerweel, 1993) has proven to measure instantaneous flow fields of small boundary layers (Lara et al., 2002; van der A et al., 2009, 2011).

In laboratory wave flumes the spatial dimensions are about a factor 10 smaller than in the field. When the waves become a factor of 10 smaller, the flow velocity will also become smaller and consequently sediment will not be moved. Alternatively, the sediment particles can be downscaled. However, when sediment particles become smaller their settling velocity also becomes smaller possibly changing the mode of transport from bedload to suspended load. For the study of intra-wave sediment transport it is essential to ensure that the laboratory model has the same transport regime as the prototype. The use of sediment that is made from a lighter material than sand can provide a solution. That way, the artificial sediment can be mobilized by the flow velocities in the model while the settling velocity is not compromised. Scale relations that are based on the dominant physical processes can provide the optimal material density and grain diameter for a certain coastal setting (Henriquez et al., 2008).

1.3. This research

1.3.1. Main objective

The main objective of this study is to investigate onshore bar migration and is restricted to the following research questions:

1. What is the relation between the periodic bed shear stress and the *nonlinear* orbital wave motion?

2. How large is the time-averaged bottom shear stress due to mass flux, Longuet-Higgins streaming and wave shape streaming?

1.3.2. Approach

To address the research questions data are required on near-bed free-stream flow velocities and bed shear stresses during an onshore bar migration. Bed shear stresses can be derived from detailed wbbl flow velocity measurements in the wbbl using the 'Particle Image Velocimetry' (PIV) technique (see e.g. van der A et al., 2011). However, repetition of the wave conditions are required to be able to ensemble average for the determination of intra-wave turbulent bed shear stresses. Such measurements need to be performed in the controlled environment of a laboratory wave flume where conditions can be repeated. Therefore, an experiment will be conducted in a laboratory wave flume with a fixed single-bar profile. The bottom profile and wave conditions are based on data from an onshore bar migration event that occurred during the mobile-bed wave-flume experiment described in Henriquez et al. (2008).

1.3.3. Outline

The fixed-bed wave flume experiment is presented in Chapter 2. In the experiment mild energetic waves were generated over a fixed bed with a single bar profile. Flow velocities were measured with sub-millimeter resolution in the wbbl using PIV.

Chapter 3 investigates the relation between the bed shear stress and the orbital wave motion. The focus is on the orbital shape of the free-stream velocity and bed shear stress. In addition to the data of laboratory wave flume tests, a k-ϵ numerical model was utilized to gain more insight in mechanics of the time-varying bed shear stresses. We tested the validity of the analytic boundary layer solution for laminar flow, the time-depended quadratic drag-law and a waveform expression.

Chapter 4 investigates the time-averaged bed shear stress under the regular surface waves that traveled over the fixed single bar profile in the laboratory wave flume. The focus was on the shoreward-directed wave Reynolds stress and the seaward-directed pressure force (to compensate the Stokes drift). A analytic quasi-1DV model was used as a tool to distinguish the relevant processes that govern the time-averaged bed shear stress.

In Chapter 5 (Synthesis) the findings are discussed and compared with other literature. Chapter 6 gives the conclusions and recommendations.

2

PIV measurements of the bottom boundary layer under nonlinear surface waves [1]

Sediment in the nearshore is largely mobilized in the wave bottom boundary layer (wbbl) hereby emphasizing the importance of this relatively thin layer to nearshore morphology. This paper presents a laboratory experiment where hydrodynamic properties of the wbbl were quantified by measuring flow velocities using Particle Image Velocimetry. The bottom of the wave flume was rigid with a single bar profile. The measurements consisted of the velocities of the wbbl with a resolution in the order of 10 points in time and space for skewed and asymmetric waves. In the wbbl there was significant transformation of velocity skewness and asymmetry. Negative wbbl streaming was generated by asymmetric waves. Boundary layer development and generation of vortex tubes were observed. The velocity measurements included the turbulent components resulting in quantification of turbulent stresses that were of similar magnitude as the viscous stresses.

2.1. Introduction

The orbital motion under surface waves in the nearshore is affected by bottom friction creating a wave bottom boundary layer (wbbl). The layer thickness ranges from a few millimeters to a few centimeters (Nielsen, 1992). The fluid forces on the bottom are the result of how momentum is transferred between the free-stream wave motion and the bottom. Accurate predictions of the bottom forces and flow properties are important for engineers and researchers since they mobilize and move

[1] This chapter has been published as: Henriquez, M., Reniers, A.J.H.M., Ruessink, B.G. and Stive, M.J.F., 2014. PIV measurements of the bottom boundary layer under nonlinear surface waves. Coastal Engineering, 94, pp.33-46. DOI: 10.1016/j.coastaleng.2014.08.004.

matter such as natural sediment and bottom protection elements, and impact the biotic environment (Koehl, 1982).

To date, uncertainties regarding flow properties of the unsteady wbbl, especially under non-linear surface waves, still exist, for example, the time evolution of the bottom shear stress over a non-linear wave cycle (Abreu et al., 2013; Mirfenderesk and Young, 2003; Nielsen, 1992; van der A et al., 2011). In a way, this is surprising, as the bottom shear stress is the basis for many sediment transport formulations (Ribberink, 1998; van Rijn, 2007). Besides viscous forces, momentum is transferred through the wbbl by turbulence and (lesser known) vortex tubes. These are all inter-related hydrodynamic processes that result in sediment transport. The associated transport gradients change the nearshore bathymetry and, under mild wave conditions, cause onshore sandbar migration (Gallagher et al., 1998; Kuriyama, 2002; Roelvink and Reniers, 1995; Ruessink et al., 2000; Sánchez-Arcilla et al., 2011). Numerous transport processes have been identified to explain these transport gradients (e.g., Berni et al., 2013b; Calantoni and Puleo, 2006; Drake and Calantoni, 2001; Flores and Sleath, 1998b; Foster et al., 1994, 2006; Henderson et al., 2004; Hoefel and Elgar, 2003; Hsu and Hanes, 2004; Kranenburg et al., 2013; Madsen, 1974; Terrile et al., 2009a), but a consensus among scientist remains off (Henderson et al., 2004; Hsu et al., 2006).

The time average flow by waves can be generated by three mechanisms (Kranenburg et al., 2012). The orbital motion of the free-stream causes a mass transport in the wave direction, known as Stokes drift (Phillips, 1977). On the basis of continuity there should be a time-averaged return flow. Closer to the bottom, in the wbbl, the vertical and horizontal velocity are not exactly in quadrature thereby generating a flow in the wave direction (Longuet-Higgins, 1953). Also in the wbbl, bottom generated turbulence under waves in the nearshore generate a flow against the wave direction (Trowbridge and Madsen, 1984). Kranenburg et al. (2012) appropriately coined the wbbl flows as 'progressive wave streaming' and 'wave shape streaming', respectively.

The bottom shear stresses by the unsteady orbital motion under nearshore waves are not as easy to predict as in steady flows. A quasi-steady assumption is often chosen where intra-wave bottom shear stresses are directly related to the square of the free-stream velocity (Ribberink, 1995; Ribberink and Chen, 1993; Ribberink et al., 2000). Henderson et al. (2004) and Berni et al. (2013b) show that this model excludes the wbbl process where free-stream velocity asymmetry is transformed into bottom velocity skewness, a process that can have a significant effect on net sediment transport. It is also hypothesized that horizontal pressure gradients found under the steep front faces of asymmetric waves mobilize sediment (Calantoni and Puleo, 2006; Drake and Calantoni, 2001; Flores and Sleath, 1998b; Foster et al., 2006; Hoefel and Elgar, 2003; Hsu and Hanes, 2004). This process is based on field and laboratory observations where sediment was mobilized during flow reversal under the wave front (Foster et al., 2006; Madsen, 1974). Also, vortex tubes, i.e. coherent flow structures that originate from instabilities generated at an inflectional-point of the flow (Akhavan et al., 1991; Carstensen et al., 2010; Foster et al., 1994), may contribute to the mobilization of sediment during flow reversal.

At the TU Delft an experiment was conducted to measure the processes mentioned above in the context to research onshore bar migration. This paper aims to present the data with a preliminary analysis to quantify and characterize these processes.

The experiment took place in a medium-sized laboratory wave flume. This type of facility correctly reproduces the free-stream flow structure under waves in the nearshore (Hughes, 1993). The bottom roughness was adjusted to approximate the turbulent flow properties found in the wbbl of the nearshore (Henriquez et al., 2008). The medium-sized laboratory flume was ideally suited for Particle Image Velocimetry (PIV) instrumentation. The challenging part is to get light (i.e. laser sheet) into the measuring domain. Lara et al. (2002) delivered the laser sheet from beneath the bottom through optically clear material. In this experiment a more practical, yet also more intrusive setup was chosen following Hofland and Booij (2004) and Schlicke et al. (2005) where the laser sheet was inserted into the water surface using a streamlined window. To mimic the nearshore, a single bar profile was built in the flume. Wave heights were adjusted to be maximum with the limitation of not breaking before the bar crest. Tests with three different wave periods were conducted to vary the nonlinearity of the waves.

The experiment is described in Section 2.2 and the data processing in Section 2.3. Data with preliminary analysis are presented in Section 2.4. Conclusions are presented in Section 2.5.

2.2. Description of experiments

2.2.1. Facility

The wave flume, located in the hydraulic laboratory of the Faculty of Civil Engineering and Geosciences at the Delft University of Technology in The Netherlands, has a length of 40 m, a width of 0.8 m and a height of 1.0 m. The piston-type wave maker is equipped with second-order steering and active reflection compensation. The bottom was an impermeable rigid single bar profile as shown in Figure 2.1. Sediment with a median grain diameter of $d_{50} = 520$ μm was glued to the bed to adjust the bottom roughness to yield turbulent conditions in the wbbl. The water depth h over the horizontal approach in the flume was 0.50 m; over the bar crest, it was 0.14 m.

2.2.2. Instruments

Flow velocities were estimated using Particle Image Velocimetry (PIV). The PIV system from LaVision consists of a control computer with DaVis 6 software, a Kodak ES1.0 camera (1008×1008 pixels) and a 50 mJ double New-Wave YAG laser. The camera was equipped with an extension tube and a Nikon Nikkor 105 mm lens. Double framed images were captured with a time of 450 μs between the frames. A laser sheet was inserted into the water surface without distortion by using a streamlined window. The setup is shown in Figure 2.2. The water was seeded with hollow glass spheres of 10 μm diameter. The reflections of particles in the light sheet were captured on camera which is positioned outside the transparent

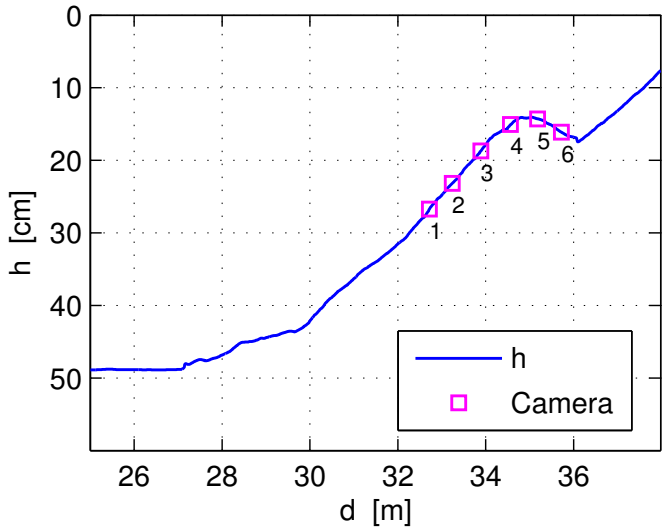

Figure 2.1: Bottom profile and camera locations. h denotes the water depth with respect to the still water level and d the distance from the wave board.

flume wall. The bed was painted fluorescent red and an optical filter was placed in front of the camera to diminish bed reflections of the light sheet. The camera was positioned at six cross-shore locations, four locations on the seaward side of the bar and 2 locations on the shoreward side of the bar (locations are shown in Figure 2.1 and are referred to as C1 to C6).

Surface elevations were measured using seven resistance type wave gauges with a sampling rate of 200 Hz. Three wave gauges were permanently positioned in the horizontal approach of the flume. Four wave gauges were positioned over the barred profile to record wave transformation. Their position depended on the camera location and could vary from test to test. One wave gauge was always co-located with the camera.

The bottom profile was measured with a Laser Displacement Sensor (LDS) from Micro-Epsilon (model: optoNCDT 1700). The LDS was mounted on a carriage that drove on tracks along the flume. Every 0.5 mm along the flume the output of the LDS was stored. This setup, considering some free movement and vibrations, allowed for a distance resolution of 0.5 mm.

2.2.3. Experimental program

Tests consisted of regular waves with periods of 1.0, 1.8 and 2.5 s and root-mean-square wave heights H_{rms} at the wave maker of 8.7, 8.4 and 8.0 cm, respectively. Using these wave conditions resulted in unbroken waves of similar wave height (H_{rms}) over the the bar crest. The wave skewness and asymmetry over the bar corresponded with those generally found in nature (Doering and Bowen, 1995).

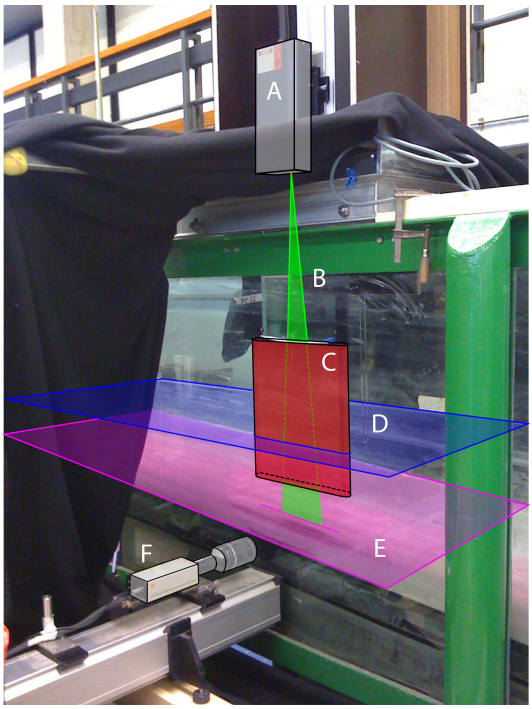

Figure 2.2: Experimental setup. The letter A denotes the laser generator, B the laser sheet, C the streamlined window, D the mean water surface, E the bottom and F the camera.

A test began by turning the wave maker on and starting the recording by the wave gauges. After 15 minutes (to reach stationary conditions in the flume) the camera took image pairs during a period of at least 10 waves (all these images together are called a set). Hereafter, the images were transferred from the random-access memory to the hard disk drive, which took several minutes. Then, the camera took eleven more sets during the test. Each test took about 1 hour to complete. In one test, the camera captured a minimum of 132, 120 and 120 waves for test with periods of 1.0, 1.8 and 2.5 s, respectively. The sampling rate of the camera was 15 Hz with the exception of tests with a wave period of 2.5 s for which the sampling rate was reduced to 10 Hz.

2.3. Data processing

2.3.1. Camera images

Image pairs consist of two grayscale images with 256 intensity levels. A background was generated by taking the mean image intensity of an image set. The background image was subtracted from every image to remove any permanent light source. The background image was also used to make a mask for areas in the images that correspond to the bottom or had significant reflections, see e.g. Figure 2.3. The intensity level of pixels that were in the mask were set to zero. The images were then processed with the PIV software package DaVis 6 from LaVision.

The PIV processing started with subdividing the image pairs in interrogation windows of 64×64 pixels. The windows had an overlap of 50%. The windows from the first image were cross-correlated with the windows of the second image to detect the average pixel displacement of the particles per window. Then, a consecutive cross-correlation was done but this time the window in the second image was shifted with the displacement result of the previous cross-correlation. This step was repeated two more times but with windows of 32×32 pixels.

The vector fields from the intermediate cross-correlations were checked using a minimum ratio of the first to the second highest correlation peak of $Q = 1.1$ and a median filter where vectors were removed if they exceeded 2 times the root-mean-square of neighbors. Removed vectors were replaced by interpolation and the field was smoothed with a Gaussian filter (filter window: 3×3 vectors). The vector fields of the final cross-correlation were also checked with an absolute allowed vector range and vectors with less than 3 neighbors were removed. Removed vectors were not interpolated. Vectors that were in the masked area were set to NaN (Not a Number).

The calibration factor to convert pixels to meters varied slightly between camera locations but was approximately 0.012 mm/pixel. Hence, the interrogation window of the final cross-correlation covered an area of 0.4 mm by 0.4 mm, the vector spacing was 0.2 mm, and the total image area amounted to 12 mm by 12 mm.

2.3.2. Wave gauges

During the tests the surface elevation η was recorded continuously. Only the parts where the PIV system was active were used. All parts were cropped to start and

end with a zero-down-crossing.

2.3.3. Ensemble averaging

A regular wave field can be seen as a repetition of similar waves in time t with a constant period T (primary harmonic). All these waves form the ensemble. Let α be any wave field variable such as the flow velocity or surface elevation and considered to be a function of time t. Then the ensemble average of α, denoted by $\widehat{\alpha}$, is calculated by

$$\widehat{\alpha}(t) = \frac{1}{N} \sum_{n=1}^{N} \alpha(t + (n-1)\,T) \qquad 0 \leq t < T \tag{2.1}$$

where N is the number of waves and n is the wave counter (see Section 2.2.3 for values of N). The wave field variable α can be divided in the following components:

$$\alpha = \overline{\alpha} + \widetilde{\alpha} + \alpha' \tag{2.2}$$

or

$$\alpha = \widehat{\alpha} + \alpha' \tag{2.3}$$

where $\overline{\alpha}$ is the time-average component, $\widetilde{\alpha}$ is the periodic component, $\widehat{\alpha}$ is the ensemble average component, and α' is the turbulent component.

There was a very small difference in clock running speed of the wave maker and the PIV system. This resulted in a gradual shift of sampling times with respect to the wave phases that was significant between the first and last set of a test (of the order of the turbulent fluctuations). Within one set of 10 waves, the drift was not significant and therefore the turbulent component was determined using the ensemble average component of the concerning set instead of the whole test. The drift was not significant for the time average and periodic component so these are averages over the whole test.

2.3.4. Spatial averaging and local coordinate system

Spatial averaging is denoted with angled brackets $\langle\ \rangle$. The bottom of the flume had a single bar profile and the PIV interrogation window included the bottom. Therefore, spatial averaging was done in the direction along the local bottom (and not the x-direction). The bottom slope was derived from the tilt of the ellipsoid made by the velocity vector of the primary harmonic of the velocity from tests with a period of 1.8 s at the center of the upper boundary of the PIV vector field. The primary harmonic was determined with the Fast Fourier Transform and the local bottom slope was assumed to be constant over the PIV interrogation window. The slope estimate derived from the flow agreed with the slope derived from the bottom profile measurements with the LDS. The estimates of the latter were not used because they had large deviations depending on the span over which the gradient was determined.

To accomplish averaging the rows, a rotated orthogonal grid was used consisting of grid lines normal and parallel to the bottom, see Figure 2.4. Linear interpolation

was used to estimate the vectors from the original grid to the rotated grid. The new grid corresponds with a local coordinate system where x is parallel to the local bottom, positive in the wave direction, and the z is normal to the local bottom and positive upward. x is zero at the left column of the rotated grid. z is zero at the maximum spatial-averaged intensity $\langle I \rangle$ of the background image. The vertical distance between $z = 0$ and the crests of protruding grains was approximately one d_{50}. The orientation of the coordinate system depended on the measurement location since the bottom slope was different at every location. The flow velocity vector was decomposed into the flow velocity u in the direction of x, and the flow velocity w in the direction of z.

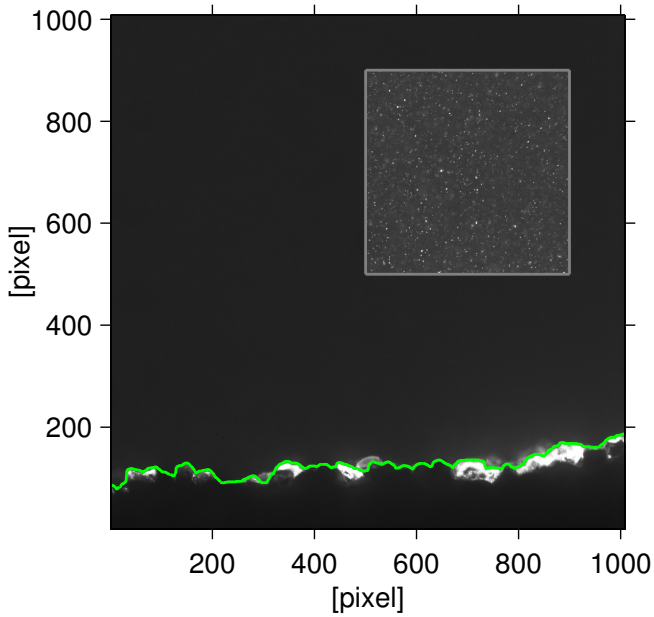

Figure 2.3: Background image. Rectangular inset shows part of a camera image with tracers when image brightness was increased. Green line is the edge of the mask.

2.4. Results

2.4.1. Flow regime

Jonsson (1980) delineated flow regimes using the wave Reynolds number, RE, and the relative roughness, a/k_N, were a is the horizontal orbital excursions and k_N is the Nikuradse roughness height equal to $2.5d_{50}$. The orbital excursion is given by $a = \sqrt{2}\tilde{u}_{rms}T/2/\pi$ where $\tilde{u}_{rms}$ is the root-mean-square of the periodic free-stream velocity. The wave Reynolds number is given by $RE = \sqrt{2}\tilde{u}_{rms}a/\nu$ where ν is the kinematic viscosity of water. The hydraulic parameters are presented in

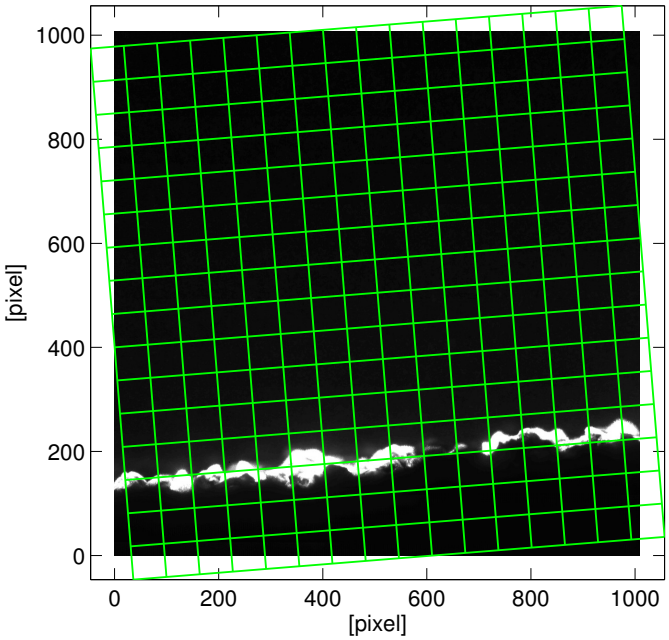

Figure 2.4: Background intensity image with the rotated orthogonal grid. Grid lines are normal and parallel to the bottom.

Table 2.1: Hydraulic conditions.

test id	h $[m]$	H_{rms} $[cm]$	$\widetilde{u}_{rms}$ $[m/s]$	$a = \sqrt{2}\widetilde{u}_{rms}T/2/\pi$	RE	a/k_N
T=1.0s@C1	0.267	8.5	0.112	0.025	3955	19
T=1.8s@C1	0.267	8.5	0.150	0.061	12829	47
T=2.5s@C1	0.267	7.6	0.151	0.085	18046	65
T=1.0s@C2	0.232	8.5	0.126	0.028	5076	22
T=1.8s@C2	0.232	8.4	0.171	0.069	16654	53
T=2.5s@C2	0.232	7.7	0.168	0.094	22411	73
T=1.0s@C3	0.187	8.7	0.144	0.033	6640	25
T=1.8s@C3	0.187	8.9	0.188	0.076	20181	58
T=2.5s@C3	0.187	8.1	0.195	0.110	30188	84
T=1.0s@C4	0.151	8.4	0.165	0.037	8651	29
T=1.8s@C4	0.151	8.7	0.197	0.080	22131	61
T=2.5s@C4	0.151	8.4	0.201	0.113	32098	87
T=1.0s@C5	0.143	7.7	0.160	0.036	8161	28
T=1.8s@C5	0.143	8.1	0.159	0.064	14468	50
T=2.5s@C5	0.143	7.5	0.172	0.097	23500	74
T=1.0s@C6	0.161	7.2	0.141	0.032	6325	24
T=1.8s@C6	0.161	6.0	0.129	0.052	9518	40
T=2.5s@C6	0.161	5.7	0.121	0.068	11628	52

Table 2.1 and shown in Figure 2.5. Wave Reynolds numbers were between 4×10^3 and 3×10^4 and the relative roughness was between 19 and 87. The flow regimes of the wbbl were in the 'transition' regime positioned between the 'laminar' and the 'rough turbulent' regime, see Figure 2.5. This indicates that the flow was laminar during low velocities with some turbulence during high velocities generated by the roughness elements. In nature, the flow conditions during onshore bar migration have larger relative roughness and wave Reynolds numbers due to larger orbital excursions, velocities and periods. Thus, flow in nature is more turbulent than in the wave flume and is in the 'smooth turbulent' regime, i.e. the onset of turbulence is caused by flow instability, see Figure 2.5 for comparison.

2.4.2. Surface Elevation

The root-mean-square wave height H_{rms} was calculated from the variance of the surface elevation

$$H_{rms} = \sqrt{8\overline{\eta^2}} \tag{2.4}$$

and is shown in Figure 2.6a. The wave height for the three wave conditions were slightly different at the wave maker but converge at the crest of the bar. Waves with longer periods showed a higher increase in wave height towards the bar crest due to more intense wave shoaling. Once the waves passed the crest of the bar they started to de-shoal due to increased water depth. Some waves did become unstable after passing the top of the bar and broke. From observations it was evident that waves with longer periods broke more frequently. The waves started to re-shoal after passing the trough of the bar.

As waves shoaled, their shape became skewed (sharp crests and flat troughs) and, later on, also asymmetric (pitched forward). Elgar and Guza (1985) defined

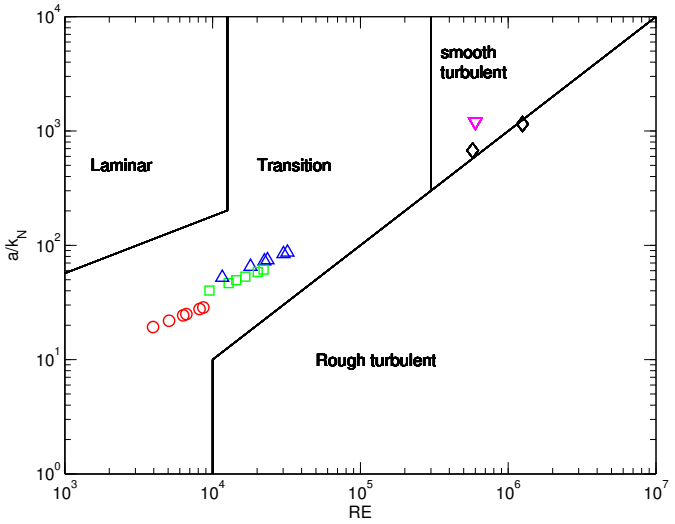

Figure 2.5: Delineation of flow regimes following Jonsson (1980). The markers, circle, square and upward-pointing triangle correspond with wave periods of 1.0, 1.8 and 2.5 s, respectively, the black diamonds correspond with tests of van der A et al. (2011) and the downward-pointing triangle corresponds with mild wave conditions during the Duck 1994 experiment (Berni et al., 2013b; Elgar et al., 2001).

the wave skewness as

$$\text{Sk of } \eta = \frac{\overline{(\eta - \overline{\eta})^3}}{\overline{(\eta - \overline{\eta})^2}^{1.5}} \tag{2.5}$$

and asymmetry as

$$\text{As of } \eta = \frac{\overline{(\mathcal{H}(\eta - \overline{\eta}))^3}}{\overline{(\eta - \overline{\eta})^2}^{1.5}} \tag{2.6}$$

where η denotes the surface elevation as a function of time and $\mathcal{H}$ the imaginary part of Hilbert transform. As waves become more pitched forward, the asymmetry becomes more negative. It is actually common practice in coastal engineering to say that the asymmetry increases for larger negative values, this use of word is maintained in this manuscript. The wave skewness is shown in Figure 2.6c and the wave asymmetry in Figure 2.6e. Generally, maximum skewness and asymmetry were found over the bar crest. While skewness decreased after the bar crest, asymmetry stayed more or less constant. Waves with periods of 1.8 s had the largest skewness at all wave gauges while waves with periods of 2.5 s had the largest asymmetry at all wave gauges. Waves with periods of 1.0 s had an asymmetry near zero at all wave gauges.

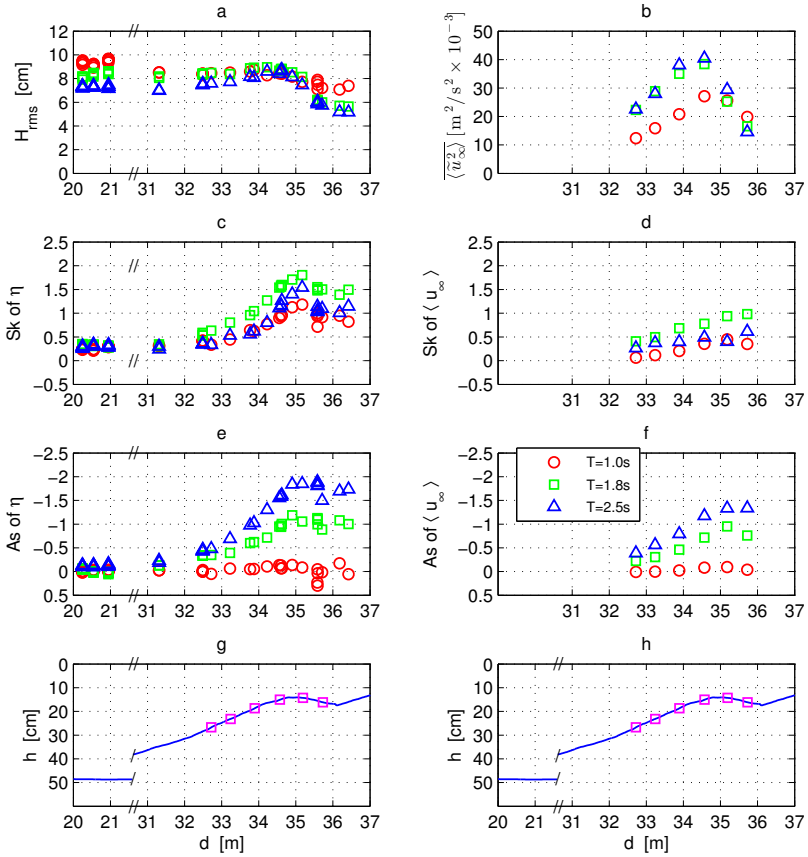

Figure 2.6: Characteristics of surface elevation and free stream velocity. (a) Root-mean-square wave height. (b) Second moment of free-stream velocity u. (c) Skewness of the surface elevation. (d) Skewness of the free-stream velocity u. (e) Asymmetry of the surface elevation. (f) Asymmetry of free-stream velocity u. (g,h) Water depth h with respect to the still water level where d is the distance from the wave board.

2.4.3. Free-stream velocity

The upper boundary of the measurement window is approximately 10 mm above the bottom and there the flow can be considered free stream since the wbbl is expected to be a few millimeters. Generally, the second velocity moments, velocity skewness, and velocity asymmetry increased from the wave maker to the bar crest, see Figures 2.6b, 2.6d and 2.6f. After the bar crest, at C5 and C6, the second velocity moments decreased and intersected for tests with different periods.

The time series of the free-stream horizontal velocity of `T=1.0s@C4`, `T=1.8s@C4` and `T=2.5s@C4` (tests on the bar crest where the ratio of wave height to water depth was largest) are presented in Figure 2.7. Positive velocities were larger than negative velocities due to wave skewness. For the same reason, the duration of positive velocities was smaller than of negative velocities. Tests with significant wave asymmetry experienced a shorter acceleration phase than deceleration phase. The largest decelerations occurred just after passing of the wave top but still in the positive phase. In all, skewed asymmetric waves experienced large velocity changes from the wave trough to just after the wave top. This implies that the life expectancy of the positive wbbl is relatively short.

2.4.4. Profiles of the horizontal velocity

In general, the profiles of the horizontal periodic velocity had typical wbbl features such as overshoot and phase lead. Figure 2.8 shows the profiles of `T=2.5s@C4` (test with the largest dimensional velocity asymmetry). The overshoot during the acceleration phase was larger than during the deceleration phase where the overshoot was almost nonexistent. The upper part of the positive overshoot extended 5 mm up into the water column. Near-bed velocity gradients were larger during positive flow than during negative flow.

2.4.5. Velocity transformation

The velocity skewness and asymmetry were determined using Eq. 2.5 and 2.6. The velocity skewness near the bottom decreased for waves with periods of 1.0 s from location C1 to C4. Waves with periods of 1.8 s and 2.5 s, had an increase of velocity skewness near the bottom at all locations. The velocity asymmetry near the bottom decreased for all tests. Figure 2.9 shows the vertical profiles of velocity skewness and asymmetry in the wbbl at location C4. The skewness of `T=2.5s@C4` was twice as large near the bottom ($Sk_c = 1.3$) as in the free stream ($Sk_\infty = 0.5$) (subscript c denotes the level ($z = d_{50}$) corresponding with the crests of protruding roughness elements). This effect was less for `T=1.8s@C4` with near-bottom skewness of ($Sk_c = 1.1$) and free-stream skewness of ($Sk_\infty = 0.8$). Figure 2.10 shows the ratio of near-bottom to free-stream velocity skewness, Sk_c/Sk_∞, as a function of the ratio of free-stream velocity asymmetry to skewness, As_∞/Sk_∞, for all tests. The data show that Sk_c/Sk_∞ was larger when As_∞/Sk_∞ was larger. Note that the skewness and asymmetry of tests with periods of 1.0 s were relatively small which leads to significant scatter in Figure 2.10.

Henderson et al. (2004) showed that the shape of the velocity oscillations change in the wbbl due to phase shifts of the frequency components. The amount of de-

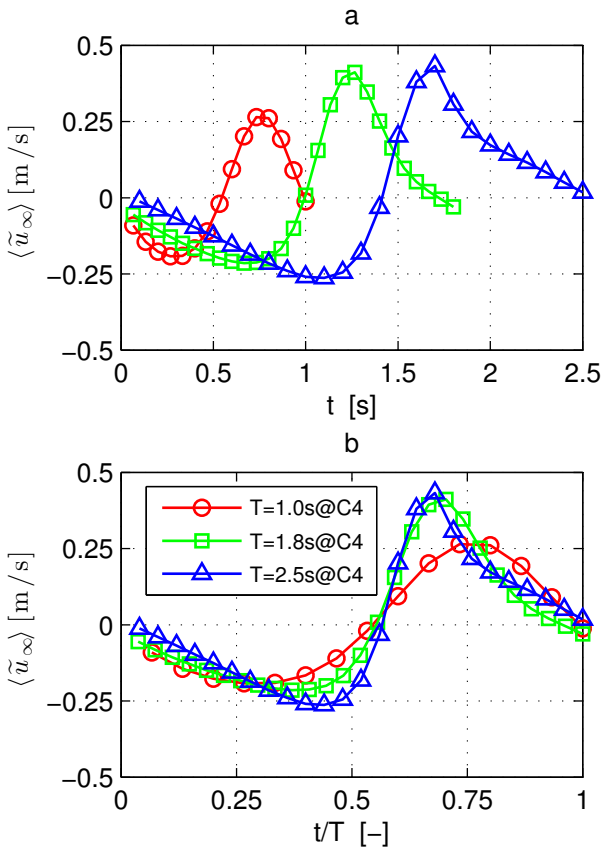

Figure 2.7: Free-stream periodic velocity at C4. (a) velocity versus time and (b) velocity versus time normalized by the wave period.

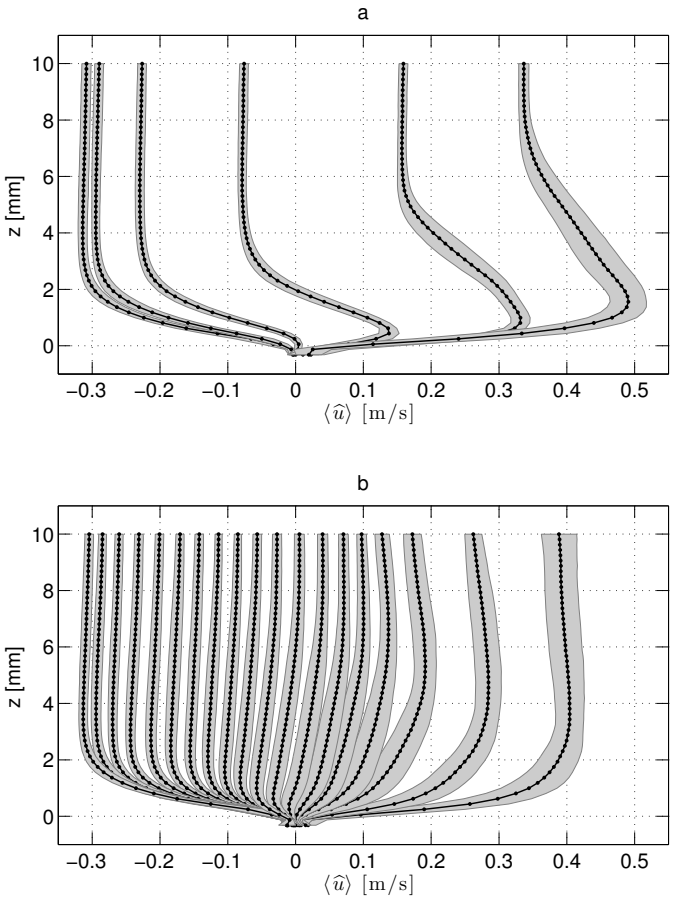

Figure 2.8: Ensemble-average velocity profiles of `T=2.5s@C4` during (a) the accelerating phase and (b) the decelerating phase. Shading indicates the root-mean-square of the fluctuations $\left\langle \sqrt{\widehat{(u')^2}} \right\rangle$.

formation, in this paper measured by velocity skewness and asymmetry, depends on the free-stream velocity skewness and asymmetry. Based on the work of Elgar and Guza (1985) and Henderson et al. (2004), Berni et al. (2013b) formulated the relation,

$$\frac{Sk_b}{Sk_\infty} = \cos(\phi_b) - \sin(\phi_b)\frac{As_\infty}{Sk_\infty} \tag{2.7}$$

that estimates the velocity skewness near the bottom. The relation is derived from bispectrum properties with the assumption that near the bottom the harmonic frequencies have similar phase shifts and gain. These assumptions were suggested by Henderson et al. (2004) based on their numerical wbbl model results. They found a constant phase shift of 25 degrees close to the bottom where gain values were approximately 0.2. Eq. 2.7 is shown in Figure 2.10 for phase shift of 25 degrees. Eq. 2.7 underestimates the skewness at $z = d_{50}$ for waves with periods of 1.8 s and 2.5 s ($R^2 = 0.86$). The reason for this is that although the phase shifts of the harmonic frequencies were approximately 25 degrees at $z = d_{50}$, the gains of the second harmonic frequencies were approximately 0.1 larger than the gains of the first harmonic frequencies thus in conflict with one of the underlying assumptions of Eq. 2.7. An increase of gain along the frequency components near the bottom contributes to larger ratio of Sk_c to Sk_∞ than constant gain along the frequency components.

Berni et al. (2013b) pointed out that the above-mentioned assumptions are not valid for laminar oscillatory flow described by Batchelor (2000) and the signal deformation near the bottom, where the orbital velocity goes to zero, follows

$$\frac{Sk_b}{Sk_\infty} = 1 - \frac{As_\infty}{Sk_\infty} \quad . \tag{2.8}$$

Eq. 2.8 is shown in Figure 2.10. Since phase shifts in the coastal wbbl are not higher than 45 degrees (Nielsen, 1992), Eq. 2.8 provides an upper limit for the ratio of near-bottom to free-stream velocity skewness, Sk_b/Sk_∞.

2.4.6. Time-averaged horizontal velocities

The vertical profiles of the time-average spatial-average horizontal velocity are shown in Figure 2.11. Tests with periods of 1.8 s and 2.5 s had more or less identical vertical profiles in contrast to tests with a period of 1.0 s. However, at the upper boundary of the PIV vector field the horizontal velocity was always negative for all tests at all locations. On the offshore slope of the bar at C1 all tests had a positive horizontal velocity near the bottom. Moving along the camera locations further from the wave maker, the positive horizontal velocity near the bottom changed to negative for tests with periods of 1.8 s and 2.5 s, but for tests with a wave period of 1.0 s this occurred only at C6. The vertical profile for tests with a period of 1.0 s had the largest negative horizontal velocity at C1 while further from the wave maker up to the bar crest, at C3 and C4, tests with periods of 1.8 s and 2.5 s had significantly larger negative horizontal velocities. Remarkable is that the largest negative horizontal velocity at C3 and C4 were just above the wbbl at z is 3 mm

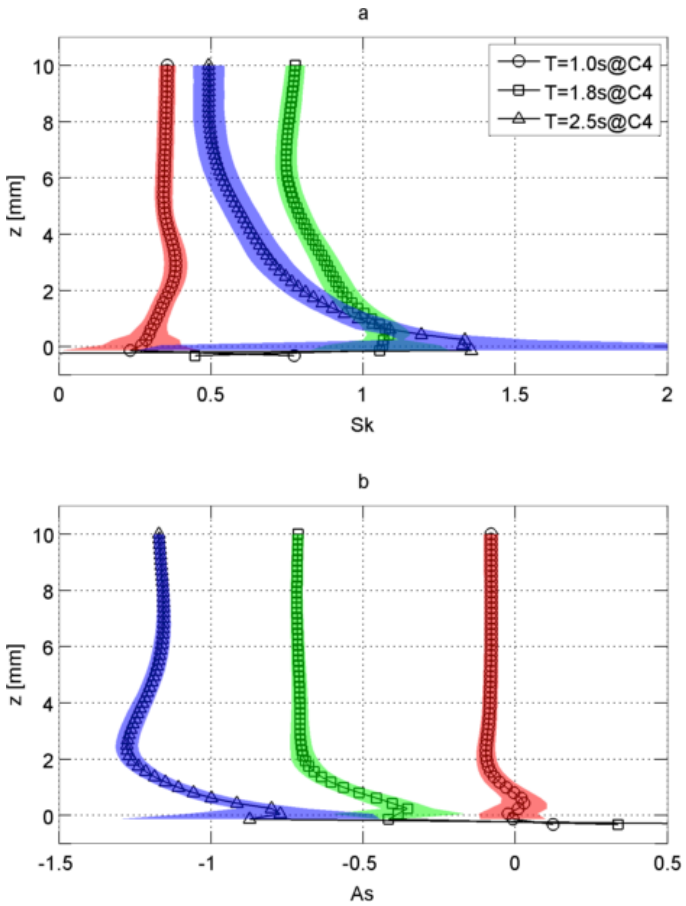

Figure 2.9: Velocity skewness (a) and asymmetry (b) in the wbbl at location C4. Shading indicates standard deviation around the vertical profile.

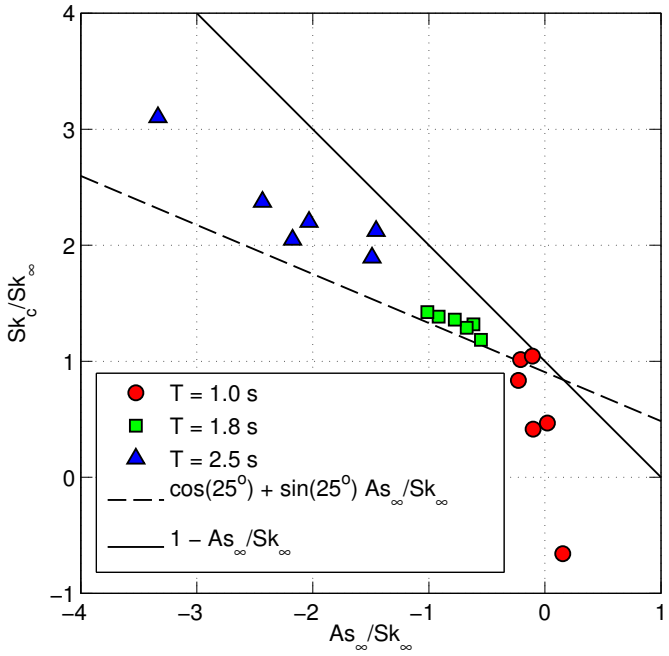

Figure 2.10: Near-bed to free-stream skewness ratio as a function of the free-stream asymmetry to skewness ratio. Markers represent measurements, dashed line is Eq. 2.7 and solid line is Eq. 2.8.

and not at the highest point in the profile. After the bar crest, at C5 and C6, the profiles tended to follow a logarithmic shape.

The negative horizontal velocity at the upper boundary of the PIV vector field could be explained by the positive mass transport caused by the free-stream wave motion also known as Stokes drift (Phillips, 1977). Since the flume was closed it can be assumed that the total volume flux was zero. On the basis of continuity there would be a time-averaged return flow. Also, after the bar crest, at C5 and C6, wave breaking was observed which is known to generate a flow circulation with a flow opposite to the wave direction near the bottom (Dyhr-Nielsen and Sorensen, 1970).

Longuet-Higgins (1953) showed that the wbbl generates a time-averaged flow in the wave direction under progressive waves. Later on, Trowbridge and Madsen (1984) showed that bottom-generated turbulence under nonlinear waves generates a time-averaged flow opposite to the wave direction in the wbbl. These two competing mechanisms can clearly be seen in the profiles where tests with a wave period of 1.0 s had a dominance of positive wbbl streaming and test with a wave period of 2.5 s had a dominance of negative wbbl streaming.

2.4.7. Horizontal velocity gradients

This section presents the spatial velocity gradients over the measurement area. Figure 2.12a shows the free-stream horizontal velocity. The spatial gradients over the measurement area corresponded with the surface elevation of a wave. The root-mean-square velocity over the ensemble, i.e. turbulence, was generally 0.01 m/s and at phase 17 was up to 0.03 m/s. The turbulence over the measurement area at phase 17 and 18 was not constant.

Figure 2.12b shows the free-stream vertical velocity. The largest vertical velocities were measured at phase 14 and 17. Phase 14 is the upcrossing of the horizontal ensemble-average velocity. This is in line with the fact that the vertical and horizontal velocity are in quadrature. The horizontal gradients from phase 15 to 18 did not correspond with the gradual course of the wave motion. Over phase 15 to 18, the root-mean-square velocity was 0.02 m/s, while the other phases were 0.005 m/s.

Figure 2.12c shows the same as Figure 2.12b at 4.2 mm above the bottom. Relatively large horizontal gradients started at phase 14. These horizontal gradients had the same signature as those in the free stream.

Figure 2.12d shows the same as Figure 2.12b at 1.2 mm above the bottom. At this distance from the bottom there was no wave-related vertical velocity visible as in Figure 2.12b. However, ensemble-average velocities varied from 0 to 0.02 m/s over the horizontal distance of a few millimeters at phase 14. Turbulence emerged one phase later.

The striking signature of the vertical velocity over the measurement area at an elevation of 1.2 mm above the bottom at phase 14 was also visible, to a lesser extent, at phase 13 (see Figure 2.12d). The "negative" of this signature can be seen, among others, during phase 1 to 12. The direction of the horizontal flow dictated the sign of the vertical velocity. This means that the roughness elements perturbated the flow with a wave length in the order of 10 mm.

The amplitude of the flow perturbation increased rapidly from phase 13 to 14.

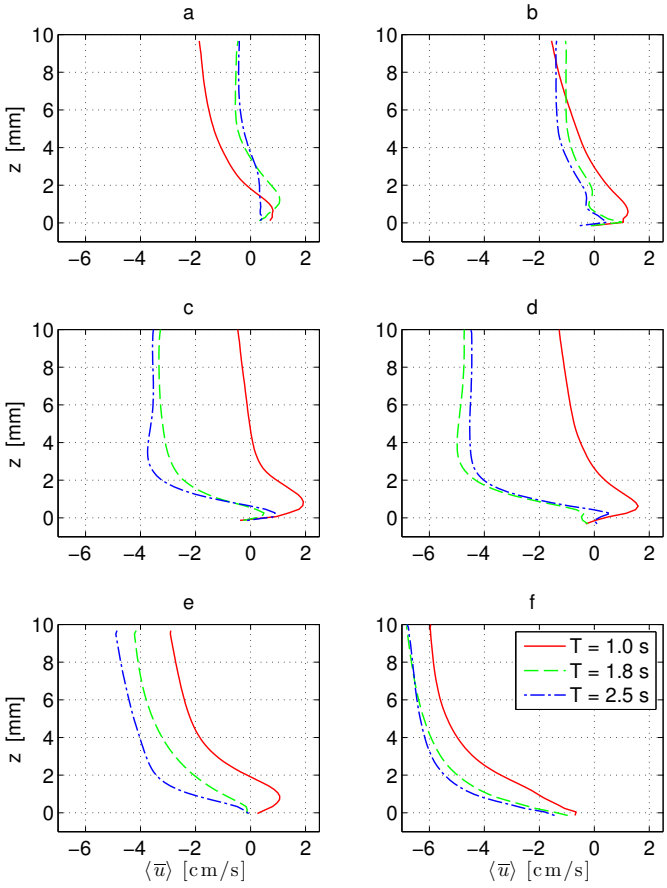

Figure 2.11: Vertical profiles of the time-average horizontal velocity at all camera locations. Panel (a) to (f) corresponds with camera locations C1 to C6, respectively.

The timing corresponded with the horizontal flow reversal from negative to positive. The amplitude growth was not seen was not seen during flow reversal from positive to negative (phase 25).

The absence of turbulence at phase 13 and 14 indicates periodic flow, i.e. the flow perturbations emerged at one consistent time and location during every wave of the ensemble.

All tests contained amplitude growth of the vertical velocity over the bottom perturbation at one or both flow reversals. However, the impact on the ensemble-average flow varied significantly. For instance, the impact during `T=2.5@C4` is clearly visible. The flow perturbations resembled coherent structures known as vortex tubes, i.e instabilities generated at an inflectional point of an oscillatory boundary layer (Akhavan et al., 1991; Carstensen et al., 2010; Foster et al., 1994). In the following section we further investigate the flow perturbations and try to identify when they became vortical structures.

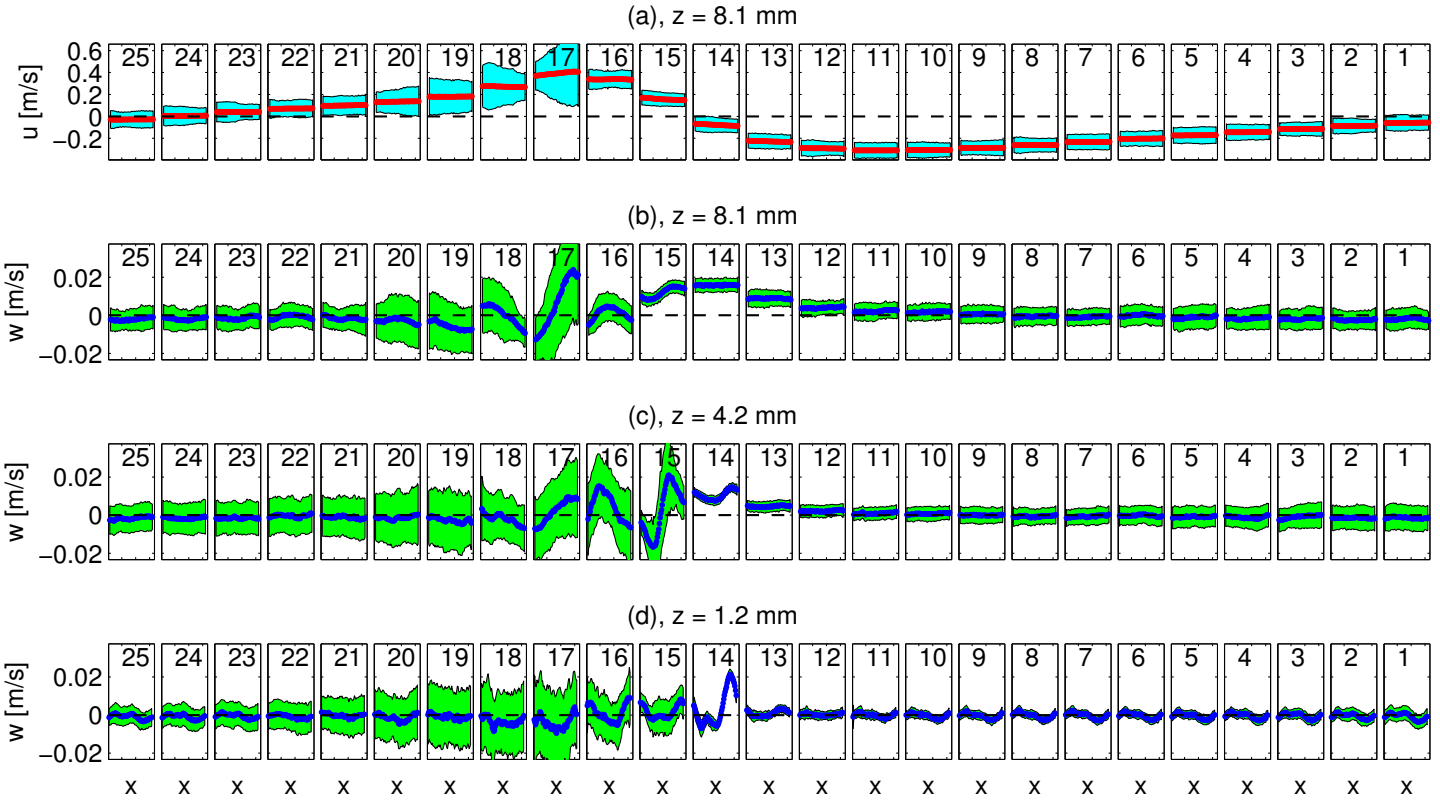

Figure 2.12: Spatial overview of velocities of `T=2.5@C4`. The horizontal axis of a box is x which is positive to the right and directed to the shore. The vertical axis of a box is the velocity. Every box corresponds with a measured wave phase indicated by the number in the box. By placing the boxes one after the other from right to left, a reconstruction of the velocities in space is imitated. (a) The red line is the ensemble-average horizontal velocity at $z = 8.1$ mm. The cyan band around the red line represent the root-mean-square of the fluctuations around the ensemble, i.e. turbulent component, times a factor of 10 (to be visible). (b) The blue line is the ensemble-average vertical velocity at $z = 8.1$ mm. The green band around the blue line is the root-mean-square of the fluctuations around the ensemble (here, no scaling is applied). (c) Idem at $z = 4.2$ mm. (d) Idem at $z = 1.2$ mm.

2.4.8. Vortex tubes

Swirling strength

Vorticity, quantified by velocity shear, is dominated by the large vertical velocity shear of the boundary layer and cannot be used to identify vortices in the boundary layer (see e.g. Nichols and Foster, 2007). Swirling strength is quantified with the eigenvalues of the velocity gradient tensor and is ideal for vortex identification (see e.g. Jeong and Hussain, 1995). For this research we adopt the practical formulation by Hofland (2005). In the (x, z)-plane, the swirling strength λ_{ci} was quantified as

$$4\lambda_{ci}^2 = \max\left[0,\ -4\frac{\partial u}{\partial z}\frac{\partial w}{\partial x} + 2\frac{\partial u}{\partial x}\frac{\partial w}{\partial z} - \frac{\partial u}{\partial x}^2 - \frac{\partial w}{\partial z}^2\right] \quad . \tag{2.9}$$

λ_{ci}^2 is zero when the shear is dominant over the rotation.

Figure 2.13 shows the swirling stress of the first measured wave of `T=2.5s@C4`. During the wave trough, see Figure 2.13c, there was a horizontal band of small-sized patches (diameter < 1 mm) in the lower 3 mm from the bottom. During flow reversal from negative to positive, see Figure 2.13d, one large-sized patch with significant swirling strength emerged with the center at $x = 8$ mm and $z = 2$ mm. The patch coincided with the center of the vortical structure defined by the streamlines. During maximum velocity, see Figure 2.13e, there were numerous medium-sized patches of significant strength distributed over the measurement area. During flow reversal from positive to negative, see Figure 2.13b, there were numerous medium-sized patches of low strength distributed over the measurement area.

It appears that during `T=2.5s@C4`, large vortices were generated close to the bottom during free-stream flow upcrossings. These vortices were entrained in the flow and prevailed over the whole positive free-stream flow cycle.

The rapid increase of vertical velocities at phase 14 in Figure 2.12d coincided with the large-sized patch of swirling strength in Figure 2.13d. These vertical velocities appear to be part of a vortex.

Swirl patch statistics

The swirling strength was calculated for all vector fields. Values smaller than 5 s^{-1} were not considered. Scalars that were connected to at least 4 others were grouped together. Properties of vortices such as width, height, area A, equivalent diameter $d = 2\sqrt{A/\pi}$ and location of centroid were extracted.

The size distribution of swirl patches during phase 14 of `T=2.5s@C4`, see Figure 2.14a, was double-peaked with a clear group of patch sizes in the range of 3 to 5 mm. The number of big patches totals the amount of measured waves of the test. The centroid of the big patches were focused around the location ($x \approx 8$ mm, $z \approx 2$ mm). This means that the big patch of swirling strength in Figure 2.13d was reproduced every wave cycle.

The swirling strength analysis detected big vortices for tests with periods of 1.8 and 2.5 s at C3 and C4 during flow reversal from negative to positive (see Figure 2.15a). These tests had wave Reynolds numbers of $4 \times 10^3 < RE < 3 \times 10^4$ (see Figure 2.15c). No big vortices were detected during flow reversal from positive to negative (see Figure 2.15b).

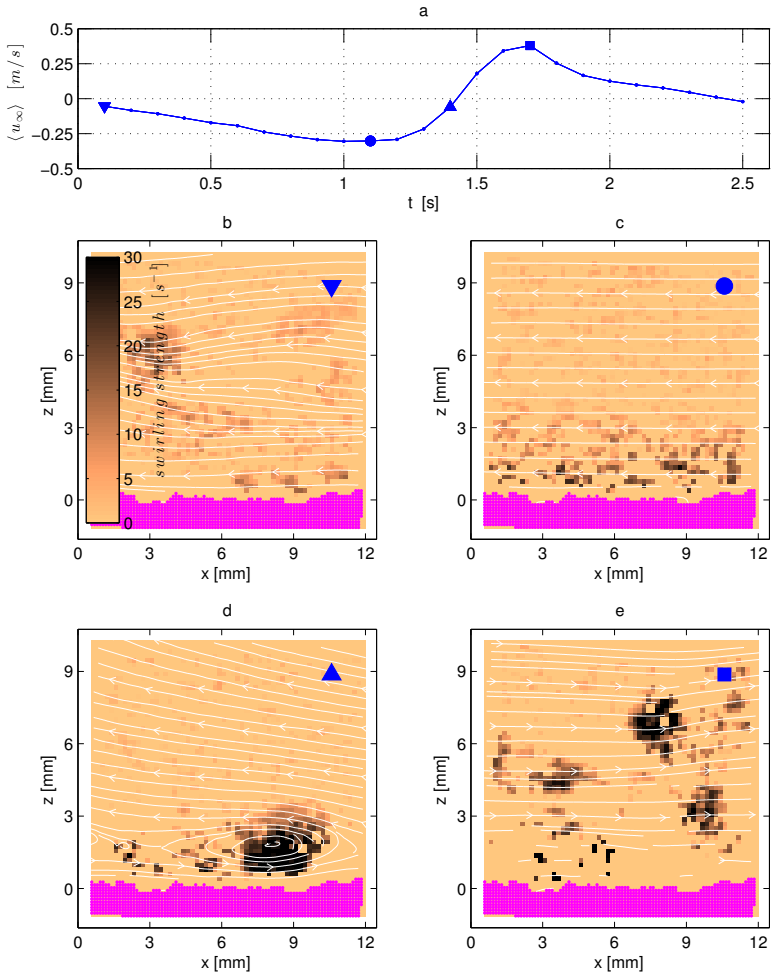

Figure 2.13: Swirling strength of the first wave of `T=2.5s@C4`. (a) free-stream horizontal velocity with four specific markers, downward-pointing triangle for the downcrossing, circle for the minimum, upward-pointing triangle for the upcrossing and a square for the maximum. (b) swirling strength of the flow during the downcrossing. White lines are streamlines and the purple color represents the bottom. (c) idem for the minimum velocity. (d) idem for the upcrossing. (e) idem for the maximum.

Experiments by Carstensen et al. (2010) showed that vortex tubes over a smooth bottom were generated by flow perturbations with wavelengths of $l \approx 6\delta$. The boundary layer thickness of laminar oscillatory flow is $\delta = 3\pi/4\sqrt{2\nu/\omega}$, for periods of 2.5 s, $\delta = 2.1$ mm leading to $l \approx 12$ mm. The vortical structure visible by the streamlines in Figure 2.13d had a similar length. However, the diameters of the big swirl patches were consistently smaller. This can be explained by the spatial variation of swirling strength over the vortex area where the largest magnitudes are concentrated around the center (compare e.g. the streamlines with the swirl patch in Figure 2.13d).

On a smooth bottom, vortex tubes were seen by Carstensen et al. (2010) for wave Reynolds numbers between $7 \times 10^4 < RE < 3 \times 10^5$. The lower limit is larger than the wave Reynolds number of the present tests. Contrary to a smooth bottom, the rough bottom contained a range of perturbations with wavelengths of the same order as the wavelengths of vortex tubes. This may explain the occurrence of vortex tubes during $RE < 7 \times 10^4$. Another big difference was the shape of the free-stream flow of Carstensen et al. (2010) which did not contain any velocity skewness and asymmetry. In the present data, velocity skewness and asymmetry was significant, see Figure 2.6. The different flow condition during flow reversal under the wave front and back may explain the absence of vortex tubes during flow reversal from positive to negative (see Figure 2.15b).

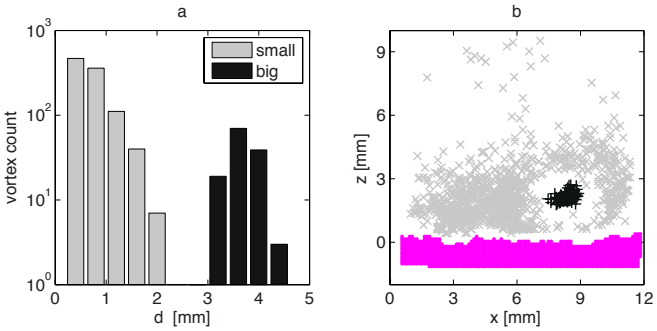

Figure 2.14: Distribution of swirl patches of `T=2.5s@C4` at the upcrossings (phase 14) of the free-stream horizontal velocity. (a) Patch count versus patch diameter. (b) Locations of the patch centroid. Magenta indicates the bottom.

2.4.9. Reynolds stress

The Reynolds stress is defined as $-\rho\widehat{u'w'}$ and shown in Figure 2.16. Larger stresses were measured for larger periods. Largest stresses ($\sim 0.4\ N/m^2$) were measured at C4. Positive and negative stresses were separated by the developing boundary layer edges. Positive stresses emerged at the bottom and diffused upward while negative stresses appeared 2 mm above the bottom. `T=1.8s@C6` and `T=2.5s@C6` form an exception from the other tests with large stresses at the upper boundary of

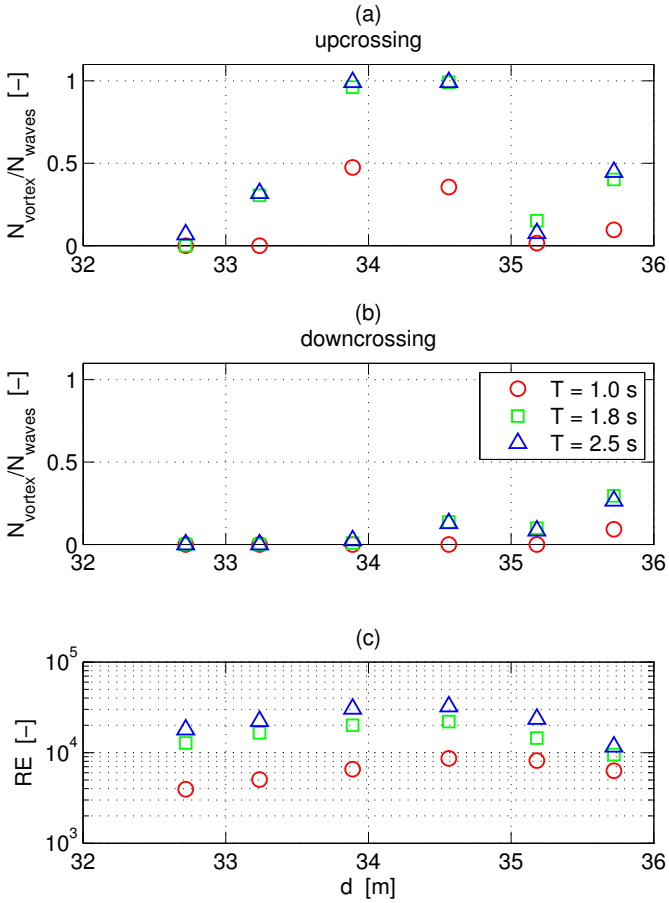

Figure 2.15: Overview of vortex generation during flow reversal. (a) Vortex tube count during flow reversal from negative to positive. (b) Vortex tube count during flow reversal from positive to negative. (c) Wave Reynolds number of all tests.

the measurement window.

Vertical velocity shear du/dz during `T=1.8s@C4` was $O(100$ m/s/m) leading to viscous shear stresses τ_{zx} of $O(0.1\ N/m^2)$. Hence, viscous- and turbulent stresses were similar which supports the suggestion that the tests with periods of 1.8 and 2.5 s were in the transitional flow regime between laminar and rough turbulent (see Figure 2.5 for flow regimes).

With the exception of `T=1.8s@C6` and `T=2.5s@C6`, the measured negative stress may be the aftermath of vortex tubes. Vortex tubes are characterized by their 2D structure that will eventually breakdown and turn into 3D chaotic motion.

Negative stresses were detected at C5 while there were no big swirl patches detected (see Figure 2.15a). It must be noted that the actual vortex tubes that were generated in the measurement window were not directly related to the measured negative stresses. The amplitude of the orbital excursion was $\sim$ 50 mm and the window was $\sim$ 12 mm wide. Big swirl patches captured in the measurement window were advected outside the window. Thus, measured negative stresses were related to vortex tubes from adjacent areas. It could be that the local bottom, captured in the 12 mm window at C5, was relatively flat or the bottom perturbations did not include the wavelengths to generate unstable flow perturbations.

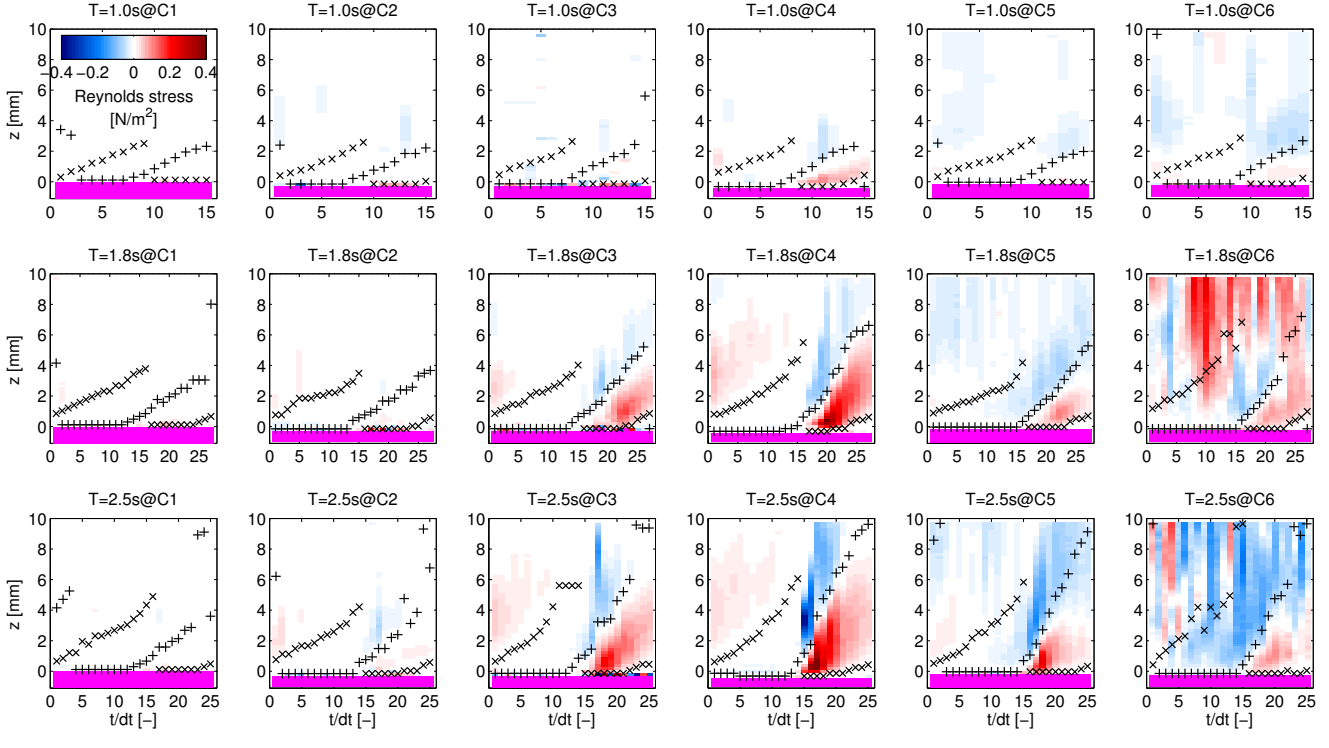

Figure 2.16: Timestacks of vertical profiles of Reynolds stress $\langle -\rho\widehat{u'w'}\rangle$. Colorbar gives values of $\langle -\rho\widehat{u'w'}\rangle$. Magenta color indicates the bottom. The plusses and crosses are the vertical location of maximum and minimum velocity $\langle\widehat{u}\rangle$, respectively, which shows the boundary layer thickness over time. The horizontal axis is divided by dt resulting in measured phase numbers.

2.4.10. Boundary layer thickness

The wbbl thickness δ is defined as the distance from $z = 0$ to the point of maximum or minimum velocity $\langle\widetilde{u}\rangle$ in a vertical measure profile. The point of maximum or minimum velocity tends to coincide with either a zero velocity at the bottom or the velocity overshoot. Figure 2.17 shows the wbbl thickness as a function of time for `T=2.5s@C4`. The wbbl thickness increased linearly in time during favorable horizontal pressure gradients (i.e. when the sign of the pressure gradient is opposite to the sign of the fluid velocity). The coefficient of determination R^2 between measurements and a linear fit was usually above 0.9. When the pressure gradient sign switched, the boundary layer thickness showed a sudden increase. Highly asymmetric waves had wbbl growth rates under the wave front that were roughly twice as large as under the corresponding wave back.

The analytic model by Batchelor (1967) describes a purely 1D oscillatory laminar flow. The model is given as

$$u(r,t) = U\left[\cos\omega t - e^{-\frac{r}{\delta_s}}\cos\left(\omega t - \frac{r}{\delta_s}\right)\right] \quad , \tag{2.10}$$

where U is velocity amplitude, r is the axis normal to the bottom, $\delta_s = \sqrt{2\nu/\omega}$ is the Stokes length, $\omega = 2\pi/T$ is the angular wave frequency and ν is the fluid viscosity. The time evolution of the wbbl thickness can be expressed by taking the spatial derivative of Eq. 2.10 and equate it to zero

$$U\left(\frac{1}{\delta_s}e^{-\frac{z}{\delta_s}}\cos\left(\omega t - \frac{z}{\delta_s}\right) - \frac{1}{\delta_s}e^{-\frac{z}{\delta_s}}\sin\left(\omega t - \frac{z}{\delta_s}\right)\right) = 0 \quad . \tag{2.11}$$

The solutions give the boundary layer thickness as a function of time. The solution for the boundary layer development during the positive flow phase is

$$\delta^+ = (3/4)\pi\delta_s + \omega\delta_s t \tag{2.12}$$

and during the negative flow phase

$$\delta^- = -(1/4)\pi\delta_s + \omega\delta_s t \quad . \tag{2.13}$$

This implies that the purely sinusoidal laminar boundary layer thickness increases linearly in time $\delta \sim t$, the growth rate is a function of $1/\sqrt{T}$ and the maximum boundary layer thickness is a function of $\sqrt{T}$. This is different from Nielsen (1992) and flows with steady pressure gradients where the boundary layer grows $\delta \sim \sqrt{t}$. Based on Eq. 2.12 and 2.13, the growth rate can be expressed as

$$d\delta^+/dt = \sqrt{2\pi\nu/t_{front}} \tag{2.14}$$

and

$$d\delta^-/dt = \sqrt{2\pi\nu/t_{back}} \tag{2.15}$$

where t_{front} and t_{back} are defined as the duration of the wave front and wave back, respectively. For sinusoidal waves t_{front} is equal to t_{back} but for asymmetric waves

this is not the case. Eq. 2.14 and 2.15 suggest that under pitched forward waves the wbbl growth rate is larger under the wave front that under the back. The boundary layer growth rate of the measurements was estimated by using the slope of the linear fits. Figure 2.18 shows the wbbl growth rate plotted against the duration of wave front or back. The measured growth rates were generally larger for shorter t_{front} and t_{back}, and, were generally larger than Eq. 2.14 and 2.15.

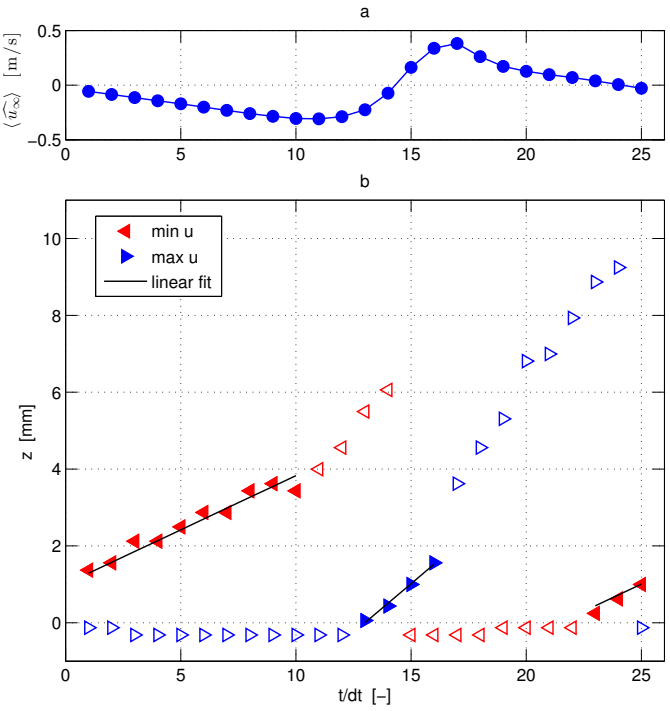

Figure 2.17: Wbbl thickness as a function of time for `T=2.5s@C4`. Panel a shows the time series of the free-stream horizontal velocity. Panel b shows the time evolution of the wbbl thickness defined by the minimum and maximum of $\langle\widetilde{u}\rangle$. Filled markers correspond with boundary layer growth during favorable pressure gradients and empty markers during adverse pressure gradients.

2.5. Conclusions

Detailed flow velocities were measured of the wave bottom boundary layer under progressive surface waves traveling over a fixed single bar profile in a medium-sized wave flume.

Free-stream asymmetric velocity signals transformed to skewed signals in the wbbl. Near-bottom skewness was linearly related to the free-stream skewness and asymmetry.

In some tests vortex tubes were generated during flow reversal from negative to positive. These tests were characterized by large velocity skewness and asymmetry.

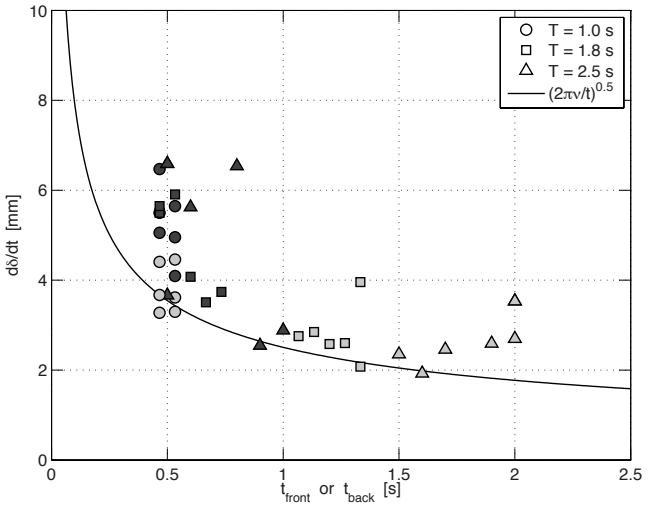

Figure 2.18: Wbbl growth rate as a function of t_{front} and t_{back} for all tests. Blue and red color indicate positive and negative flow phase, respectively.

Due to fixed roughness elements and regular waves, the vortex tubes were generated at fixed locations and wave phases.

Negative Reynolds stresses were observed a few millimeters above the bottom after the generation of vortex tubes. Positive Reynolds stresses were observed during the positive flow phase and originated from the bottom.

Significant time-averaged currents were measured in the order of 1 cm/s. Wave wbbl streaming was negative instead of positive under skewed and asymmetric waves.

The wbbl thickness increased linear in time under favorable pressure gradients. The wbbl growth rate under asymmetric waves was larger under the wave front than under the wave back. However, the wbbl thickness was larger under the wave trough than under the wave top under asymmetric waves.

3

Intra-wave bed shear stress by nonlinear waves

Skewed and asymmetric waves in the nearshore are known to generate onshore sediment transport. However, there are still large uncertainties in the estimation of the bed shear stress under arbitrary non-sinusoidal waves. Data of laboratory wave flume tests and k-ϵ numerical model tests were utilized to gain more insight in mechanics of the time-varying bed shear stresses. We tested the validity of the analytic boundary layer solution for laminar flow, the time-depended quadratic drag-law and a waveform expression. It turns out that non-sinusoidal regular waves were accurately described by a fairly simple waveform expression. The bed shear stresses in the laminar flow regime were described by the analytic boundary layer solution. In the turbulent regime, the bed shear stresses were adequately described on the basis of the quadratic drag-law. An essential item for the correct time-evolution of the bed shear stress was the consideration of a frequency-independent phase shift that allows for the transfer of free-stream velocity asymmetry to friction velocity skewness.

3.1. Introduction

As waves travel to shore their shapes change from symmetrical to sharp crested (skewed) and pitched forward (asymmetric) (Elgar and Guza, 1985). Skewed waves are known to generate a net shoreward flux of sediment because the instantaneous sediment transport depends on the power 3 to 4 of the free-stream velocity (Bowen, 1980; Dohmen-Janssen and Hanes, 2002; Ribberink and Al-Salem, 1995). On the other hand, the effect of wave asymmetry on the net sediment transport is less clear (e.g., Henderson et al., 2004; Hoefel and Elgar, 2003; Hsu et al., 2006). The impact of the free-stream velocity asymmetry on the bed shear stress was already suggested and modeled through a transfer function by Nielsen (1992, 2002). Later on, Terrile et al. (2009b) and Abreu et al. (2013) improved and extended Nielsen's transfer function. In the meantime, measurements and numerical models showed

that free-stream velocity asymmetry is actually transformed to velocity skewness in the wave bottom boundary layer (wbbl) (see Berni et al., 2013a; Henderson et al., 2004; Henriquez et al., 2014). Recently, Dubarbier et al. (2015) and Fernández-Mora et al. (2015) showed that the inclusion of wave asymmetry improved the capability to model the cross-shore morphology and specifically the onshore migration of sandbars in the nearshore. Therefore, a validation of the transfer function and the underlying assumptions is needed.

Basically, the transfer function works by summing a finite number of friction velocity harmonics. The friction velocity harmonics are calculated by shifting the velocity harmonics with a phase lead and by multiplying the velocity harmonics with friction coefficients. This results in a transfer function that describes a linear relationship between the friction velocity skewness and the free-stream velocity asymmetry (Berni et al., 2013a; Henderson et al., 2004).

According to the findings of Henderson et al. (2004) and Berni et al. (2013a), the linear relationship between the friction velocity skewness and the free-stream velocity asymmetry applies for laminar and turbulent flow regime. However, there are some essential differences between the laminar and turbulent flow regime. First, in laminar flow regimes the friction coefficients of consecutive harmonics depend on the harmonic frequency while in rough turbulent flow regimes the friction coefficients of consecutive harmonics are assumed to be similar. When the friction coefficients are similar there will be a weaker transfer function. The second difference is that in turbulent flow regimes the phase leads of the harmonic friction velocities are smaller than 45 degrees (Jensen et al., 1989; Jonsson and Carlsen, 1976; Sleath, 1987). A lower phase lead results in a weaker transfer function. The third difference is that in turbulent flow regimes the time-evolution of the bed shear stress agrees better with the quadratic relation for drag than the linear relation that applies for laminar flow regimes (e.g., Jensen et al., 1989; Jonsson and Carlsen, 1976; Lofquist, 1986; Sleath, 1987). However, Nielsen (2002) noted that the quadratic drag relation is not fully supported by experimental data.

Furthermore, the transfer function has always been calculated with the assumption that the phase leads of consecutive friction velocity harmonics are constant because there was no data to prove otherwise. This assumption needs to be validated. Recent tests by van der A et al. (2011) and Henriquez et al. (2014) provide detailed wbbl flow measurements suitable for this validation.

To apply the transfer function in practice, the time series of the nonlinear free-stream velocity is required. Abreu et al. (2010) developed a waveform description that conveniently generates the free-stream velocity time series based on the velocity skewness and asymmetry (see Abreu et al., 2013; Drake and Calantoni, 2001; Malarkey and Davies, 2012; Terrile et al., 2009b). However, the waveform description has not been validated against data of real surface waves.

In this chapter, we investigate the transfer of free-stream velocity asymmetry to friction velocity skewness in the laminar and turbulent flow regimes. For the laminar flow regime we analyze velocity measurements from a wave flume experiment. However, the wave flume experiment does not cover the turbulent flow regime and therefore we analyze the results of a numerical model that calculates the verti-

cal profile of the horizontal velocity by solving the Reynolds-averaged Navier-Stokes equation with a two-equation turbulence model for closure (Kranenburg et al., 2012; Uittenbogaard and Klopman, 2001). In addition, we test the validity of the waveform description against the surface elevations and flow velocities of the wave flume experiment.

In Section 3.2 we elaborate on the methods needed to analyze the amplitude and phase lead of the friction velocity. The wave flume experiment is described in Section 3.3 and the numerical model is described in Section 3.4. The results, discussion and conclusions are presented in Section 3.5, 3.6 and 3.7, respectively.

3.2. METHODS

The key variables of this investigation are the amplitudes and phase leads of the friction velocity. The friction velocity u_* can be directly converted from the bed shear stress τ_b based on the expression by Nielsen (2002, Equation 7)

$$\tau_b(t) = \rho \left(\sqrt{2} u_{rms}\right)^{2-\alpha} |u_*|^{\alpha} \text{sign}\left(u_*\right) \tag{3.1}$$

where t is time, u is the free-stream horizontal velocity, ρ the fluid density, the subscript rms indicates the root-mean-square and $\alpha = 1$ corresponds to the laminar form $\tau_b \sim u$ and $\alpha = 2$ corresponds to the quadratic form $\tau_b \sim u|u|$. Based on experimental data of near-bed fluid stresses in turbulent oscillatory boundary layers, Nielsen (2002) indicated that α is probably somewhere between 1 and 2. The value of α can be determined by considering a test with a sinusoidal free-stream velocity $u(t) = U \cos \omega t$, where U is the amplitude, ω is the angular frequency and t is time. Namely, raising the velocity to the power of α generates higher odd harmonics (see Appendix B). Thus, a frequency analysis on the bed shear stress $\tau_b(t)$ will reveal the value of α. The frequency analysis is performed by conducting the fast Fourier transform (FFT) on the time series. Higher harmonics with amplitudes that were smaller than 5% of the first harmonic were not included in the analysis.

To validate the waveform description by Abreu et al. (2010) we will compare how well the amplitudes and phases of the free-stream horizontal velocity are represented by the waveform. Based on the work of Drake and Calantoni (2001) and Abreu et al. (2010) used the following function to describe waveforms

$$u(t) = \Im \left\{ f_s \sum_{n=1}^{N} b^{n-1} \exp i \left[n\omega t + (n-1)\,\Phi \right] \right\} \tag{3.2}$$

Where $\Im$ denotes the imaginary part, f_s is a scale factor to get the correct signal energy, b is a coefficient that controls the harmonic amplitudes, n is the harmonic index, Φ is the so-called waveform parameter. Note that $(n-1)\Phi$ represents the harmonic phase shift θ_n and $\theta_1 = 0$. Malarkey and Davies (2012) showed that the relations between the velocity skewness Sk and velocity asymmetry As of the waveform and the waveform parameter Φ and the amplitude coefficient b are given by

$$\Phi = \tan^{-1}\left(\frac{-As}{Sk}\right) \tag{3.3}$$

$$b^2 = \frac{2B^2}{9 + 2B^2} \tag{3.4}$$

$$B^2 = Sk^2 + As^2 \tag{3.5}$$

Thus, when the bi-spectral properties of a signal, i.e. the skewness and asymmetry, are known, Equations (3.3-3.5) provide the necessary waveform parameters to produce a waveform time series which can be scaled to get the correct energy (in this case, the correct u_{rms}). The waveform expression can be validated by considering the harmonic amplitudes b^{n-1} and phases $(n-1)\Phi$. More on the bispectrum and the derivation of these equations can be found in Appendix A.

3.3. Wave flume experiment

3.3.1. Description of tests and data processing

In the following a brief overview of the experiment is given, more details can be found in Henriquez et al. (2014). The flume has a length of 40 m, a width of 0.8 m and a water depth of 0.5 m. In the flume a rigid single bar profile was build (see Chapter 2, Figure 2.1). The top of the bar is approximately 0.15 m below the mean water level. Granular sediment with a grain size of 0.54 mm was glued to the surface to provide bottom roughness. The hydrodynamic model scale was 1:10, which corresponds to a medium sized wave flume experiment.

The flow velocity vectors within the wave bottom boundary layer were measured with Particle Image Velocimetry (PIV) at 6 locations along the flume; 4 locations leading up to the bar crest and 2 locations between the bar crest and trough (see Henriquez et al., 2014, Figure 1). The laser sheet for PIV was inserted into the water from the water surface using a streamlined window. The camera was placed outside of the flume (flume wall is transparent). The camera had a field of view of approximately 10×10 mm^2. The camera images were processed resulting in a velocity vector for every 0.37×0.37 mm^2. The surface elevations $\eta(t)$ were measured with 7 resistance type wave gauges sampling at 200 Hz of which one was co-located with the PIV location.

Tests were carried out with wave periods of 1.0, 1.8 and 2.5 s with root-mean-square wave heights at the wave maker of 8.7, 8.4 and 8.0 cm, respectively. For the test with periods of 1.0, 1.8 and 2.5 s, the PIV system captured 132, 120 and 120 waves with sampling frequencies of 15, 15 and 10 Hz, respectively.

The velocity vectors were decomposed in a tangent and normal component on the basis of the local bottom slope at each of the 6 locations (i.e. one general slope angle per location was determined). The tangent velocity component u is positive in wave direction and the normal velocity component w is positive in the direction away from the bed (see Figure 3.1 for illustration of coordinate system).

The flow velocities of individual tests were also decomposed in different time components. Averaging over the wave phase separates the turbulent velocity com-

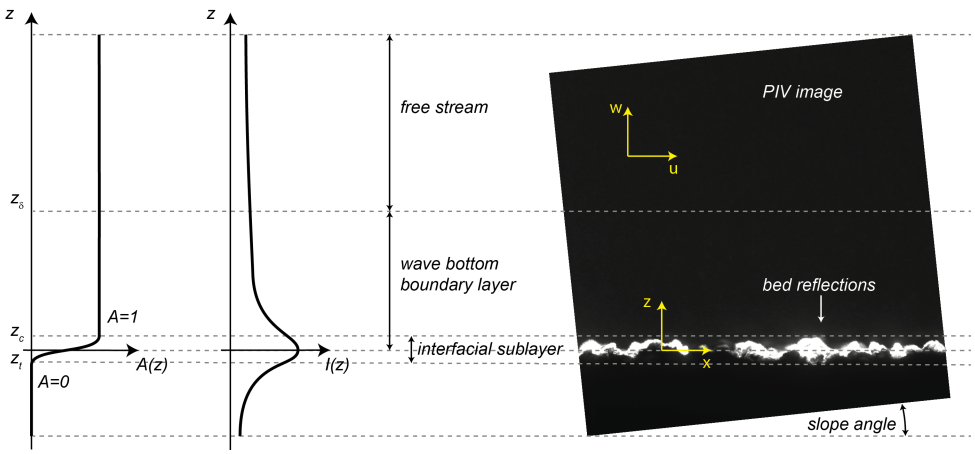

Figure 3.1: Sketch of the vertical references. The z-level was set to zero at the maximum of the horizontally spatial-averaged image intensity $I(z)$. The crest level of the roughness elements was set at $z_c = d_{50}$ and the trough level was set at $z_t = -d_{50}$. The roughness geometry function $A(z)$ is zero for $z < z_t$, one for $z > z_c$ and described by Equation 3.6 for $z_t < z < z_c$.

ponent u'. Subtracting the time-averaged component $\overline{u}$ from the phase-averaged component gives the periodic component $\widetilde{u}$. In addition, the velocity vectors of a row were averaged to obtain the spatial-averaged velocity. Furthermore,the vertical level at $z = 9$ mm is taken as the free stream based on the fact that the wbbl does not grow past this level (see Henriquez et al., 2014, Figure 8).

3.3.2. MOMENTUM-INTEGRAL METHOD

The bottom shear stresses were determined by using the "defect velocity integral" from crest to trough level (e.g., Jonsson and Carlsen, 1976; Nielsen, 1992). For the conservation of momentum in the interfacial sublayer it is necessary to consider the amount of horizontal space occupied by fluid relative to the space occupied by the bed which is described with the roughness geometry function $A(z)$ (see Figure 3.2 for profile) (Nikora et al., 2001):

$$A(z) = 0.5 + 0.5 \sin \frac{\pi}{2d_{50}} z \quad \text{for } z_c \leq z \leq z_t \tag{3.6}$$

where z_t is the trough level and z_c is the crest level. The roughness geometry function (Equation 3.6) corresponds to the space characteristics of a sinusoidal rippled bed and thus can be seen as a first order estimate. It is important to include this parameter in the momentum integral, otherwise, rapidly decelerating flow deep in the interfacial sublayer would be overestimated since it only occupies a small portion of the total horizontal space of the PIV measuring window. Finally, the time-varying bed shear stress was determined by

$$\widetilde{\tau}_b(t) = \widetilde{\tau}_{zx}(z_c, t) + \rho \int_{z_t}^{z_c} A(z) \left(\frac{\partial}{\partial t} \left(\widetilde{u}_\infty - \widetilde{u} \right) \right) dz \tag{3.7}$$

where the tilde denotes the periodic component and $\widetilde{\tau}_{zx}$ is the sum of the laminar and turbulent fluid shear stress

$$\widetilde{\tau}_{zx} = \rho\nu\frac{\partial\widetilde{u}}{\partial z} - \rho\widetilde{u'w'}. \tag{3.8}$$

Note that the advective term $-\rho\widetilde{u}\widetilde{w}$ is not included in the momentum integral. We reason that the term is negligible due to the minimal vertical orbital velocities below crest level. In addition, note that usually the free stream is taken as the the upper limit of Equation 3.7 because, in contrast to this study, there is no data available on the turbulent stresses at crest level of the bottom roughness elements (e.g. Jonsson and Carlsen, 1976). However, in this study the data is available at crest level and by choosing this upper level we also prevent contamination from the time and spatial accelerations associated with vortex tubes (see Section 2.4.8).

The velocities were measured from the free stream downto the still bed. The PIV technique estimates the velocity vectors by determining the spatial shift of tracers between two consecutive images. Every image was divided into smaller interrogation windows that can be interpreted as the "measuring volume". The width and height of the interrogation window was of the same order as the grain diameter d_{50}. This renders the vectors below the crest level of the bottom roughness elements as unreliable because the fixed bed will be included in the cross-correlation. In addition, the spatial resolution was too coarse to resolve the velocities in the interfacial sublayer between the crest and trough level of the roughness elements (see Figure 3.1 and 3.2) (Nikora et al., 2001). Consequently, the velocities at crest level are considered as the closest bottom measurements. As can be seen in Figure 3.2, the velocity attenuation at crest level was larger than 0.6 indicating that a large part of the velocity deceleration due to bed friction took place in the interfacial sublayer. Therefore, it is essential to integrate the "defect velocity integral" (Equation 3.7) down to the through level of the bottom roughness elements.

To provide the interfacial sublayer with data, the spatially-averaged vertical profiles of the horizontal velocity were interpolated from the crest level to the trough level. Velocity vectors below trough level were set to zero. The thickness of the interfacial sublayer was assumed to be $2d_{50}$ based on the visual observation in the PIV image (see Figure 3.1). The missing points were generated with spline interpolation. A spline was chosen to ensure a derivative that was smooth and continuous. It must be noted that we make the assumption that the interpolated variable tapers off to zero, which is expected for the velocity and turbulence.

3.4. Description of numerical flow model

To solve the vertical profile of the horizontal flow velocity in an oscillating flow tunnel we used the 1DV model of Uittenbogaard and Klopman (2001) and applied it in a similar fashion as Ruessink et al. (2009) and Kranenburg et al. (2012). The horizontal velocity $u(z,t)$ was determined using the horizontal momentum balance

$$\frac{\partial u}{\partial t} = -\frac{1}{\rho}\frac{\partial p}{\partial x} + \frac{\partial \tau_{zx}}{\partial z} \tag{3.9}$$

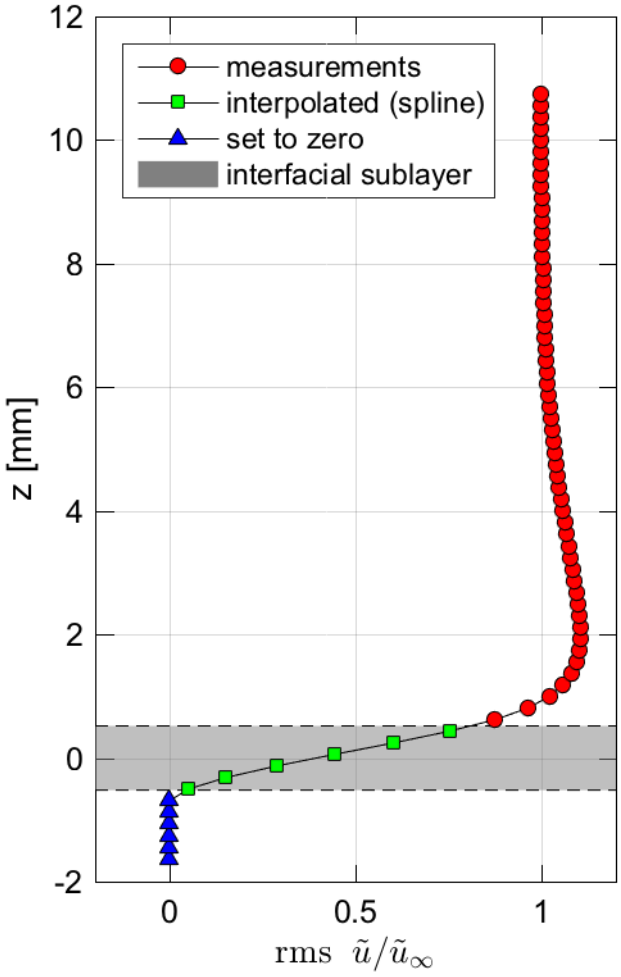

Figure 3.2: Vertical profile of the root-mean-square (rms) time-varying horizontal velocity of experiment test T=1.8s@C4.

where $\frac{\partial p}{\partial x}$ is the horizontal pressure gradient, z is the vertical coordinate, with $z = 0$ at the bed and positive upward, and τ_{zx} is the viscous and turbulent fluid stress that is calculated using the eddy viscosity concept

$$\tau_{zx} = \rho\,(\nu_t + \nu)\,\frac{\partial u}{\partial z} \tag{3.10}$$

The turbulent eddy viscosity ν_t is calculated by

$$\nu_t = C_\mu \frac{k^2}{\epsilon} \tag{3.11}$$

where $C_\mu = 0.09$, k the fluid turbulent kinetic energy and ϵ its dissipation rate. The variables k and ϵ are calculated from the standard k-ϵ turbulence equations (Kranenburg et al., 2012; Launder and Spalding, 1974; Rodi, 1987). The lower boundary is defined at the crests of the roughness elements of the bed where a partial slip condition is applied under the assumption that locally: the velocity profile is logarithmic, the quadratic friction law applies and there is equilibrium between production and dissipation:

$$\frac{u(z)}{u_*} = \frac{1}{\kappa}\ln\left(\alpha + \frac{z}{z_0}\right) \quad ; \quad u_*^2 = \left(\nu_t \frac{\partial u}{\partial z}\right)\Big|_{z=0} \quad ; \quad P_k|_{z=0} = \epsilon|_{z=0} \tag{3.12}$$

Here, the values of the friction velocity, turbulent kinetic energy and its dissipation rate were calculated following Hinze (1975) and Jackson (1981):

$$\frac{\partial u}{\partial z}\Big|_{z=0} = \frac{u_*}{9\kappa z_0} \quad ; \quad k|_{z=0} = \frac{u_*^2}{\sqrt{C_\mu}} \quad ; \quad \epsilon|_{z=0} = \frac{u_*^3}{9\kappa z_0} \tag{3.13}$$

where κ is the Von Karman constant, 0.41, and z_0 is the roughness length scale for hydraulically rough flow related to the Nikuradse roughness height k_N with $z_0 = k_N/30$. At the upper boundary a no-shear condition is applied were the time-varying horizontal pressure gradient is equal to the applied time-varying free-stream horizontal velocity acceleration. Hence, a steady flow is allowed to develop without any friction at the upper boundary.

The wave period and amplitude of the primary harmonic were set to 6.5 s and 1.0 m/s, respectively. The combination of wave period and orbital velocity resembles field conditions where the wave Reynolds numbers are $RE \geq 1 \times 10^6$ (see Figure 3.3 and Table 3.1). Here, the wave Reynolds number is defined as $RE = 2\,\mathrm{std}(u)/\omega\nu$ where std stands for standard deviation and the wave friction factors were determined by $f_w = \mathrm{std}(\tau_b)/\frac{1}{2}\rho\,\mathrm{std}(|u|u)$.

The velocity skewness and asymmetry ranged from 0 to 1 with intervals of 0.5 leading to 9 different combinations. The waveforms were made using Equation 3.2-3.5. In addition, the Nikuradse roughness height was varied using a value of 0.35 mm and 10 mm. Thus, in total 18 runs were carried out. The model was run with a time step of $\Delta t = 6.5 \times 10^{-3}$ s for a duration of 650 s. The velocity at $z = 0.20$ m was taken as the reference free-stream velocity.

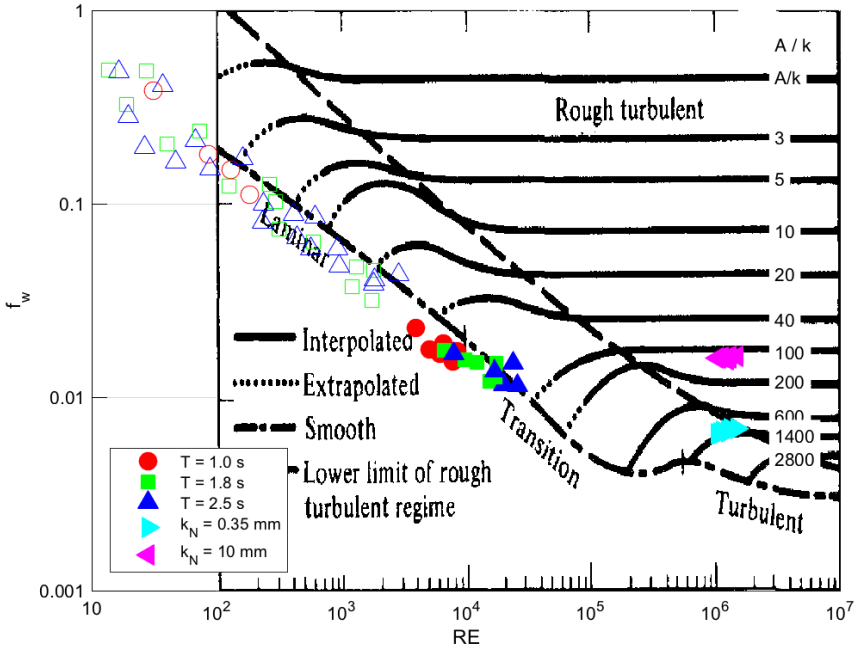

Figure 3.3: Wave friction factors in the Stanton diagram from Kamphuis (1975). The circle, square and upward triangle markers correspond to the laboratory wave flume tests. The filled markers correspond to the friction factor of the primary harmonic and the open markers correspond to higher harmonics. The left and right triangle markers correspond to the numerical model tests.

nr	$k_N(mm)$	$T(s)$	$U_1(m/s)$	Sk_∞	As_∞	a/k_s	$RE \times 10^6$
1	0.35	6.5	1.0	0.0	0.0	2957	1.04
2	0.35	6.5	1.0	0.0	0.5	3038	1.09
3	0.35	6.5	1.0	0.0	1.0	3269	1.27
4	0.35	6.5	1.0	0.5	0.0	3038	1.09
5	0.35	6.5	1.0	0.5	0.5	3117	1.15
6	0.35	6.5	1.0	0.5	1.0	3342	1.32
7	0.35	6.5	1.0	1.0	0.0	3269	1.27
8	0.35	6.5	1.0	1.0	0.5	3342	1.32
9	0.35	6.5	1.0	1.0	1.0	3549	1.49
10	10.0	6.5	1.0	0.0	0.0	104	1.04
11	10.0	6.5	1.0	0.0	0.5	106	1.09
12	10.0	6.5	1.0	0.0	1.0	114	1.27
13	10.0	6.5	1.0	0.5	0.0	106	1.04
14	10.0	6.5	1.0	0.5	0.5	109	1.15
15	10.0	6.5	1.0	0.5	1.0	117	1.32
16	10.0	6.5	1.0	1.0	0.0	114	1.27
17	10.0	6.5	1.0	1.0	0.5	117	1.32
18	10.0	6.5	1.0	1.0	1.0	124	1.49

Table 3.1: Overview of numerical model test conditions

The upper boundary was set at a height of 0.21 m which is approximately equal to 3-4 times the wbbl layer thickness and prevents interference between the upper boundary and the wbbl development. The wbbl thickness δ is defined as the distance from the bed to the point of maximum velocity overshoot and was estimated using the relationship between δ/k_N and a/k_N (Fredsøe and Deigaard, 1992):

$$\frac{\delta}{k_N} = 0.09 \left(\frac{a}{k_N} \right)^{0.82} \quad . \tag{3.14}$$

3.5. Results

3.5.1. Measurements - laminar flow regime

Bed shear stresses of the measurements were determined using the defect velocity integral (Equation 3.7). The wave friction factors were determined by $f_{w,lam} = \tau_{b,n,max}/\frac{1}{2}\rho U_n^2$ and the wave Reynolds numbers by $RE_{lam} = U_n^2/\omega_n \nu$ where U is the velocity amplitude and the subscript n denotes the harmonic component. All the friction factors fall close to the theoretical line of laminar flow $f_w = 2/\sqrt{RE}$ (Figure 3). The relative roughness a/k_N (using $k_N = 2.5d_{50}$) of the tests ranged from 19 to 87. The tests fall in the expected roughness region indicated in the diagram of Kamphuis (1975). It must be noted that the relative roughness in the diagram of Kamphuis (1975) is defined using $k_N = 2d_{90}$ and thus we assume here that $2.5d_{50} \approx 2d_{90}$.

The friction velocity phase lead was determined as follows. First, the friction

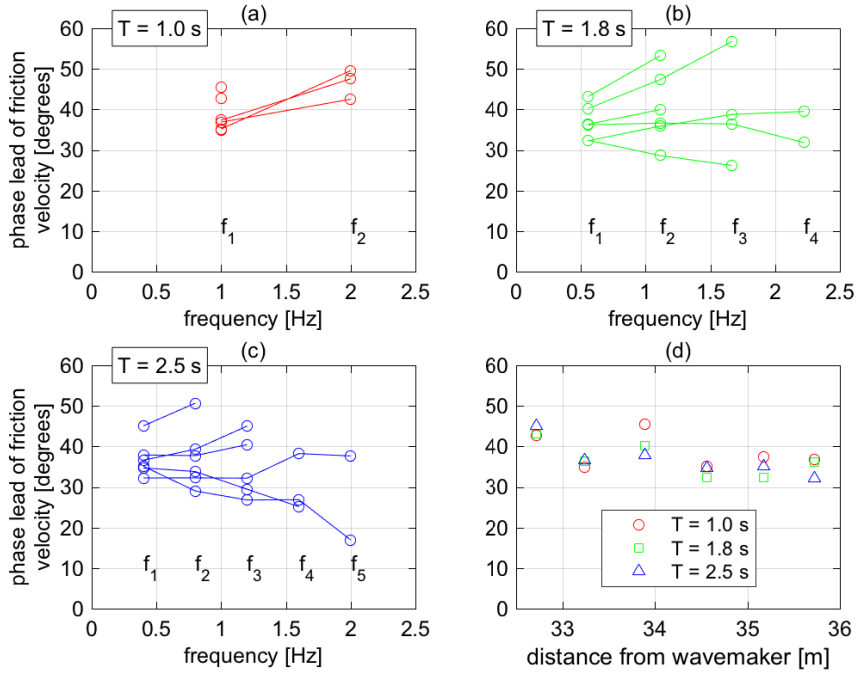

Figure 3.4: Friction velocity decomposition of the experiment tests. (a, b, c) Phase lead of the friction velocity components as a function of frequency. The lines the panels correspond to the different locations. (d) Phase lead of the primary friction velocity components as a function of the distance from the wave maker.

velocity was derived from the bed shear stresses using Equation 3.1 with $\alpha = 1$. Second, the phases of the harmonics were determined by applying the FFT on the time series of the friction velocity and free-stream flow velocity. Hereafter, the phase lead was determined by subtracting the phase of the free-stream velocity component from the friction velocity component

$$\varphi_{n,u_*} = \theta_{n,u_*} - \theta_{n,u_\infty} \tag{3.15}$$

The friction velocity phase lead of the first harmonics ranged from 30 to 45 degrees with an average of approximately 37 degrees (see Figure 3.4a-c). No general trend could be detected for the phase lead of the higher harmonics. Despite the scatter, the difference between the first and corresponding second harmonic was often less than 10 degrees. The friction velocity phase leads of the first harmonics varied with measurement location (Figure 3.4d) and a maximum difference of approximately 15 degrees was found between locations.

The relative amplitude of the surface elevation and free-stream velocity of the measurements agreed well with the amplitude coefficient b from Equation (3.4) (Figure 3.5). Deviations from Equation (3.4) were found after the bar crest for test with

periods of 1.8 and 2.5 s. The harmonic phases (θ_n) of the free-stream velocity measurements agreed well with the harmonic phases from Equation (3.2) (Figure 3.6).

3.5.2. Numerical modeling - turbulent flow regime

Bed shear stresses were calculated by the numerical model. The friction velocities were determined using Equation (3.1) with the α values found for the purely sinusoidal tests. For the sinusoidal tests with $k_N = 0.35$ mm (10 mm) the velocity was raised to the power of $\alpha = 1.55$ (1.64).

For the tests with $k_N = 0.35$ mm, the amplitudes of the friction velocity increased over the first three harmonics while a decline can be observed for the fifth harmonic (Figure 3.7a). For tests with $k_N = 10$ mm, the amplitudes of the friction velocity increased steadily over the harmonic components (Figure 3.7b). For all tests, the friction velocity amplitude of the second harmonics was about 1.2 times larger than the amplitude of the first harmonics. There were no large differences between the friction velocity phase leads for tests with $k_N = 0.35$ mm and 10 mm. The friction velocity phase leads of the first harmonics were approximately 18 degrees (Figure 3.7c, d). The second harmonics had phase leads that were relatively lower, ranging from 14 to 18 degrees. The phase leads of the third, fourth and fifth harmonics had some scatter, however, no trend was observed over these frequencies.

3.6. Discussion

The consecutive phase leads of the friction velocity components in the experiment were approximately 37 degrees instead of the 45 degrees for the analytic solution by Stokes (1851). This may be explained by the fact that multiple roughness elements extended well into the boundary layer where they were in contact with fluid that had relatively low velocity phase leads. In the numerical modeling results, the friction velocity phase leads of the first harmonics were around 18 degrees. When compared to past measurements results, see e.g. van der A et al. (2011, Figure 6), we would expect the friction velocity phase lead of tests with $a/k_N \approx 100$ to be between 20 to 30 degrees. The higher harmonic phase leads were generally a few degrees lower than the first harmonic. These results support the suggestion of Henderson et al. (2004) for applying a constant friction velocity phase lead for consecutive harmonics.

Equation 3.2 is a good approximation for the shape of the regular waves encountered over the bar in the experiment, which spanned a broad range of skewness and asymmetry. The differences found for waves after the bar crest were mainly caused by a mismatch in amplitude (see Figure 3.5) which may be caused by wave breaking. The use of a waveform parameter Φ seems justified since the phases of the higher harmonics can be described by $\theta_n = (n-1)\Phi$ (see Figure 3.6).

Following Nielsen (1992), the bed shear stress by an oscillatory flow with an arbitrary non-sinusoidal waveform can be calculated by summing the individual solutions for laminar oscillatory flow (e.g., Batchelor, 2000):

$$\tau_b(t) = \sum_{n=1}^{N} \rho\sqrt{n\omega\nu}u_{b,n} \quad ; \quad u_{b,n}(t) = \Re\{u_{\infty,n}e^{i\varphi}\} \tag{3.16}$$

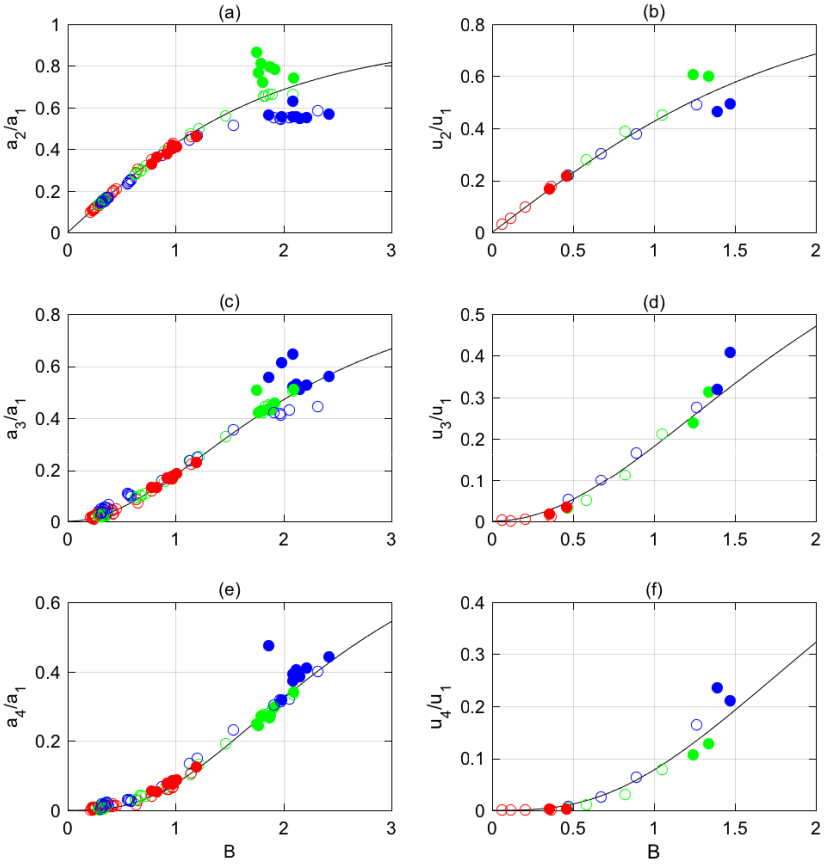

Figure 3.5: (a, c, e) Relative amplitude of the surface elevation components as a function of $B = \sqrt{Sk^2 + As^2}$ (Equation 3.5). (b, d, f) Relative amplitude of the free-stream velocity components as a function of B. The colors red, green, blue correspond to test with periods of 1.0 s, 1.8 s, 2.5 s, respectively. Open and closed markers indicate measurements seaward and shoreward of the bar crest, respectively. The black solid line is the relative amplitude b^{n-1} where $b = \sqrt{\frac{2|B|^2}{9+2|B|^2}}$ (Equation 3.4).

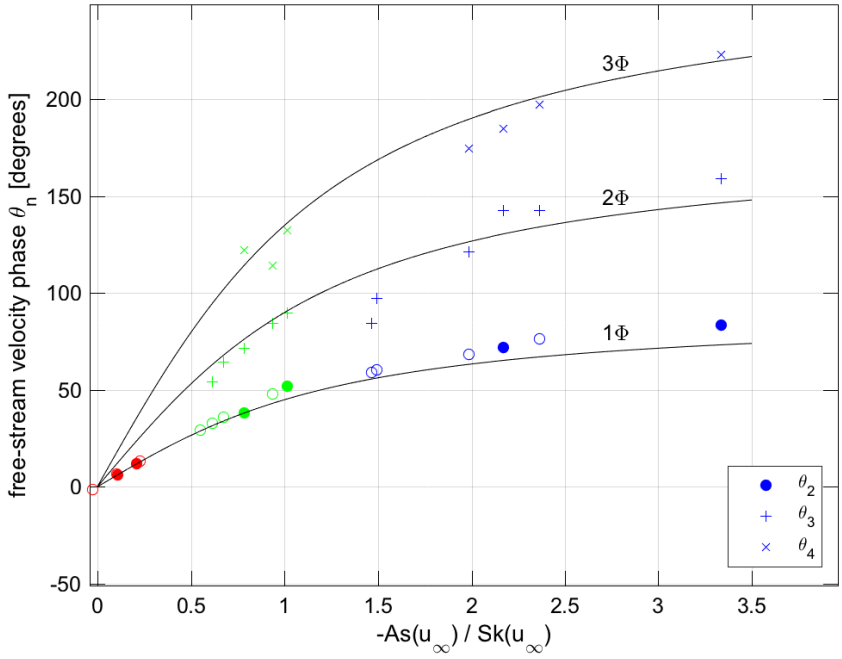

Figure 3.6: The phase of the free-stream velocity components relative to the first harmonic as a function of $-As(u_\infty)/Sk(u_\infty)$. The colors red, green, blue correspond to test with periods of 1.0 s, 1.8 s, 2.5 s, respectively. Open and closed markers indicate measurements seaward and shoreward of the bar crest, respectively. The solid lines represent $(n-1)\Phi$ where the waveform parameter is given by $\Phi = \tan^{-1}\left(\frac{-As}{Sk}\right)$ (Equation 3.3).

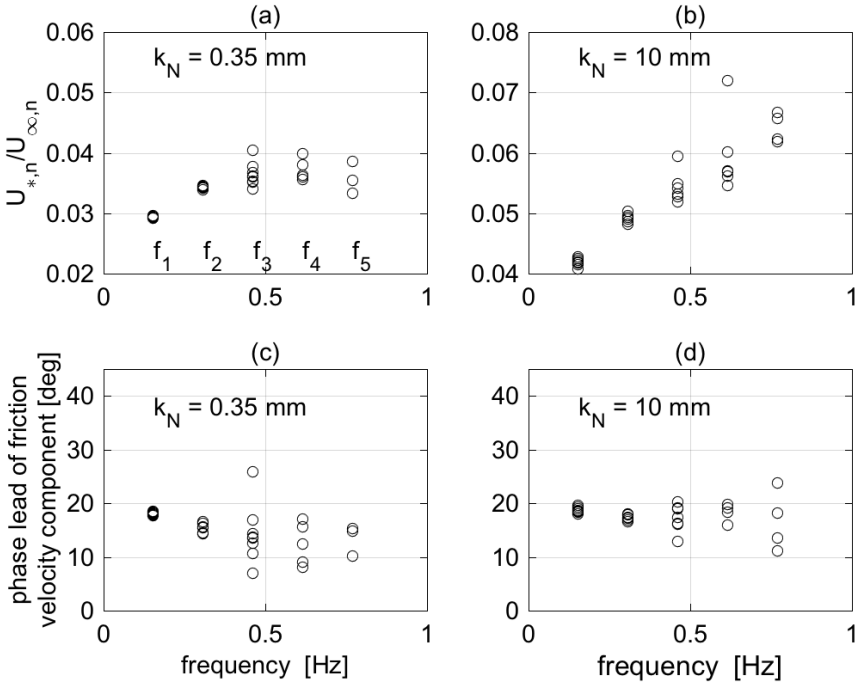

Figure 3.7: Decomposition of the friction velocity for the numerical modeling tests. (a, c) Relative amplitude and phase lead of the friction velocity component for the tests with $k_N = 0.35$ mm. (b, d) Relative amplitude and phase lead of the friction velocity component for tests with $k_N = 10$ mm.

where $u_{\infty,n}$ is the free-stream velocity component that is described by Equation (3.2) and φ is the friction velocity phase lead. The bed shear stress skewness of the experiment tests was replicated with a r^2 (coefficient of determination) of 0.94 predicted by using $\varphi = 37$ degrees in Equation (3.16) and using Equation (3.2) to construct the free-stream velocity harmonics (Figure 3.8a). The differences with the experiment data were generally less than 10%. Almost all deviations larger than 10% were found for the experiment tests with a period of 1 s, which had relatively low skewness and asymmetry.

In the numerical modeling results, the amplitudes of the friction velocity were still mildly frequency dependent for consecutive harmonics. However, in practice it is convenient to choose for a frequency-independent friction factor and a quadratic expression (i.e. $\alpha = 2$) as proposed by Terrile et al. (2009b),

$$\tau_b(t) = \frac{1}{2}\rho f_w |u_b| u_b \quad ; \quad u_b(t) = \Re\{u_\infty e^{i\varphi}\} \tag{3.17}$$

where u_∞ is the free-stream velocity and φ is the friction velocity phase lead. The wave friction factor f_w is a constant that can be calculated using the formula of Swart (1974). The bed shear stress skewness of the numerical model data was replicated with a r^2 of 0.91 by using a phase lead of 18 degrees in Equation (3.17) and using Equation 3.2 to construct the free-stream velocity (Figure 3.8b).

Equations (3.16) and (3.17) describe a linear relationship between the friction velocity skewness and the free-stream velocity asymmetry (see Figure 3.9). This also accounts for the experimental data and the numerical modeling results. Note that the experimental tests with periods of 1 s show large scatter in Figure 3.9 because the velocity asymmetries were relatively low (close to zero) and, therefore, the ratio of asymmetry to skewness was susceptible to measurement error. Overall, these findings confirm the theories of Nielsen (1992, Equation 1.2.17) and Henderson et al. (2004, Section 5.1). In addition, these findings support the use of Equation (3.16) and (3.17) which offer a simple way of estimating the time-varying bed shear stress from the free-stream velocity. Moreover, Abreu et al. (2010) derived an analytical formulation for Equation (3.2) and, in combination with Equation (3.3-3.5) (Malarkey and Davies, 2012), the free-stream velocity signal can be easily translated into the bed shear stress signal (e.g., Dubarbier et al., 2015).

3.7. Conclusions

The shape of the surface elevation and horizontal velocity of nonlinear regular waves can be adequately described using two shape parameters, i.e. one coefficient for the harmonic amplitudes and one parameter for the harmonic phases as was suggested by Abreu et al. (2010). These parameters can easily be derived from the skewness and asymmetry of the signal.

Experimental bed shear stress data agreed with the analytic solution for laminar oscillatory flow in terms of frequency dependent amplitudes and frequency independent phase leads. However, the phase leads of the friction velocity components were approximately 37 degrees instead of 45 degrees, which may be related to the fact that the bed was not smooth.

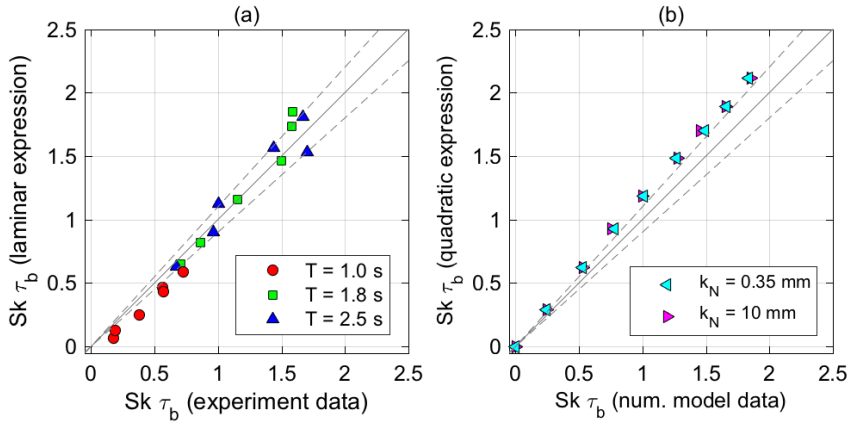

Figure 3.8: Skewness off the bed shear stress. (a) Comparison between the laminar expression, Equation (13), and the experiment data. (b) Comparison between the quadratic expression, Equation (14), and the numerical modeling results.

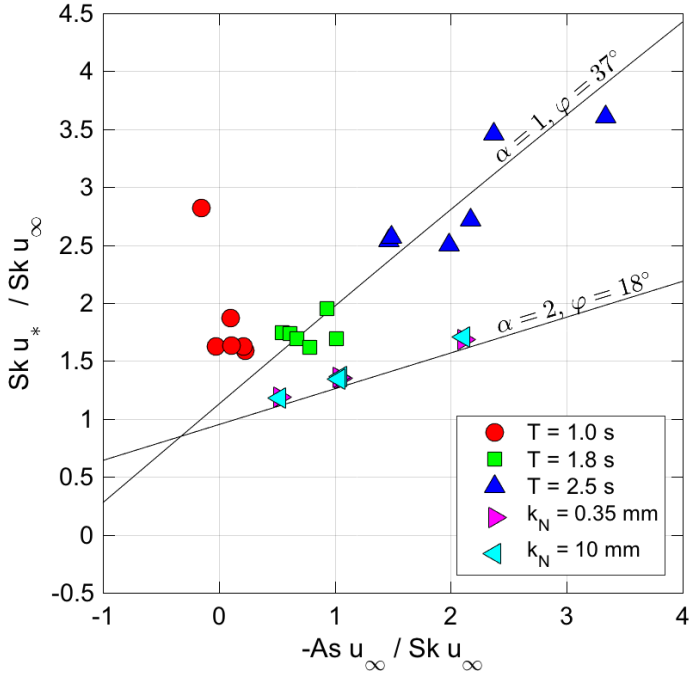

Figure 3.9: The transfer of free-stream velocity asymmetry to friction velocity skewness. The solid lines represent Equation (3.16) and (3.17).

Based on numerical modeling results of purely sinusoidal tests in the turbulent regime it appeared that the relation between free-stream velocity and bed shear stress is not quadratic and is closer to $\tau_b \sim u^{1.6}$. However, when the quadratic assumption is applied, the error made in the skewness of the bed shear stress was relatively small. Furthermore, in the numerical model tests the phase leads of consecutive friction velocity components did not deviate more than a few degrees.

The experimental and numerical data confirm that under nonlinear regular waves the free-stream velocity asymmetry leads to bed shear stress skewness. This process can be conveniently modeled for practical applications by summing the solutions of the harmonic components or using the analytic expressions of Abreu et al. (2010) and Malarkey and Davies (2012).

4

Mean bed shear stress by nonlinear surface waves

Even when the time-averaged component of the bed shear stress is small compared to the time-varying component, it can have a large effect on the net bedload in the nearshore. This chapter studies the time-averaged bed shear stress under regular surface waves traveling over a fixed single bar profile in a laboratory wave flume. The waves transformed to skewed and asymmetric and broke after passing the bar crest. The bed shear stresses were derived from flow velocity measurements of the wave bottom boundary layer. An analytic quasi-1DV model was used as a tool to distinguish the relevant processes that govern the time-averaged bed shear stress. The time-averaged bed-shear stresses by unbroken waves were mainly governed by the shoreward-directed wave Reynolds stress and seaward-directed pressure force to compensate the Stokes drift. For broken waves an additional force becomes apparent that was not further investigated. To determine the impact of the time-averaged bed shear stress on sediment transport we utilized the well-established power relation between bed shear stress and bedload. The contribution of the time-averaged bed shear stress to the net bedload ranged from 20% to 100% depending on the wave shape and dissipation by wave breaking. When the wave skewness and asymmetry were relatively large, the contribution of the time-averaged bed shear stress to the net bedload reduced to 20%. Furthermore, the free-stream velocity at the top of the wave bottom boundary layer was an unsuitable proxy for the time-averaged bed shear stress.

4.1. Introduction

Waves in the nearshore generate bed shear stresses through a variety of processes, which can mobilize sediments and, thus, are important for the coastal morphology. The role of bed shear stresses during an onshore sandbar migration in the nearshore has been investigated in the last three decades. Past experiments have shown that

bedload is strongly related to the 1.5 power of the bed shear stress. Due to this power relationship, a skewed bed shear stress will result in a nonzero net bedload (Bowen, 1980). Therefore, many studies have focused on the relation between wave shape and the time varying bed shear stress. The time-averaged component of the bed shear stress is small compared to the time-varying component. However, it can have a large effect on the total net bedload despite the relatively small magnitude.

Processes such as bed friction, mass flux and wave breaking all govern the time-averaged bed shear stress. The downward flux of horizontal momentum into the wave bottom boundary layer (wbbl), which is referred to as 'wave Reynolds stress', generates a near-bed current in the direction of wave propagation (Longuet-Higgins, 1953). In addition, the friction between the bed and a non-sinusoidal oscillatory water motion leads to a nonzero time-averaged wave-related turbulent stress, which drives a current in the wbbl against the direction of wave propagation (Holmedal and Myrhaug, 2009; Kranenburg et al., 2012; Trowbridge and Madsen, 1984). Thus, in essence, the bed friction by streaming balances the nonzero time-averaged wave-related turbulent stress. Kranenburg et al. (2012) coined this process 'wave shape streaming'.

A process outside the wbbl is the transport of mass in the direction of wave propagation referred to as Stokes drift (Phillips, 1977; Stokes, 1851). In case of a closed boundary, the depth-averaged velocity is zero and a return flow must exist. In addition, the roller of a breaking wave generates a mass flux and a surface stress in the direction of wave propagation (Duncan, 1981; Svendsen, 1984). The forces exerted by progressive wave streaming on the bed and by the rollers on the surface are balanced through a water level gradient and a bed shear stress contribution.

Hoefel and Elgar (2003), Henderson et al. (2004), Hsu et al. (2006), Ruessink et al. (2007b) and Dubarbier et al. (2015) hindcasted the same onshore sand bar migration event that was observed during the Duck94 field experiment using either wave-averaged or intra-wave models and the combined effort reveals the dominant transport processes remains inconclusive. Namely, the onshore bar migration could be modeled by either including wave skewness or asymmetry, however, including both works best for the whole cross-shore profile. In addition, the various methods of including the time-averaged free-stream and wbbl currents had a large impact on the results. Furthermore, free model parameters leave enough room to compensate for missing physics. Therefore, the theoretical concepts and models cannot be validated with existing field data only and the role of the bed shear stresses during an onshore sandbar migration cannot be properly assessed (see also Hsu et al., 2006). In addition, bed shear stress measurements under progressive waves are scarce (Boers, 2005).

In this chapter we present the time-averaged bed shear stresses that were derived from flow measurements of waves traveling over a fixed single-bar profile in a wave flume. The primary objective is to investigate the potential contribution of the time-averaged bed shear stress to the net bedload in the nearshore. To provide insight in the contribution of the different processes (i.e., wave Reynolds stress, turbulent stress, Stokes drift and the horizontal pressure gradient) a simple analytic model will be compared with the measurements.

First we elaborate on the relation between the contribution of the time-averaged bed shear stress and the net bedload in Section 4.2 on methodology. Hereafter, a brief description is given on the experimental data in Section 4.3. The analytic model is described in Section 4.4. Results, discussion and conclusions are presented in Section 4.5, 4.6 and 4.7.

4.2. METHODOLOGY

The flux of particles that roll along the bed is called 'bedload' (Bagnold, 1966). Here, the sand particles are transported over the bed by the shearing of the fluid over the bed. Empirical findings from the experiments of Meyer-Peter and Müller (1948) and Wilson (1987), showed that bedload q_b was related to the bed shear stress τ_b by

$$\overline{q}_b \sim \overline{\tau_b|\tau_b|^{0.5}} \tag{4.1}$$

where the overbar indicates averaging over time. Bagnold (1966) came to a similar conclusion based on a physically based derivation. Note that this relation is based on knowledge from sediment transport by 'steady' flows such as rivers and, in the absence of contrary evidence, is also applied for sediment transport by the 'unsteady' orbital wave motion (see e.g. Bailard, 1981, 1982; Bailard and Inman, 1981; Bowen, 1980; Ribberink, 1998; Roelvink and Stive, 1989). To identify and analyze the contribution of the time-averaged bed shear stress to the odd bed shear stress moment, $\overline{\tau_b|\tau_b|^{0.5}}$, the bed shear stress is decomposed in a time-averaged and time-varying component:

$$\tau_b = \overline{\tau}_b + \widetilde{\tau}_b \tag{4.2}$$

Decomposition of the odd bed shear stress moment $\overline{\tau_b|\tau_b|^{0.5}}$ is possible by assuming that $|\overline{\tau}_b| < |\widetilde{\tau}_b|$ and using a Taylor expansion (Bowen, 1980):

$$\overline{\tau_b|\tau_b|^{0.5}} = \overline{\widetilde{\tau}_b|\widetilde{\tau}_b|^{0.5}} + \frac{3}{2}\overline{\tau}_b\overline{|\widetilde{\tau}_b|^{0.5}} + \cdots \tag{4.3}$$

where the term on the left-hand-side is referred to as the "odd bed shear stress moment", the first term on the right-hand-side represents the "nonlinear contribution" due to the nonlinearity of the waves and the second term on the right-hand-side represents the "mean contribution" due to the interaction between the time-averaged and the time-varying bed shear stress component.

4.3. MEASUREMENTS OF BED SHEAR STRESSES

This chapter uses the flow velocity data from the experiments conducted in a medium sized wave flume described in Henriquez et al. (2014). In addition, this chapter builds on the data processing methods (including data interpolation), symbols and coordinate systems described in Section 3.3.

The time-averaged bed shear stress is determined by integrating the time-averaged fluid shear stress over the interfacial sublayer which is located between the crest and trough of the roughness elements (Nikora et al., 2001). In the interfacial sublayer,

the amount of fluid is described by the roughness geometry function $A(z)$, see Equation 3.6. The integral for the time-averaged bed shear stress is

$$\overline{\tau}_b = \overline{\tau}_{zx}(z_c) - \int_{z_t}^{z_c} A(z) \left(\frac{\partial \overline{\tau}_{zx}}{\partial z} \right) dz \tag{4.4}$$

where the bar denotes the mean component, z_t is the trough level and z_c is the crest level and τ_{zx} is the fluid shear stress (viscous and turbulent)

$$\overline{\tau}_{zx} = \rho\nu \frac{\partial u}{\partial z} - \rho\overline{u'w'}. \tag{4.5}$$

Note that the wave Reynolds stress $-\rho\widetilde{\tilde{u}\tilde{w}}$ is not included in Equation 4.4. We reason that the term is negligible due to the small periodic vertical velocities below crest level.

4

4.4. Description of the analytic model

The applied model uses parts from the analytic quasi-1DV model of Roelvink and Reniers (1994) (see Reniers et al. (2004a) for the complete model description). The model used in the present study includes only non-breaking wave orbital processes and Stokes drift, and does not include alongshore processes nor wind processes since the latter processes did not occur in the experiments.

The vertical distribution of the cross-shore flow is based on the 3 layer conceptual model of De Vriend and Stive (1987) consisting of a top layer above wave through level, a middle layer and a wave bottom boundary layer (wbbl). The water depth below wave trough level h_t includes the middle layer and wbbl and is determined by

$$h_t = h - \frac{H_{rms}}{\sqrt{2}} \tag{4.6}$$

where H_{rms} is the root-mean-square wave height and h is the mean water depth. The model utilizes a non-dimensional depth

$$\sigma = \frac{z}{h_t} \tag{4.7}$$

where z is positive upward from the bottom level. The momentum balance of the middle layer is governed by the fluid shear stress τ_{zx} and a depth invariant forcing F_x

$$\frac{\partial \tau_{zx}}{\partial \sigma} = F_x \tag{4.8}$$

The depth invariant forces F_x consist of a pressure force due to a horizontal water level gradient gradient, $F_x = -\rho g \frac{\partial \bar{\eta}}{\partial x}$. Integration of Equation 4.8 along the σ-axis and applying no surface stresses gives

$$\tau_{zx} = -F_x(1 - \sigma) \tag{4.9}$$

In the wbbl the wave Reynolds stress is defined as $\tau_{zx,WRS} = -\rho\widetilde{\tilde{u}\tilde{w}}$ and decreases to zero at the bed. The time-averaged wave energy dissipation $\bar{D}_f$ in the

wave bottom boundary layer due to friction between the bed and the oscillatory flow is related to the wave Reynolds stress as

$$-\rho\left(\overline{\tilde{u}\tilde{w}}\right)_{\infty} = \frac{\overline{D}_f}{c} \tag{4.10}$$

where c is the wave celerity. The time-averaged wave energy dissipation of laminar oscillatory flow is calculated by

$$\overline{D}_f = 0.8\frac{2}{3\pi}\rho f_w u_{orb}^3 \tag{4.11}$$

where $f_w = 2\sqrt{\omega\nu}/u_{orb}$ is the laminar wave friction factor (Jonsson, 1966). Note that the factor of 0.8 is used to account for laminar flow. In the model, wave Reynolds stress is assumed to decrease linearly to zero across the wave boundary layer (Fredsøe and Deigaard, 1992).

$$\rho\frac{\partial\tilde{u}\tilde{w}}{\partial\sigma} = -\frac{1}{\delta}\frac{\bar{D}_f}{c} \tag{4.12}$$

where δ is the thickness of the wbbl (scaled with the water depth h_t defined as

$$\delta = \frac{2.28}{h_t}\sqrt{\frac{2\nu}{\omega}} \tag{4.13}$$

which is equal to the vertical distance from the bottom to the maximum velocity amplitude of a laminar oscillatory boundary layer. Including the wave Reynolds stress in the horizontal momentum balance results in the force balance of the wbbl

$$\tau_{zx} = -F_x\left(1-\sigma\right) + \frac{\bar{D}_f}{c}\frac{\left(\delta-\sigma\right)}{\delta} \tag{4.14}$$

The relation between the shear stress and the vertical gradient of the mean horizontal velocity is modeled using the turbulent eddy viscosity ν_t,

$$\tau_{zx} = \rho\frac{\nu_t}{h_t}\frac{\partial u}{\partial\sigma} \tag{4.15}$$

The turbulent eddy viscosity ν_t is described using two parabolic shape functions, see (Reniers et al., 2004b, Appendix A) for more details. The parabola that extends from the bottom to the wave trough level has a depth-averaged eddy viscosity equal to

$$\bar{\nu}_t = \frac{1}{6}\kappa h_t\sqrt{gh_t\left|\frac{\partial\eta}{\partial x}\right|} \tag{4.16}$$

The second parabola extends over the wbbl for the purpose to increase the depth-averaged eddy viscosity over the wbbl. Since viscous stresses were dominant in the wbbl we fixed the additional depth-averaged eddy viscosity $\bar{\nu}_{t,wbbl}$ to $1\times10^{-6}\ m^2/s$ (Henriquez et al., 2014).

The combination of Equation 4.14, 4.15, 4.16, and the parabolic shape functions for the turbulent eddy viscosity can be solved analytically which provides the velocity profile and bottom shear stress (see Reniers et al., 2004b, Appendix B). The model output will be compared to the measurements to aid in the interpretation of the physical processes.

4.5. Results

4.5.1. Velocity profiles

In this section we elaborate on the measured and modeled velocity profiles in the wbbl. See Figure 4.1 to 4.6 for the profiles. Note that the thickness of the interfacial sublayer ($2d_{50} \sim 1$ mm) is in the same order of magnitude as the wbbl thickness ($1 - 5$ mm, Henriquez et al. (2014)) meaning that a significant part of the profile close to the bottom is obtained through interpolation. For example, at T=1.8s@C3, the only positive time-averaged velocities were found below the crest level of the roughness elements and thus are a result of interpolation.

Among the profiles were the typical positive wbbl streaming profiles that were most often found for tests with periods of 1 s (see e.g., T=1.0s@C4 in Figure 4.4). Negative velocities in the wbbl were most often found for tests with the larger periods of 1.8 s and 2.5 s (see e.g., T=1.8s@C4 in Figure 4.4). The model predicted the typical positive wbbl streaming profiles for all tests.

4.5.2. Bed shear stress

The vertical profiles of the viscous and turbulent stresses are shown in Figure 4.1 to 4.6. At crest level, the viscous and turbulent stresses were of comparable magnitude and often in opposite direction (see e.g. T=1.8s@C4 in Figure 4.4).

The time-averaged bed shear stresses (determined with Equation 4.4) were mainly positive (shoreward) with the exception at location C6 (see Figure 4.7). The maximum time-averaged bed shear stress was found at C4 (near the bar crest) and the minimum was found at C6 (near the bar trough). Generally, the time-averaged bed shear stresses increased from the wavemaker to the bar crest, and decreased from the bar crest to the bar trough. The maximum magnitude of the time-averaged bed shear stress was 0.03 Pa, which was two orders of magnitude lower than the maximum magnitude of the time-varying bed shear stress (1.3 Pa). Remarkably, for tests with periods of 1.8 s and 2.5 s the time-averaged bed shear stress at C2 was lower than at C1.

4.5.3. The odd 1.5th bed shear stress moment

Figure 4.7 shows the bed shear stress moments over the bar. In general, the odd bed shear stress moment $\overline{\tau_b|\tau_b|^{0.5}}$ increased from location C1 to C4 and decreased from C4 to C6. Thus, a well-defined maximum existed over the bar crest (see Figure 4.8). There were little differences between tests with periods of 1.8 s and 2.5 s. At the bar crest, the odd moment of the test with period of 1 s was half of the odd moment of the tests with periods of 1.8 s and 2.5 s.

The oscillatory contribution, $\overline{\widetilde{\tau}_b|\widetilde{\tau}_b|^{0.5}}$, and the mean current contribution, $\frac{3}{2}\overline{\tau}_b\overline{|\widetilde{\tau}_b|^{0.5}}$, followed a similar distribution as the odd moment with a maximum at C4. At this location, the mean contribution was approximately, 50%, 20%, 25%, for tests wit periods of 1.0 s, 1.8 s, 2.5 s, respectively.

In all, the mean contribution $\frac{3}{2}\overline{\tau}_b\overline{|\widetilde{\tau}_b|^{0.5}}$, to the odd moment of the bed shear stress $\overline{\tau_b|\tau_b|^{0.5}}$ was generally smaller than the oscillatory contribution $\overline{\widetilde{\tau}_b|\widetilde{\tau}_b|^{0.5}}$, however, of similar order of magnitude. At the bar crest, mean contribution $\frac{3}{2}\overline{\tau}_b\overline{|\widetilde{\tau}_b|^{0.5}}$ was in the

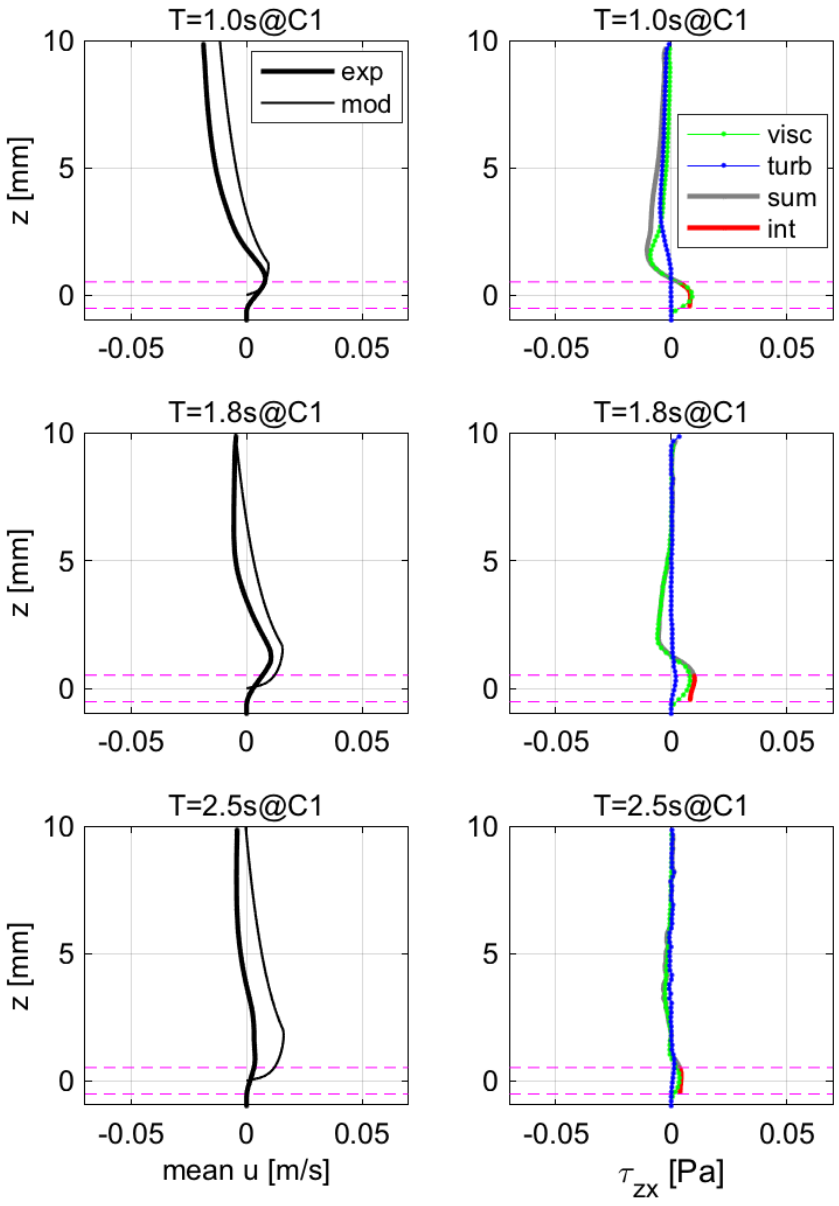

Figure 4.1: Vertical profiles at C1. Left panels, vertical profiles of the time-averaged horizontal velocity of measurements (thick line) and model (thin line). Right panels, viscous shear stress (green), turbulent shear stress (blue), sum of the shear stresses (gray) and Equation 4.4 (red). The horizontal dashed lines mark the crest and trough level of the interfacial sublayer.

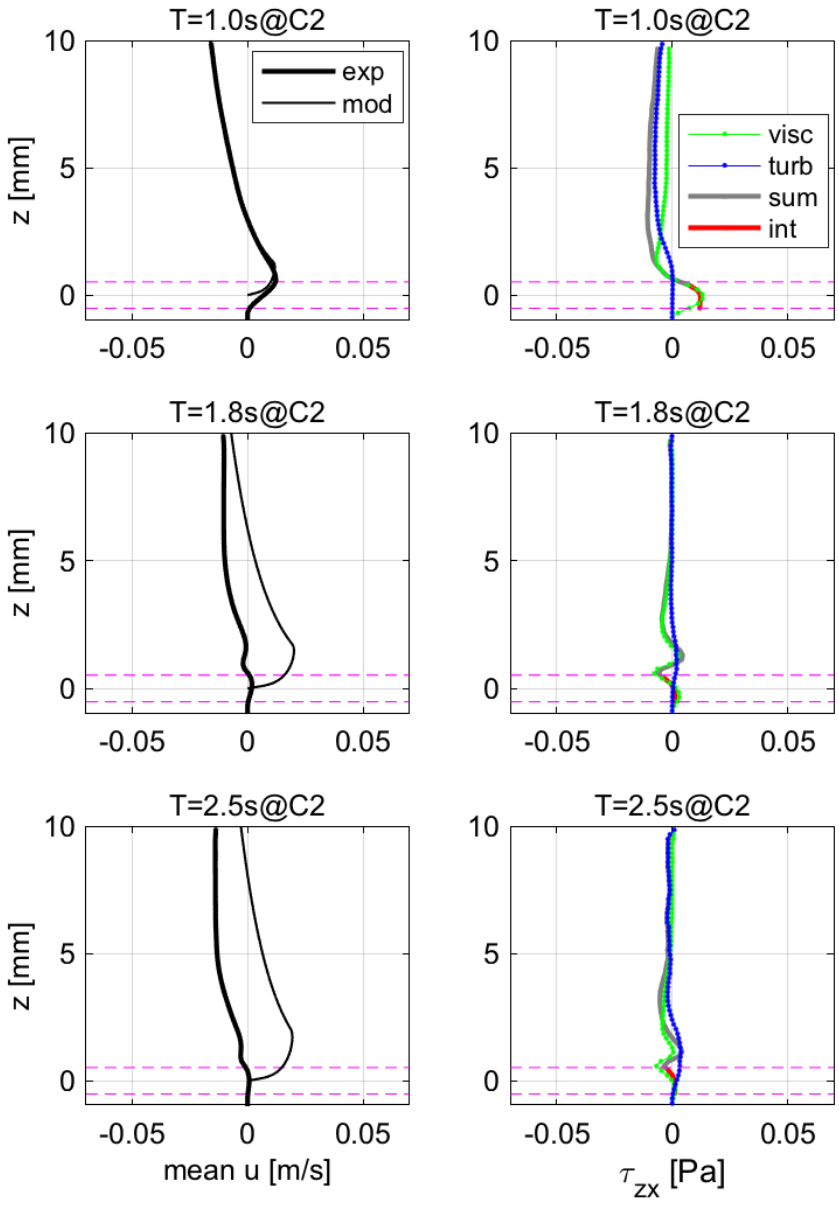

Figure 4.2: Vertical profiles at C2. Left panels, vertical profiles of the time-averaged horizontal velocity of measurements (thick line) and model (thin line). Right panels, viscous shear stress (green), turbulent shear stress (blue), sum of the shear stresses (gray) and Equation 4.4 (red). The horizontal dashed lines mark the crest and trough level of the interfacial sublayer.

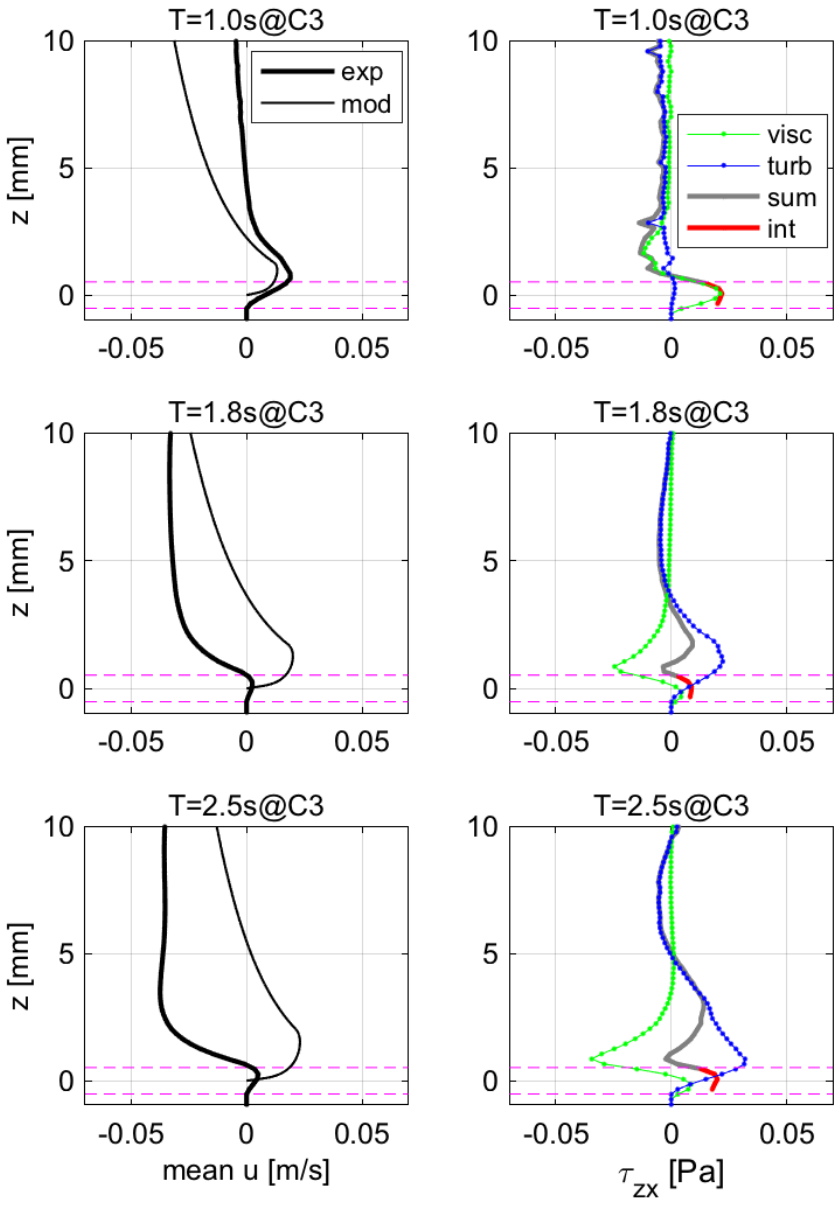

Figure 4.3: Vertical profiles at C3. Left panels, vertical profiles of the time-averaged horizontal velocity of measurements (thick line) and model (thin line). Right panels, viscous shear stress (green), turbulent shear stress (blue), sum of the shear stresses (gray) and Equation 4.4 (red). The horizontal dashed lines mark the crest and trough level of the interfacial sublayer.

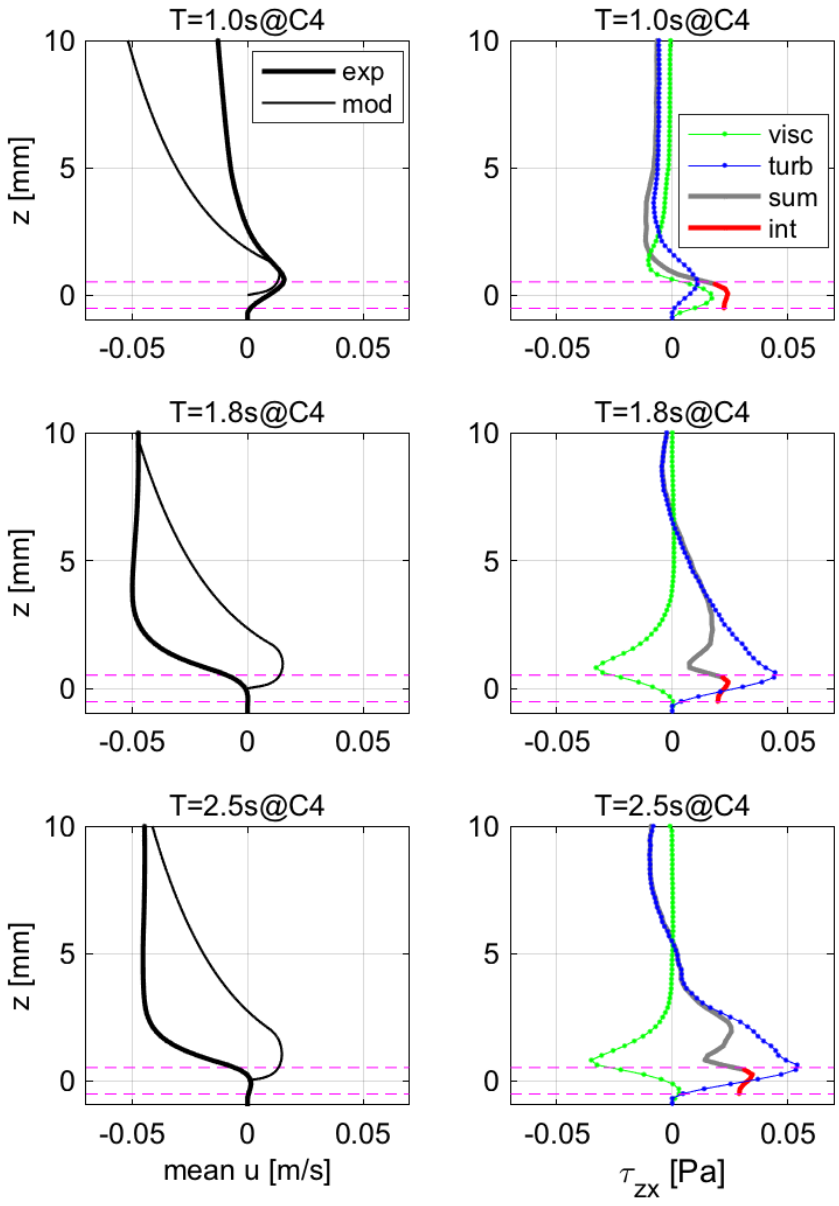

Figure 4.4: Vertical profiles at C4. Left panels, vertical profiles of the time-averaged horizontal velocity of measurements (thick line) and model (thin line). Right panels, viscous shear stress (green), turbulent shear stress (blue), sum of the shear stresses (gray) and Equation 4.4 (red). The horizontal dashed lines mark the crest and trough level of the interfacial sublayer.

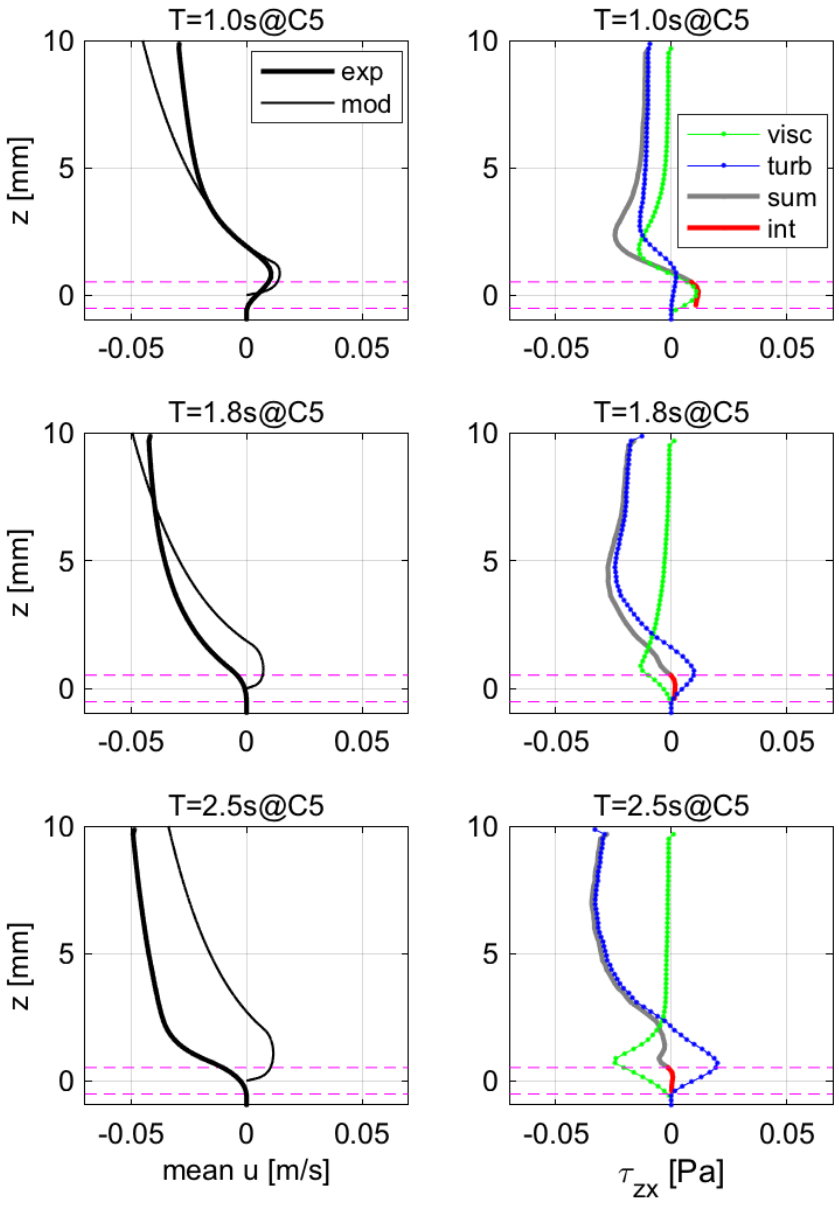

Figure 4.5: Vertical profiles at C5. Left panels, vertical profiles of the time-averaged horizontal velocity of measurements (thick line) and model (thin line). Right panels, viscous shear stress (green), turbulent shear stress (blue), sum of the shear stresses (gray) and Equation 4.4 (red). The horizontal dashed lines mark the crest and trough level of the interfacial sublayer.

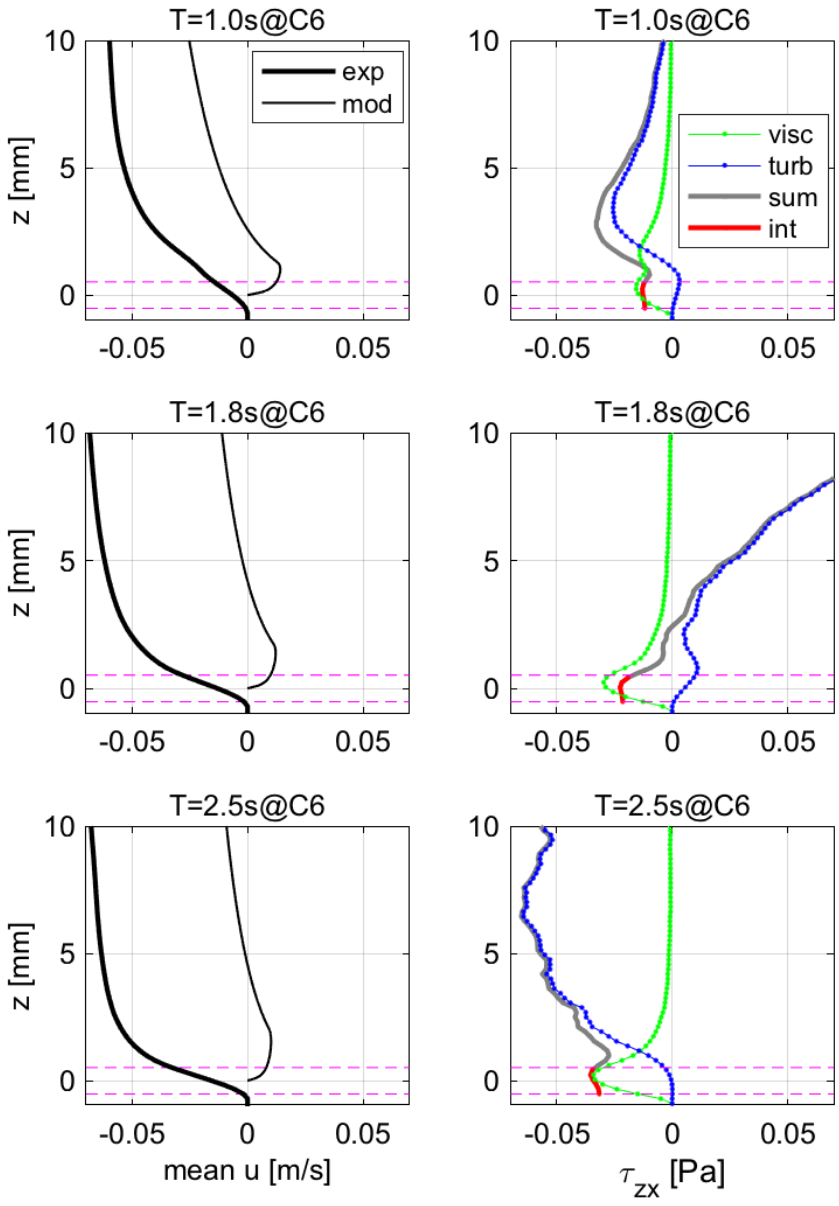

Figure 4.6: Vertical profiles at C6. Left panels, vertical profiles of the time-averaged horizontal velocity of measurements (thick line) and model (thin line). Right panels, viscous shear stress (green), turbulent shear stress (blue), sum of the shear stresses (gray) and Equation 4.4 (red). The horizontal dashed lines mark the crest and trough level of the interfacial sublayer.

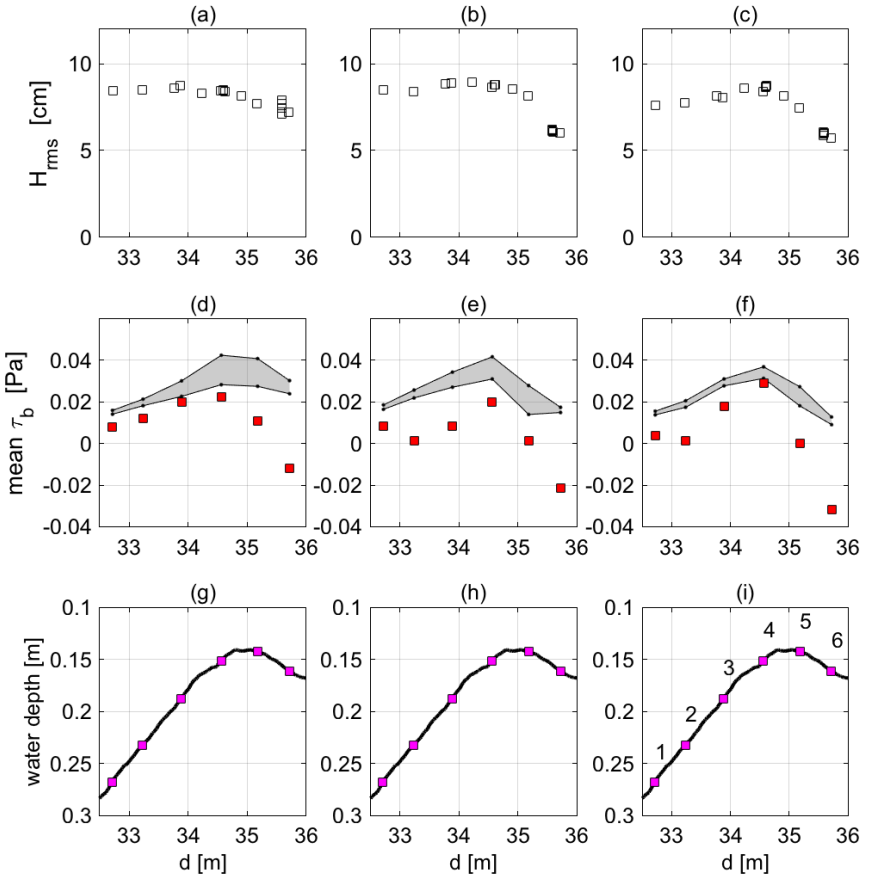

Figure 4.7: (a, b, c) Root-mean-square wave height of tests with periods of 1.0 s, 1.8 s, 2.5 s, respectively. (d, e, f) Time-averaged bed shear stress (squares) of tests with periods of 1.0 s, 1.8 s, 2.5 s, respectively. Upper limit of shaded area corresponds with the wave Reynolds stress using Equation 4.10 and the lower limit is the bed shear stress by the analytic model. The shaded area represents the pressure force. (g, h, i) Similar plots of the fixed bottom profile, squares indicate the locations of the PIV measurements.

same (onshore) direction as the oscillatory contribution $\overline{\widetilde{\tau}_b|\widetilde{\tau}_b|^{0.5}}$. On the contrary, in the bar trough the mean contribution $\frac{3}{2}\overline{\tau}_b\overline{|\widetilde{\tau}_b|^{0.5}}$ was in the offshore direction.

4.6. Discussion

4.6.1. On results

In the following we explore a process that may explain the differences between the measurements and the model results of the velocity profiles. In the absence of wave breaking and in the laminar flow regime, two processes govern the time-averaged bed shear stress: the wave Reynolds stress and the Stokes drift. In a closed flume, the Stokes drift will generate a return flow that is driven by a horizontal surface gradient. Therefore, in terms of a force balance, the expected bed shear stress is equal to the wave Reynolds stress minus the pressure force by the water level gradient. Tests with periods of 1 s had wbbl's that were in the laminar flow regime and, with the exception of C6, had positive time-averaged bed shear stresses (Figure 4.1-4.6). This indicates that the wave Reynolds stresses were larger than the horizontal pressure gradients due to Stokes drift. It is therefore no surprise that the velocity profiles corresponded with a positive wave streaming profile. Since the model includes the physical processes such as the wave Reynolds stress and the Stokes drift it produced similar velocity profiles as in the measurements.

For tests with periods of 1.8 s and 2.5 s the time-averaged turbulent stresses in the wbbl were of similar order of magnitude as the time-averaged viscous stresses. The time-averaged turbulent stresses were nonzero because the time-varying turbulent stresses were not symmetrical over time. The main reason for this was twofold; first, the oscillatory velocity was skewed and asymmetric due to non-sinusoidal waves, second, in turbulent flow the quadratic friction law applies. In the experiment, the time-varying bed shear stresses were often dominated by viscous shear stresses. However, the time-averaged turbulent stresses at crest level of the bottom roughness elements were relatively large for some tests, for example, for T=1.8s@C4 the time-averaged turbulent stress at crest level was 0.045 Pa, which is of similar order of magnitude as the wave Reynolds stress $\tau_{zx,WRS} = \overline{D}_f c^{-1} = 0.039\ Pa$ (using Equation 4.10 and 4.11). The effect of the turbulent stresses become apparent when we consider the horizontal momentum balance in the wbbl (for derivation see Kranenburg et al., 2012, Appendix B);

$$\underbrace{\rho\left(\nu+\bar{\nu}_t\right)\frac{\partial\overline{u}}{\partial z}+\rho\overline{\widetilde{\nu}_t\frac{\partial\widetilde{u}}{\partial z}}}_{\overline{\tau}_b}=\underbrace{\rho\left(\overline{uw}-\overline{uw}_\infty\right)}_{\overline{\tau}_{b,WRS}}+\underbrace{\frac{\partial\overline{p}}{\partial x}\left(z-h\right)}_{F_x} \tag{4.17}$$

On the left-hand-side of Equation 4.17, the first term represents the shear stress associated with the time-averaged velocity gradient $\frac{\partial\overline{u}}{\partial z}$ and the second term represents the wave-related mean shear stress. On the right-hand-side, the first term represents the wave Reynolds stress and the second term is the force associated with the water level gradient F_x.

Note that the left-hand-side of Equation 4.17 represents the time-averaged bed shear stress. Thus, when the wave-related mean shear stress is larger than the sum

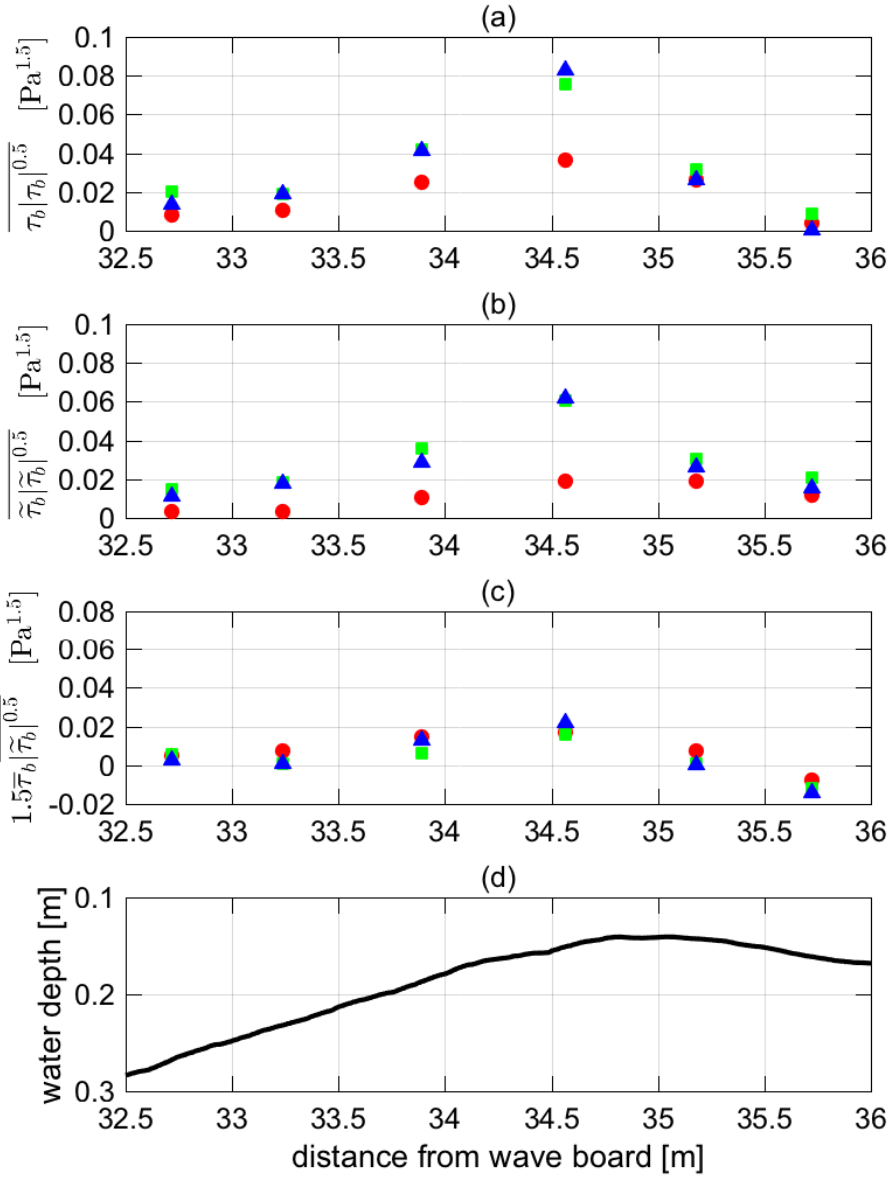

Figure 4.8: (a) The odd bed shear stress moment. Circles, squares, triangles correspond to tests with 1.0 s, 1.8 s, 2.5 s, respectively. (b) The oscillatory contribution to the odd bed shear stress moment. (c) The mean contribution to the odd bed shear stress moment. (d) Bottom profile.

of terms of the right-hand-side, i.e. the wave Reynolds stress and pressure gradient force together, the shear stress associated with the time-averaged velocity gradient will become negative and consequently a negative streaming profile will be observed as in e.g., T=1.8s@C4. In the model, the wave-related mean shear stress was not included and may explain the difference between the measurements and the model results.

The model results indicate that at the offshore location C1 and onshore location C6, the time-averaged bed shear stress was approximately equal to the wave Reynolds stress indicating that the setup caused by Stokes drift was negligible. However, near the bar crest, the (negative) pressure force due to setup was approximately half of the wave Reynolds stress.

From the bar crest to the bar trough there was a clear decreases in the measured time-averaged bed shear stress with negative values at C6. The negative values were likely caused by wave energy dissipation due to wave breaking. Namely, wave breaking is accompanied by additional mass flux and surface stresses that generate setup and drives undertow (Reniers et al., 2004a). The effect of wave energy dissipation was not included in the applied model and thus the model does not show the rapid decrease and no negative values.

Additional difference between model output and measurements may partly be explained by the method used to derive bed shear stresses from the velocity measurements. The method involves spline interpolation over the interfacial sublayer and thus will underestimate viscous stresses over the interfacial sublayer when there would be strong curvature of the velocity profile. This can only be adequately resolved by measuring the velocity in the interfacial sublayer with sufficient spatial resolution. Note that we discarded the flow measurement below the crest level of the roughness elements due to insufficient spatial resolution. The interpolation problem will disappear when the time-averaged turbulent stresses become dominant over the viscous stresses. Thus, bed shear stress estimates of tests with periods of 1 s, T=1.8s@C2, T=2.5s@C2 and T=1.8s@C2 may be affected by the underrepresentation of viscous stresses in the interfacial sublayer.

4.6.2. On past model usage

Ruessink et al. (2007b), Walstra et al. (2012) and Dubarbier et al. (2015) modeled nearshore sediment transport using the Roelvink and Reniers (1994) model, which is similar to the model herein. Ruessink et al. (2007b) and Walstra et al. (2012) used the time-averaged horizontal velocity at 1 cm above the bed to estimate the contribution of the mean flow to the bed shear stress while Dubarbier et al. (2015) used the integrated velocity over the wbbl. It is questionable whether the modeled wbbl current is a representative proxy for the bed shear stress. For instance, in the model it may occur that the wbbl flow is zero or negative while the time-averaged bed shear stress is positive, especially when there is a relatively small surface stress present due to a roller. In addition, the net bedload predicted using the net power (or net bed shear stress) expended by the oscillatory flow is over predicted since this excess of power drives wave shape streaming in the wbbl, a process not included in the model of Roelvink and Reniers (1994).

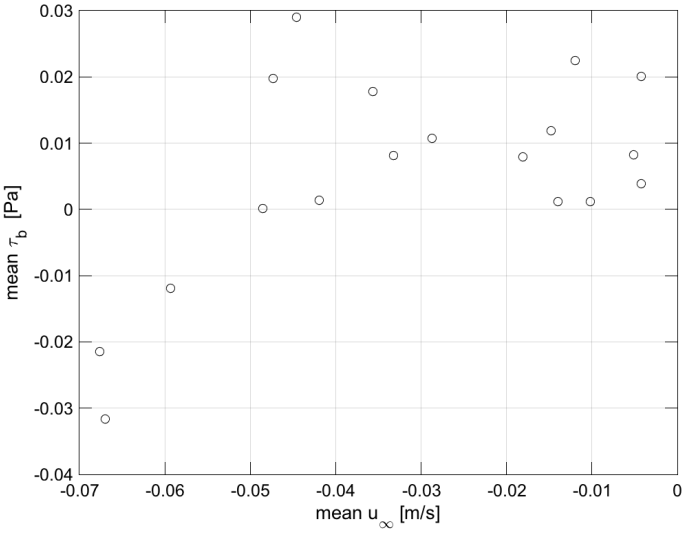

Figure 4.9: The mean bottom shear stresses versus the free-stream currents of the experiment.

An alternative method for predicting bedload, which may be physically more correct, can be achieved by adding the time-averaged bed shear stress attained from the model output and add that to the oscillatory bed shear stress. Essentially, first a translation is required from velocities to bed shear stresses and than from bed shear stresses to bedload. This intermediate step can easily be applied to Shields based transport formulas.

Furthermore, the near-bed suspended sediment transport is not correctly predicted because turbulent stresses under skewed or asymmetric waves, a process not included in the model, will contribute to substantial offshore currents in the wbbl (see also Kranenburg et al., 2012). To resolve the correct time-averaged horizontal velocity profile, a parameterization of the process of wave shape streaming is required in the model. This could be done in a similar fashion as the wave Reynolds stress where, in the case of time-averaged turbulent wave stresses, the shear stress is zero at the top of the wave boundary and maximum at the bed. Here, the time-averaged shear stress by the oscillatory flow can be attained based on the quadratic friction law as described in Chapter 3.

During the experiment, the time-averaged horizontal velocities above the wbbl were all directed offshore while the time-averaged bed shear stresses were directed onshore with the exception of location C6 (see Figure 4.9. This renders the mean free-stream velocity as an unsuitable proxy for the time-averaged bed shear stress and may partly explain the poor predictive capability of conventional energetic type sediment formulations during the onshore sandbar migration observed near Duck, NC (22-27 September 1994) (Dubarbier et al., 2015; Fernández-Mora et al., 2015; Gallagher et al., 1998; Hoefel and Elgar, 2003; Hsu et al., 2006)

4.7. Conclusions

Laboratory wave flume measurements were conducted to study the bed shear stresses by progressive surface waves traveling over a single bar profile. In this chapter the focus was on the time-averaged bed shear stresses, the wave Reynolds stress and the Stokes drift. Under the skewed or asymmetric waves that traveled over the bar crest, the time-averaged bed shear stress was approximately half of the wave Reynolds stress due to the return flow generated by Stokes drift. The free-stream time-averaged velocity above the wbbl was not a good proxy for the time-averaged bed shear stress in the absence of significant wave breaking. The odd 1.5th bed shear stress moment, $\overline{\tau_b|\tau_b|^{0.5}}$, was investigated since bedload is closely related to the power 1.5 of the bed shear stress. The time-averaged bed shear stress contributed approximately 20% of the odd 1.5th bed shear stress moment, $\overline{\tau_b|\tau_b|^{0.5}}$, under skewed or asymmetric waves at the bar crest. The analytic current profile model of Roelvink and Reniers (1994) adequately predicts the contribution of wave Reynolds stress and Stokes drift to the time-averaged bed shear stress. However, the model was not capable of predicting the correct vertical profile of the horizontal velocity in the turbulent wave bottom boundary layer because the process of wave shape streaming was not included in the model.

5

Synthesis

5.1. Introduction

This chapter draws together the contribution of this research on the topic of onshore sandbar migration. First, the results of this research will be discussed in light of the previous state of knowledge as summarized in the introduction chapter of this thesis. The topic of onshore sandbar migration is divided into several sub topics which correspond to different processes in space and time (i.e. periodic and time-averaged). Figure 5.1 provides a schematic overview of the sub topics in the water column with respect to space and time. In addition to the sub topics, the Duck94 onshore sandbar migration event is discussed. After the discussion the findings are applied to the onshore sandbar migration event of the LIP11d Test 1c to identify (new) knowledge gaps for further research that may impact modeling of onshore bar migration. Finally, this chapter ends with the conclusions and recommendations.

5.2. Discussion

5.2.1. The wave front

The steep wave front of a nearly breaking wave has often been associated with onshore sandbar migration. (Madsen, 1974) was the first to investigate this concept inspired by the observations of a military diver: "Just prior to the passage of the crest of a near-breaking wave the bed seemed to explode". Since prior to the passage of the wave crest the horizontal velocity by the orbital motion is approximately zero (at the moment of flow reversal from seaward to shoreward) and the water surface is very steep, it was hypothesized that the horizontal pressure gradient may contribute to sediment transport. This concept was further explored in the research of Flores and Sleath (1998a), Drake and Calantoni (2001), Hoefel and Elgar (2003) and Foster et al. (2000). Another process that may explain a suspension event during flow reversal are coherent structures, known as 'vortex tubes', which are generated in the wbbl during flow reversal (Carstensen et al., 2010; Foster et al., 1994).

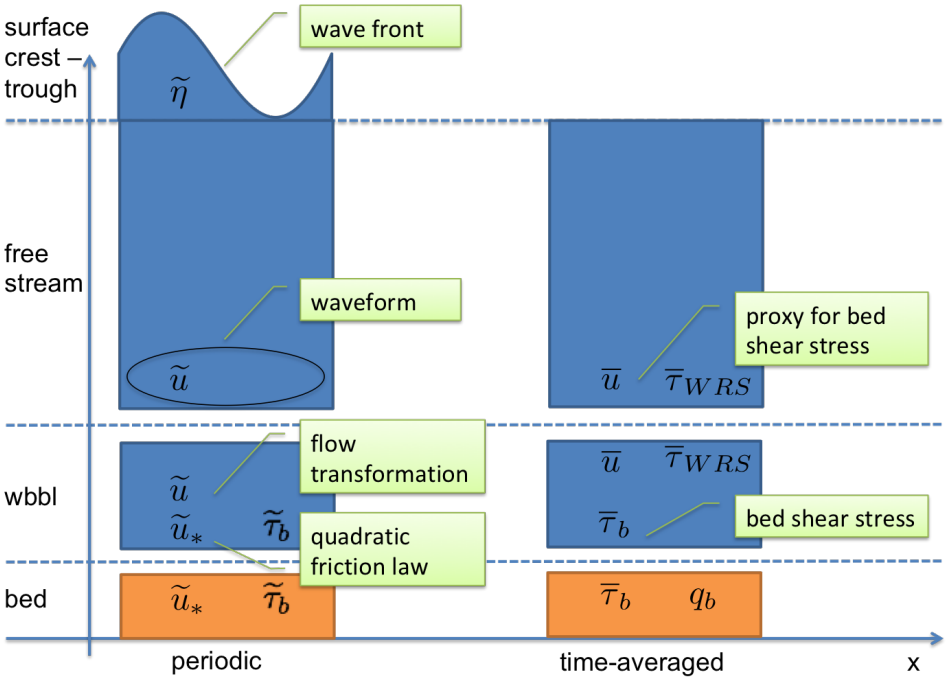

Figure 5.1: Overview of the research topics (denoted by the green boxes) in relation to the water column and physical parameters.

In this study the bed was fixed and the horizontal pressure gradient was not measured. Therefore, we cannot expand further on the relation between the horizontal pressure gradient and sediment transport. However, vortex tubes where consistently observed in the wbbl under steep wave fronts over the bar crest. In the tests of Carstensen et al. (2010) vortex tubes did not occur for Reynolds numbers larger than $RE = 3 \times 10^5$ which coincided with the transition from laminar to turbulent flow in the wbbl. In our tests the wave Reynolds numbers were not larger than $RE \leq 3.2 \times 10^4$. This raises the question whether vortex tubes occur in the field, for example, during the Duck94 onshore sandbar migration where the wave Reynolds number was $RE = 6 \times 10^5$ (Berni et al., 2013a). Unfortunately, there is currently no data available to investigate this.

5.2.2. The waveform

For research relating to nonlinear surface waves it is necessary to have a unified parameterization for nonlinear waveforms which can be related to real skewed and asymmetric waves in the nearshore. The time series of surface waves (or horizontal orbital velocity) is characterized by the bispectral parameters: 1) skewness, 2) asymmetry, 3) energy and 4) peak frequency. A representative time series of a single surface wave can be constructed from these four parameters using the waveform description developed by Abreu et al. (2010)(their work is based on the work of (see Drake and Calantoni, 2001; Terrile et al., 2009b)). The waveform description is based on an amplitude and phase relation between the harmonics which was not yet validated against real surface wave data.

From the data of this study it is evident that the waveform description is a good approximation for the shape of the regular waves encountered over the bar in the experiment, which spanned a broad range of skewness and asymmetry. Differences were mainly found for waves after the bar crest where there was a mismatch in harmonic amplitudes which may be caused by wave breaking processes. Thus, the waveform description allows for the application of a nonlinear horizontal orbital velocity at the surface or the upper boundary of the wbbl.

5.2.3. The transformation of the orbital velocity in the wbbl

Nielsen (1992, 2002) noted that the shape of the free-stream horizontal velocity (i.e. the signals non-dimensional skewness and asymmetry) is not similar to the shape of the friction velocity at the bed (in case the signal is asymmetric). This process can be explained by considering that the horizontal velocity signal is composed out of harmonic components. In the wbbl, the horizontal velocity components will lead the free stream components with a maximum phase lead at the bottom (see e.g. Batchelor, 1967; Stokes, 1851). By adding a phase lead to the phase of the horizontal velocity components the shape of the compound signal will change. This process is elegantly described by Henderson et al. (2004):

> "Qualitatively, the conversion of asymmetry to skewness results from the frequency-independent shift in phase, which corresponds to a frequency-

> dependent shift in the timing of the Fourier components. The change in the timing of the Fourier components systematically changes the shapes of the velocity fluctuations."

The experiment data of this study, Henriquez et al. (2014, 2011), and Berni et al. (2013a) confirm that the horizontal velocity transformation occurs in the wbbl. The magnitude of the transformation depends on the values of the phase leads and amplitudes (i.e. friction coefficients) of the friction velocity components with respect to the free-stream velocity components. For laminar flow and a smooth bed, the oscillatory boundary layer velocity and bed shear stress are described by the the analytic solution by Stokes (1851). In this study, the conditions of the experiment consisted of dominantly laminar flow over a rough bed. Here, the friction velocity phase leads were approximately 37 degrees instead of the 45 degrees of the analytic solution.

In addition, we conducted and examined numerical model simulations of the oscillatory boundary flow with turbulent flow conditions and a rough bed. Here, the friction velocity phase leads of the first harmonics were around 18 degrees which are a bit lower than the experimental findings of van der A et al. (2011, Figure 6). The higher harmonic phase leads were generally a few degrees lower than the first harmonic and support the suggestion of Henderson et al. (2004) for allowing a constant (friction) velocity phase lead for consecutive harmonics. The frequency dependence of the friction velocity amplitudes was weak, i.e. the amplitude of the second harmonics was about 1.2 times larger than the amplitude of the first harmonics.

In all, free-stream velocity asymmetry leads to friction velocity skewness at the bed which contributes to the net sediment transport over the wave cycle and is therefore a very important process to consider in the sediment transport by waves in the nearshore.

5.2.4. The quadratic friction law

The friction force between the fluid and the bed (i.e. the bed shear stress τ_b) for steady flows is commonly expressed as $\tau_b \sim u^2$ which is based on empirical findings from experiments, e.g. Meyer-Peter and Müller (1948) and Wilson (1987) and the physically-based derivation of Bagnold (1966). In the absence of contrary evidence, the quadratic relation is also applied for bed shear stress estimates by the 'unsteady' orbital wave motion (see e.g. Bailard, 1981, 1982; Bailard and Inman, 1981; Bowen, 1980; Ribberink, 1998; Roelvink and Stive, 1989). Nielsen (2002) noted that the quadratic drag relation is not fully supported by experiment data.

In this study we conducted numerical model simulations of oscillatory flow and concluded that the relation between free-stream velocity and bed shear stress is not quadratic and is closer to $\tau_b \sim u^{1.6}$. However, the impact of this finding is minor on the dimensional skewness of the bed shear stress (approximately 10%). Applying the relatively simple quadratic expression (Equation 3.17) results in a r^2 of 0.91 when compared to the numerical modeling results.

5.2.5. The time-averaged bed shear stress

The cross-shore time-averaged bed shear stress is generally one order of magnitude smaller than the maximum time-varying bed shear stress. Although smaller, the time-averaged bed shear stress can have a large impact on magnitude and direction of the total net bedload (Hsu et al., 2006). The contribution of the time-averaged bed shear stress to the total net bedload becomes apparent when the terms are decomposed using a Taylor expansion (Bowen, 1980):

$$\overline{q}_b \sim \underbrace{\overline{\tau_b|\tau_b|^{0.5}}}_{\substack{\text{odd 1.5th}\\ \text{moment}}} = \underbrace{\overline{\widetilde{\tau}_b|\widetilde{\tau}_b|^{0.5}}}_{\substack{\text{time-varying}\\ \text{part}}} + \underbrace{\frac{3}{2}\overline{\tau}_b\overline{|\widetilde{\tau}_b|^{0.5}}}_{\substack{\text{time-averaged}\\ \text{part}}} + \cdots \tag{5.1}$$

In this study the hydrodynamic conditions which occurred during an onshore bar migration event were mimicked in a wave flume. In addition, an analytic quasi-1DV model of Roelvink and Reniers (1994) was utilized to further explore the effects of the wave Reynolds stress (wave forcing), mass flux and set-up gradients on the time-averaged bed shear stress. Experiment and model data indicate that during the experiment the time-averaged bed shear stress of the tests were directed onshore over the bar crest. Furthermore, the time-averaged bed shear stress, $\overline{|\widetilde{\tau}_b|^{0.5}}$, contributed approximately 20% of the odd 1.5th bed shear stress moment, $\frac{3}{2}\overline{\tau}_b\overline{\tau_b|\tau_b|^{0.5}}$, under skewed or asymmetric waves at the bar crest. These findings emphasizes the importance to include the time-averaged bed shear stress in onshore sandbar migration modeling efforts.

5.2.6. The flow velocity as a proxy

The time-averaged horizontal velocity is often used as a proxy for the time-averaged bed shear stress in morphodynamic (model) studies (e.g. Dubarbier et al., 2015; Fernández-Mora et al., 2015; Gallagher et al., 1998; Hoefel and Elgar, 2003; Hsu et al., 2006; Ruessink et al., 2007b; Walstra et al., 2012). The results of the experiment and modeling efforts herein indicate that the relation between the time-averaged horizontal velocity and bed shear stress is not consistent due to the complex vertical flow structure (see e.g. Figure 4.1-4.6 and Figure 4.9). This is caused by the mixture of processes, among others, mass flux, wave Reynolds stress, wave shape streaming (Kranenburg et al., 2012) and roller surface stress. This may partly explain the poor predictive capability of conventional energetic type sediment formulations during the onshore sandbar migration observed near Duck, NC (22-27 September 1994) (Dubarbier et al., 2015; Fernández-Mora et al., 2015; Gallagher et al., 1998; Hoefel and Elgar, 2003; Hsu et al., 2006). Therefore, it is recommended to obtain an estimate of the time-averaged bed shear stress from the force balance of a process-based (analytic) model (e.g. Reniers et al., 2004a).

It must be noted that the current version of the process-based analytic model of Reniers et al. (2004a) does not include the process of wave shape streaming. However, this process may be parameterized and incorporated in the model.

5.2.7. The Duck94 onshore sandbar migration

In this section we review the sediment transport pattern during the onshore sandbar migration event of the Duck94 field experiment since this event has been used in many studies to test hypothesis and rate the performance of morphological models (see Table 1.1). The studies of Hoefel and Elgar (2003) and Henderson et al. (2004), Hsu et al. (2006) focus on processes that generate a maximum sediment transport over the bar crest. Hence the question: what was the actual sediment transport pattern during the onshore bar migration event?

A sediment transport pattern with a maximum over the bar crest is motivated by the erosion and accretion that may occur during an onshore sandbar migration. Namely, when the bar migrates shoreward, the bar needs to erode on the seaward side and accrete on the shoreward side. In general, erosion happens when the sediment transport gradient is positive, and accretion when sediment transport gradient is negative. Two things can be deducted from the associated erosion and deposition pattern. First, the unbroken waves need to generate net transport, which means that more sand is transported during the shoreward movement of the orbital motion than during the seaward movement of the orbital motion or vice verse. Secondly, to comply with the associated erosion and deposition pattern, the net transport needs to have a local maximum close to the bar crest (see also Walstra et al., 2012).

The onshore sandbar migration event occurred between 22 and 27 September 1994 during an extensive field campaign and was well registered. For this analysis, the sediment transport is derived from the bed level observations. Figure 5.2 and 5.3 shows the sediment transport during two specific tidal cycles (corresponding with tide event B and E in Figure C.3). Note that here a tidal cycle is defined by the high water and the preceding low water.

The intra-tide sediment transport shows the following pattern:

1. Accretion on the shoreward side of the bar occurred during the low waters of September 23 13:00 and September 26 16:00 while the sediment transport was directed offshore.

2. Erosion on the seaward side of the bar occurred during the high waters of September 23 19:00 and September 26 22:00 while the sediment transport was directed onshore.

3. the combination of the sediment transports during low and high water result in the typical sediment transport pattern where the maximum is over the bar crest.

Therefore, we can conclude that the intra-tide sediment transport pattern did not correspond with the typical sediment transport pattern and, the tide-averaged sediment transport did correspond with the typical sediment transport.

5.3. Application - The LIP11d Test 1c

5.3.1. Introduction

In this section the findings are applied to a real-scale onshore bar migration event to evaluate the current status of knowledge and identify (new) knowledge gaps. For

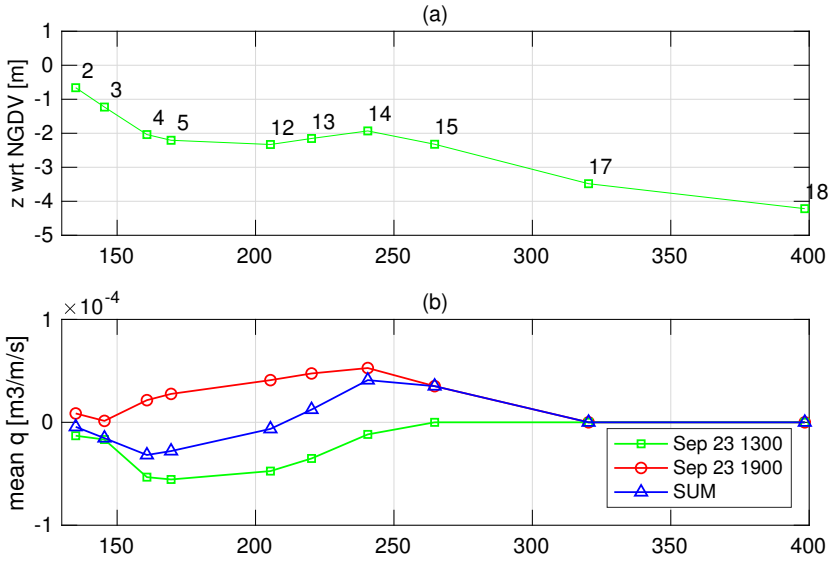

Figure 5.2: Sediment transport during Duck94 on 23 September 13:00 (low water) and 19:00 (high water)

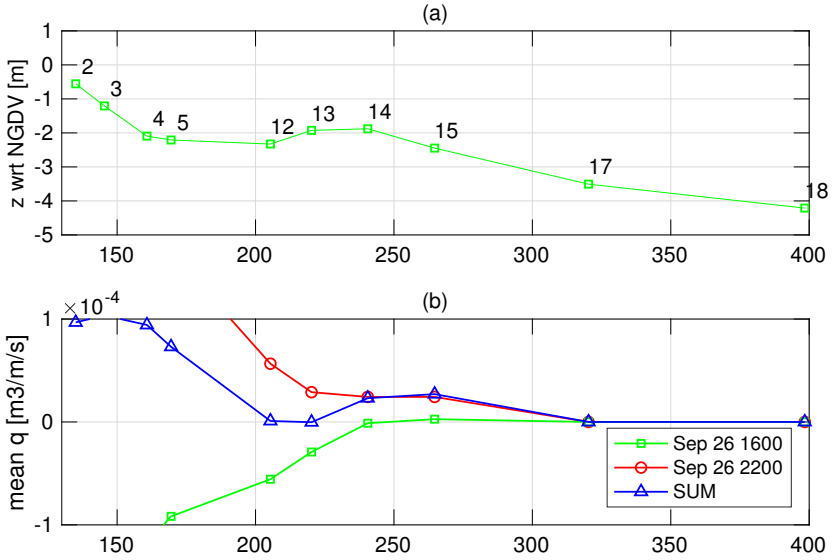

Figure 5.3: Sediment transport during Duck94 on 26 September 16:00 (low water) and 22:00 (high water)

this we use the observation of the LIP11d Test 1c which was part of a large-scale wave flume experiment (Roelvink and Reniers, 1995). The findings of this study are incorporated into a model structure.

5.3.2. Description of flume test

The experiments took place in the Delta flume of DELFT HYDRAULICS in the Netherlands in April-June 1993. The flume had a length of 223 m, a width of 5 m, a depth of 7 m and was equipped with a piston-type wave maker. The water level in the flume was 4.1 m. The bed material consisted of sand with a median grain diameter of 220 µm. The bottom profile at the start of Test 1c was the result of previous tests that resulted in a single bar profile. The wave conditions were based on a narrow-banded spectrum with a significant wave height of 0.6 m and a peak period of 8 s. Contrary to the erosive wave conditions of the previous tests, the wave conditions of Test 1c were considered strongly accretive due to a lower significant wave height in combination with a larger peak period.

Ten pressure sensors were installed along the wave flume at fixed locations. A vertical array of 5 electro-magnetic flow meters (emf) was attached to a carriage. The bottom profiles were measured with an echosounder in combination with a wheel-based profile follower.

Test 1c consisted of 13 consecutive wave hours. Usually, after one wave hour the carriage was re-positioned at a different location. The distance between the carriage and a pressure sensor was never more than 5 m. Bottom profiles were measured after 1 to 3 wave hours.

The sediment transport was obtained from the bed-level changes between the profiles measured after 2 wave hours (code 1C02) and 7 wave hours (code 1C07) (Figure 5.6d). Integrating the bed-level changes from the dry beach towards the wave maker led to the total sediment transport (Figure 5.6c).

5.3.3. Model structure

The essence of the model structure shown in Figure 5.4 is to estimate the temporal bed shear stress which constitutes of the time-varying and time-averaged part. For the time-varying part, the bed shear stresses are estimated by parameterizing the orbital free-stream flow velocity near the bed with a waveform and transforming the waveform in the wbbl. Hereafter, the transformed waveform is converted into a bed shear stress using the quadratic friction law:

$$\tau_b(t) = \frac{1}{2}\rho f_w |u_b| u_b \quad ; \quad u_b(t) = \Re\{u_\infty e^{i\varphi}\} \tag{5.2}$$

In this application the flow velocity measured by the lowest electro-magnetic flow meters (emf) was used (approximately 10 cm above the bed). It must be noted that when a skewed waveform is raised to the power of 2 a time-averaged component is generated:

$$\tau_b(t) = \overline{\tau}_{b,\text{wave shape}} + \widetilde{\tau}_b \quad , \tag{5.3}$$

The time-averaged bed shear stress component has the subscript 'wave shape' to link to the process of 'wave shape streaming' (Kranenburg et al., 2012) and basically

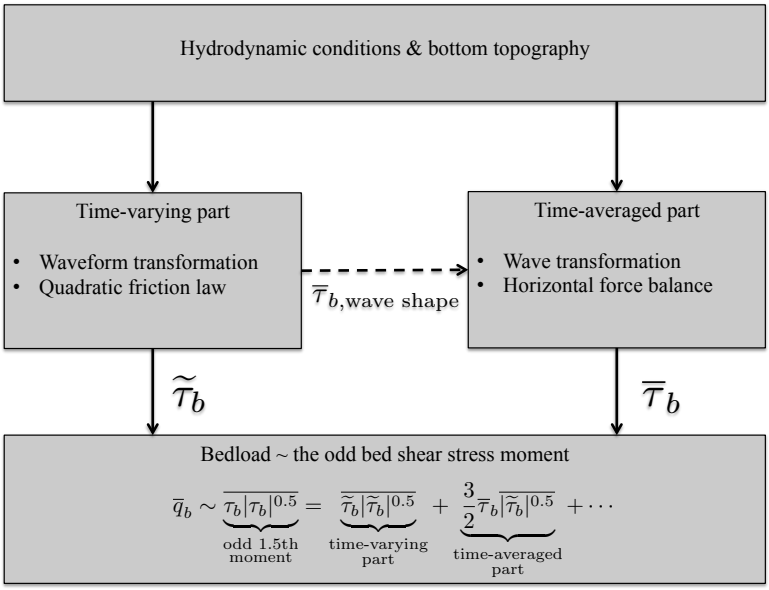

Figure 5.4: Schematic overview of modeling approach to estimate bedload. In the current two-way approach the time-varying and time-averaged bed shear stress were determined independently. The bed shear stresses are combined to determine the odd 1.5th moment which consists of a time-varying and time-averaged part. See Section 4.2 for background on the terms of the odd 1.5th moment.

needs to be included in the time-averaged horizontal momentum balance. However, this has not yet been accomplished, hence the dashed line in Figure 5.4.

The time-averaged part of the bed shear stress was estimated by solving the horizontal force balance. For this application the analytic model of (Reniers et al., 2004a) was used which was driven by the measured data. The wave dissipation was set as a free variable in the model and was found by minimizing the difference between model results and observations. For reference, the resulting wave dissipation was compared to the wave dissipation from the wave transformation model of (Reniers et al., 1997).

5.3.4. Results and discussion

The analytic model was capable of reproducing the observed vertical flow profiles (see Figure 5.5).

The transformation of the orbital flow velocity in the wbbl only had an impact on the measurement location that was inshore of the bar ($X = 138$ m in Figure 5.6a). Here, the third moment of the orbital velocity was larger due to the transformation of velocity asymmetry to velocity skewness. Thus, this transformation promotes onshore bar migration, however, since the maximum was located inshore of the bar crest it also promoted bar damping (Walstra et al., 2012).

In contrast to the third moment of the orbital velocity, the maximum of the odd 1.5th bed shear stress moment was located offshore of the bar crest ($X = 134$ m in Figure 5.6b). This promoted onshore bar migration and bar growth. Thus, the location of the odd 1.5th bed shear stress moment was also determined by the time-averaged bed shear stress.

The wave dissipation is commonly modeled through a roller which contains and dissipates energy, and hence provides a surface stress. From the observed vertical flow profiles the roller dissipation (D_r) was estimated with the analytic model of (Reniers et al., 2004a). The roller dissipation increased rapidly inshore of $X = 140$ m (Figure 5.7c) which is in agreement with the fraction of observed rollers (Figure 5.7b). Apparently, the rollers started dissipating their energy in the bar trough.

The wave transformation model of (Reniers et al., 1997) provided wave energy estimates that were in agreement with the observations (Figure 5.7a). However, the wave transformation model predicted a large peak in the fraction of rollers and roller energy dissipation at the bar crest ($X = 135$ m). This peak was not observed in the observations and the analytic model (see Figure 5.7b and 5.7c). This mismatch was also illustrated in the study of Boers (2005).

It must be noted that many onshore sandbar migration studies utilize the above-mentioned wave transformation model (e.g., Dubarbier et al., 2015; Fernández-Mora et al., 2015; Ruessink et al., 2007a). Consequently, the roller dissipation will dramatically affect the horizontal force balance since this is the most dominant force in the nearshore. For example, during the LIP11d Test 1c, the time-averaged surface stress in the bar trough was one order of magnitude larger than the wave Reynolds stress.

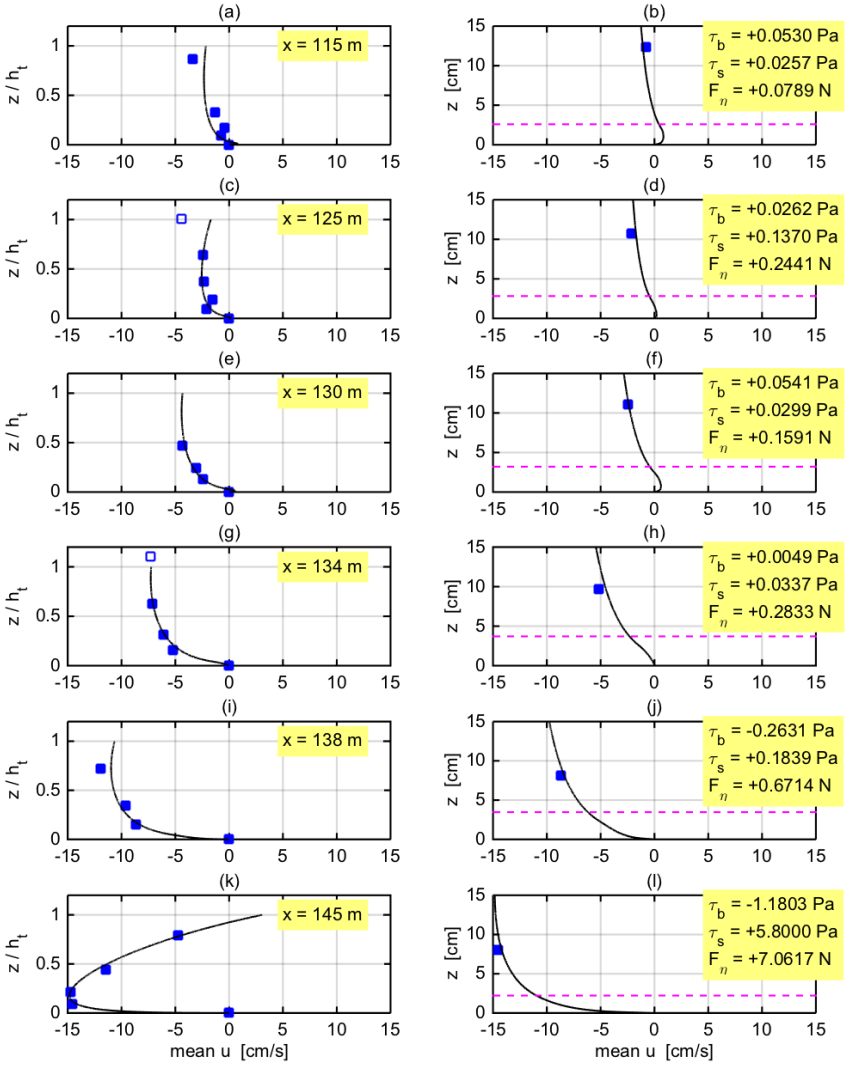

Figure 5.5: Vertical flow structure of the time-averaged horizontal velocity during the LIP11D Test 1c. Solid lines are the RTSR04 model. The blue square markers are the measurements with the exception of the marker at the bottom which is set to zero. The panels from top to bottom represent different locations along the flume. The panels in the left column (a, c, e, g, i, k) show the velocity profile over the entire (normalized) depth and the panels in the right column (b, d, f, h, j, l) show the velocity profile over the lower 15 cm. The symbol τ_s is the modeled wave breaking related shear stress at through level and $F_\eta = \rho g h \frac{\partial \overline{h}}{\partial x}$.

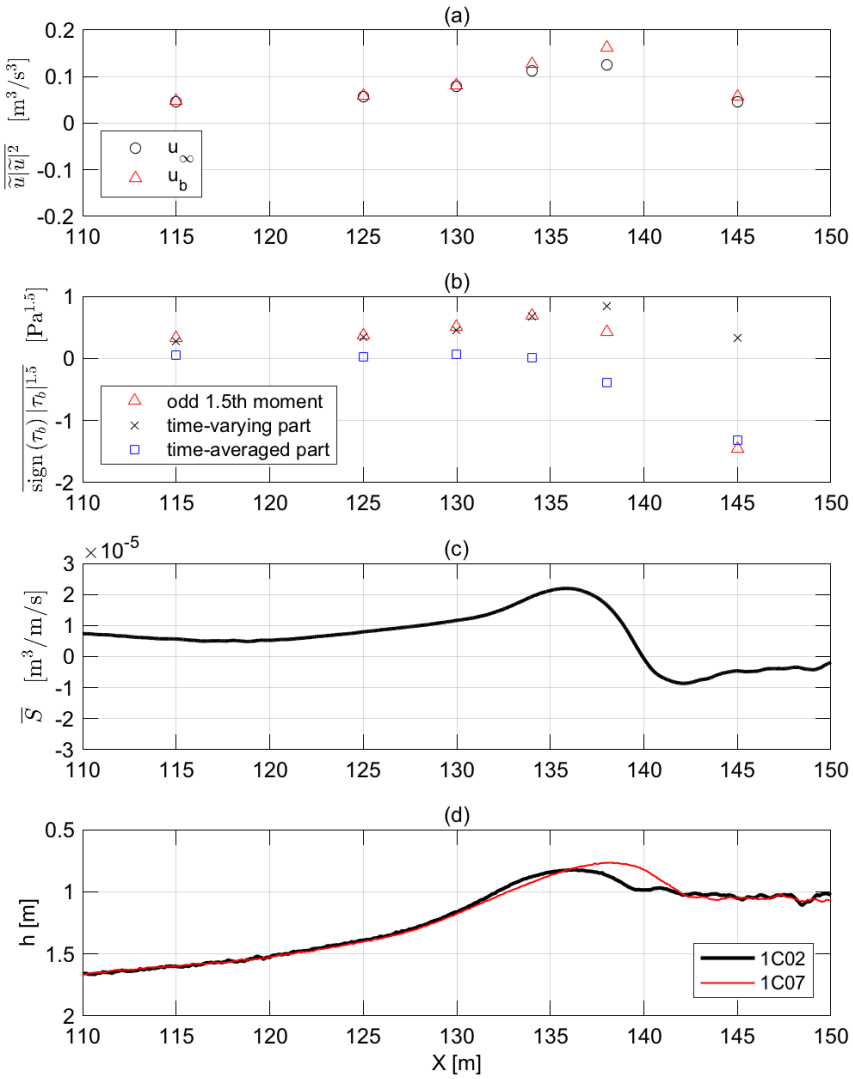

Figure 5.6: Moments of the velocity and bed shear stress of the LIP11d Test 1c. (a) Third moment of the orbital velocity u_∞ of the lowest measurement point and u_b (Equation 5.2 with $\varphi = 20°$). (b) The odd 1.5th moment including the time-varying and time-averaged part. (c) Sediment transport derived from from profile 1C02 and 1C07. (d) Measured bottom profiles during the LIP11d Test 1c.

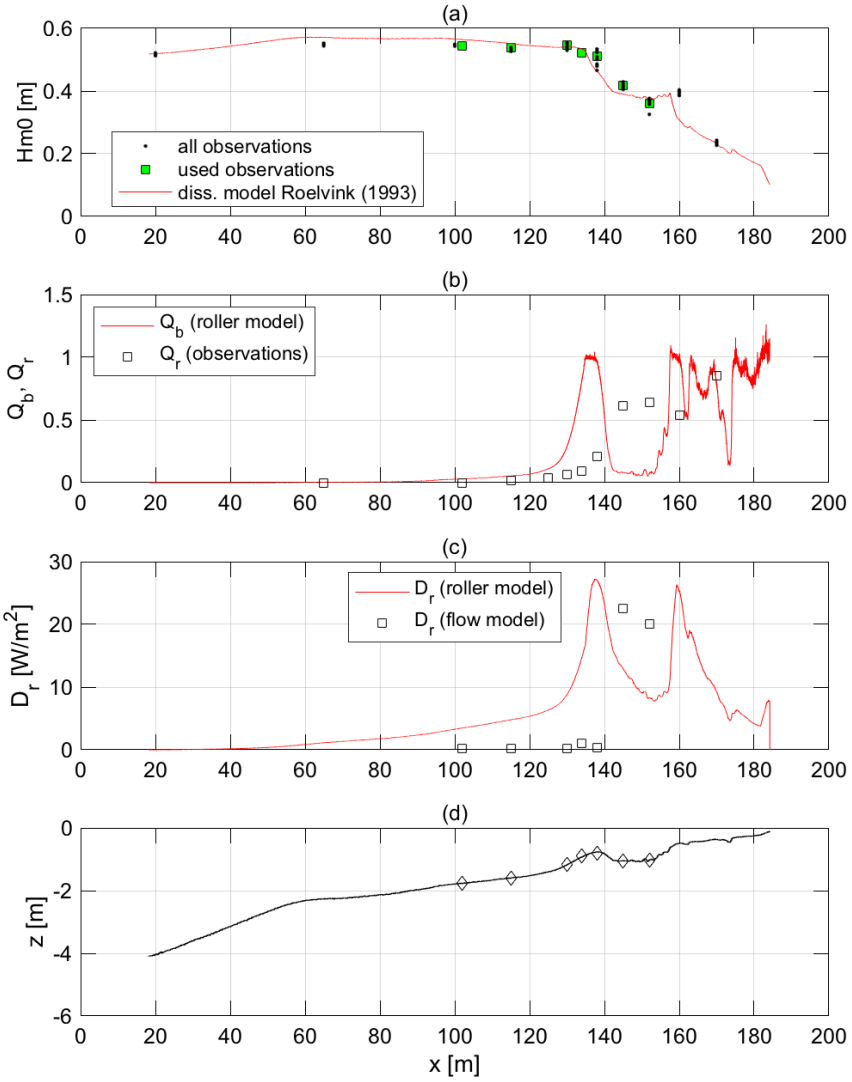

Figure 5.7: Wave heights, fraction of breaking waves and wave energy dissipation of the of the LIP11d Test 1c. (a) Wave heights along the wave flume. The markers are measurements. The red line is the wave dissipation model of Roelvink (1995). (b) Fraction of breaking waves. Markers are observations and the red line is the model of Battjes and Janssen (1978). (c) The roller dissipation determined with Stive and De Vriend (1994) (red line) and by inverse modeling with the analytic model of (Reniers et al., 2004a) (markers). (d) Bottom profile of the LIP11D Test 1c. Markers indicate the locations of the measurements.

6

Conclusions and recommendations

6.1. Conclusions

What is the relation between the bed shear stress and the nonlinear orbital wave motion?

In order to observe this relation an experiment was conducted in a medium-sized wave flume with a rigid single bar profile. The shape of the profile was based on a measured profile which occurred during an onshore bar migration event with a mobile-bed in the same wave flume. The wave shapes were skewed and asymmetric (i.e. nonlinear wave shape) when the waves were traveling over the bar crest. The flow velocities in the wbbl were measured with the PIV technique at six locations along the wave flume. The camera produced images which covered an area of approximately 12 mm by 12 mm with sub-millimeter resolution. Therefore, detailed flow velocities were obtained of the wbbl. The velocity vectors were decomposed in a tangent and normal component on the basis of the local bottom slope at each of the measurement locations.

In some tests vortex tubes were generated in the wbbl during flow reversal of the orbital motion. Due to the rigid bed in combination with regular waves, the vortex tubes were generated at fixed locations and wave phases. The wave length of the vortex tubes where approximately equal to the camera image width. To eliminate the velocity variations over the horizontal space (along the wave flume) caused by the vortex tubes, the flow velocity vector fields were spatially averaged over the horizontal space.

Viscous and turbulent fluid shear stresses were derived from the flow velocity vectors above the bottom roughness elements. However, these stresses are not yet the stresses between the bottom and the fluid. Since the bottom was not smooth the interface between the bottom and the fluid is defined by a layer between the crests and troughs of the roughness elements, i.e. the interfacial sublayer. For the

conservation of momentum it is necessary to consider the amount of horizontal space occupied by fluid relative to the space occupied by the bed which was accounted for by using a roughness geometry function.

The observations of the wbbl showed that in laminar flow the relation between the free-stream velocity and the friction velocity components was linear. The friction velocity amplitudes were frequency dependent and the phase leads were frequency independent. Thus, these observations were inline with the analytic solution for oscillatory laminar flow over a smooth bed. However, the phase leads of the friction velocity components were approximately 37 degrees instead of the theoretical 45 degrees, which may be related to the fact that the bed was not smooth in the experiment.

Modeling results of the wbbl showed that in turbulent flow the relation between the free-stream velocity components and the friction velocity components was nonlinear, approximately $\tau_b \sim u^{1.6}$. Furthermore, the friction velocity amplitudes and the phase leads were frequency independent. Applying the quadratic assumption $\tau_b \sim u^2$ will result in a relatively small error ($\sim 10\%$) in the skewness of the bed shear stress.

The experimental and numerical data confirm that under nonlinear regular waves the free-stream velocity asymmetry leads to bed shear stress skewness. This process can be modeled by summing the solutions of the harmonic components or using the analytic expressions of Abreu et al. (2010) and Malarkey and Davies (2012). Namely, the shape of the surface elevation and horizontal velocity of nonlinear regular waves can adequately be described using two shape parameters, i.e. one parameter for the harmonic amplitudes and one parameter for the harmonic phases as was suggested by Abreu et al. (2010). These parameters can easily be derived from the skewness and asymmetry of the signal.

How large is the time-averaged bottom shear stress due to mass flux, Longuet-Higgins streaming and wave shape streaming?

During the wave flume tests, under the skewed or asymmetric waves that traveled unbroken over the single bar profile, the bed shear stresses were generally directed onshore and approximately equal to half of the wave Reynolds stresses. The maximum time-averaged bed shear stress was located at the bar crest. In general, the free-stream time-averaged velocity above the wbbl was not a good proxy for the time-averaged bed shear stress (at least under unbroken waves) due to the complex flow structure in the wbbl.

Since bedload is related to the power 1.5 of the bed shear stress, the odd 1.5th bed shear stress moments ($\overline{\tau_b|\tau_b|^{0.5}}$) were investigated. In the tests, the time-averaged bed shear stress contributed approximately 20% to the odd 1.5th bed shear stress moment, $\overline{\tau_b|\tau_b|^{0.5}}$, under skewed or asymmetric waves at the bar crest.

The analytic current profile model of Reniers et al. (2004a) estimated the contribution of wave Reynolds stress and Stokes drift to the time-averaged bed shear stress. However, the model was not capable of predicting the correct vertical profiles of the horizontal velocity when the wave bottom boundary layer was turbulent because the process of wave shape streaming was not included in the model.

The research questions were formulated to investigate and better understand onshore sandbar migration. Essentially, onshore bar migration is driven by cross-shore transport gradients where the maximum transport is over the bar crest. When the maximum transport is located seaward (landward) of the bar crest the sandbar grows (dampens). In this research, the free-stream velocity skewness was the main contributor to the odd 1.5th bed shear stress moments ($\overline{\tau_b|\tau_b|^{0.5}}$) which had maximum over the bar crest. The transfer of velocity asymmetry to velocity skewness in the wbbl was relatively large and resulted in the increase of the friction velocity skewness with a factor of 1 to 4. The contribution of the time-averaged stresses were relatively smaller, however, the time-averaged stresses tend to position the maximum of the odd 1.5th bed shear stress moment on the seaward side of the bar crest promoting bar growth. This effect is enhanced by wave breaking and the corresponding dissipation which lead to negative time-averaged bottom shear stresses.

6.2. Recommendations

From this study it appears that the time-averaged processes can have a large impact on the odd 1.5th bed shear stress moment and, therefore, on the bedload. To improve the modeling capabilities of onshore sandbar migration the following topics are recommended for further research:

1. Improve the roller dissipation model. It is vital to accurately model the roller dissipation in the nearshore since the associated time-averaged forces are one order of magnitude larger than the time-averaged bed stresses by the orbital motion.

   There is a mismatch when the roller dissipation is estimated from the flow velocity measurements through inverse modeling and when roller dissipation is estimated from the surface elevation measurements using a roller model. Observation of the roller and advanced numerical flow models may provide insight in roller dissipation processes.

2. Incorporate 'wave shape streaming' in the time-averaged horizontal force balance of a nearshore flow model. In the turbulent wbbl the associated stress of wave shape streaming is of similar order of magnitude as the wave Reynolds stress.

   Using advance numerical flow models 'wave shape streaming' can be parameterized and incorporated in practical nearshore flow models.

3. Extensive observations of nearshore processes over the vertical space for a coherent picture.

   The wave flume experiment in the study herein focused on the wbbl with minimal wave breaking. The LIP11d experiment focused on the middle layer (from wave through to the wbbl) with breaking waves. To investigate the horizontal force balance it is recommended to have accurate observation of all

three layers, the top layer from wave crest to wave through, the middle layer and the wbbl.

A

Nonlinear waveforms

A.1. Skewness and asymmetry

As waves shoal, for instance, when traveling upslope, energy is transferred to the higher harmonics giving the waves first a Stokes/skewed shape and eventually a pitched forward asymmetric shape (Beji and Battjes, 1993; Doering and Bowen, 1995; Elgar and Guza, 1985). Energy transfer between harmonics is continued as waves de-shoal, for instance, when traveling downslope (Beji and Battjes, 1993). The nonlinear interactions can be modeled with sophisticated spectral, Boussinesq, and non-hydrostatic models.

The wave shape can be quantified by the skewness and asymmetry parameter. Lets consider a discretely sampled signal $\zeta(t)$ that can be a wave variable such as the surface elevation or orbital velocity (see for example Figure A.1). The time series $\zeta(t)$ can be represented as

$$\zeta\left(t\right) = \sum_{n=1}^{N} \{A_n \exp\left(i2\pi f_n t\right) + A_n^* \exp\left(-i2\pi f_n t\right)\} \tag{A.1}$$

where f is frequency, A_n are complex Fourier coefficients, the asterisk denotes complex conjugation, subscript n is the frequency index and N is the number of samples Elgar and Guza (1985).

The skewness, a well-known parameter in statistics, is formally defined as the third normalized moment

$$Sk_\zeta = \frac{\mathbf{E}\left[\zeta^3\left(t\right)\right]}{\mathbf{E}\left[\zeta^2\left(t\right)\right]^{3/2}} = \frac{\mu_3}{\sigma^3} \tag{A.2}$$

where $\mathbf{E}$ is the expected value operator. The time series of the flow velocity shown in Figure A.1a is representative for a shoaling wave where the maximum positive velocity is larger than the maximum negative velocity due to the timing of the phases

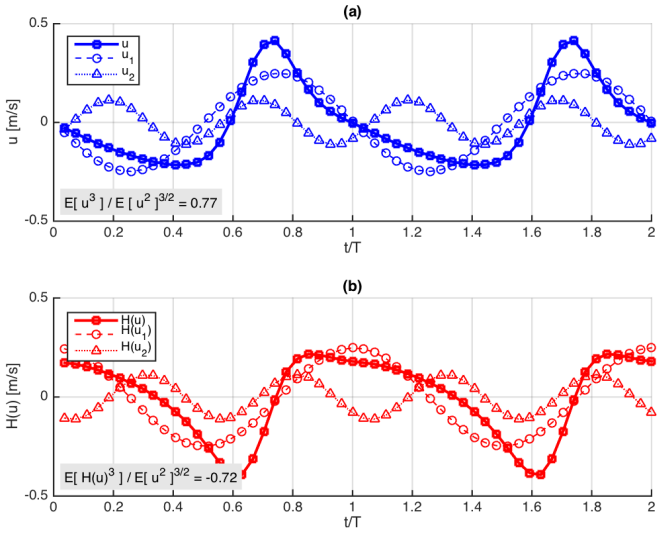

Figure A.1: Wave skewness and asymmetry.

of the higher harmonics (e.g. u_2) with respect to the first harmonic (u_1). This fact will result in a third moment that is larger than zero ($\mathbf{E}\left[u^3\left(t\right)\right] > 0$).

Besides the skewed shape feature, the time series exhibits a pitched forward shape (or sawtooth shape). This shape feature is quantified by the asymmetry parameter and determined by the third normalized moment of the Hilbert transform of the time series

$$As_\zeta = \frac{\mathbf{E}\left[\mathcal{H}\{\zeta\left(t\right)\}^3\right]}{\mathbf{E}\left[\zeta^2\left(t\right)\right]^{3/2}} = \frac{\mathbf{E}\left[\mathcal{H}\{\zeta\left(t\right)\}^3\right]}{\sigma^3} \tag{A.3}$$

where $\mathcal{H}$ is the Hilbert transform operator. The Hilbert transformation shifts the harmonics by $-\pi/2$ which produces a time series $\mathcal{H}\left[\zeta\left(t\right)\right]$ of similar variance where the minimum and maximum are located at the maximum and minimum slope of $\zeta\left(t\right)$, respectively. [1] The Hilbert transform of $u(t)$ is shown in Figure A.1b. The timing of the phases of the transformed harmonics (i.e. $\mathcal{H}\left[u_1\right]$ and $\mathcal{H}\left[u_2\right]$) leads to larger negative values of $\mathcal{H}\left[u\right]$ than positive values. Consequently, the third moment of the transformed time series is smaller than zero ($\mathbf{E}\left[\mathcal{H}\{\zeta\left(t\right)\}^3\right] < 0$). Therefore, pitched forward shapes are associated with negative asymmetry values. Note that in order for waves to be skewed and asymmetric there needs to be significant energy in the higher harmonics. However, the phases of the harmonics determine the ratio of skewness to asymmetry.

[1] To some extend, the Hilbert transform is similar to the derivative of the time series, i.e. $\mathcal{H}\left[\cos(\omega t)\right] = \sin(\omega t)$ and $\frac{d}{dt}\cos(\omega t) = -\omega\sin(\omega t)$, however, there is a ω and sign difference in amplitude.

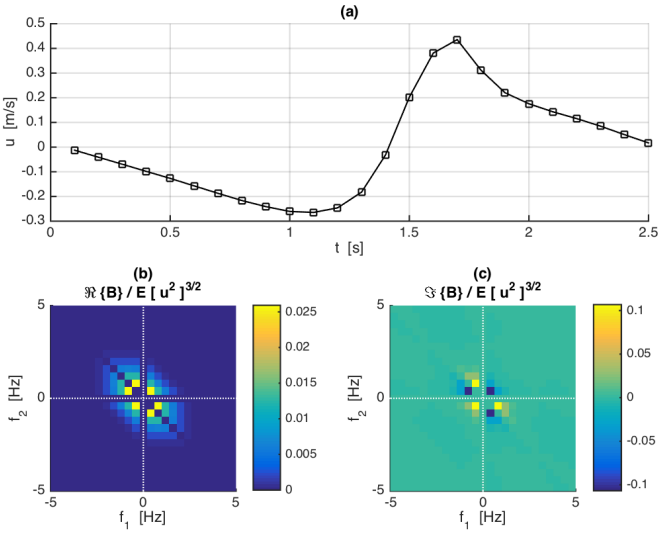

Figure A.2: Bispectral analysis.

A.2. THE BISPECTRUM

The wave skewness and asymmetry are properties that can be derived from the bispectrum which is determined by the Fourier coefficients A_n and A_n^* of Equation A.1. The Fourier coefficients can be calculated using the FFT technique on the time series of $\zeta(t)$. The FFT returns N number of Fourier components that includes the DC component. A signal sampled with frequency F_s is limited by the Nyquist frequency $f_N = F_s/2$. The Fourier components will have frequencies that range from $-f_N \leq f \leq f_N$ with discrete intervals of $\Delta f = F_s/N$. [2]

The power spectrum is defined as

$$P(f_k) = \frac{1}{2}\mathbf{E}\left[A(f_k)A^*(f_k)\right] . \tag{A.4}$$

Taking the sum over all frequencies is equal to the variance of $\zeta(t)$

$$\sum_n P(f_n) = \operatorname{var}\zeta(t) = \mathbf{E}\left[\zeta^2(t)\right] = \sigma^2 . \tag{A.5}$$

The power bispectrum is defined as (Elgar and Guza, 1985; Hasselman et al., 1963)

$$B(f_k, f_j) = \mathbf{E}\left[A(f_k)A(f_j)A^*(f_k + f_j)\right] . \tag{A.6}$$

[2] In practice, typically the power of two is chosen for the length of the time series, e.g. $2^{10} = 1024$, thus the FFT will return an even number of frequency components that includes the zero-frequency component. When the spectrum is centered around the zero-frequency component, the zero-frequency component will be the 513th frequency component of the array. As a consequence, the Nyquist frequency exists only on the negative axis and the maximum positive frequency is equal to $f_N - \Delta f$. A workaround to get the complete frequency range from $-f_N \leq f \leq f_N$ is adding the discrete frequency f_N at the expense of energy preservation.

A

The domain of the bispectrum in the (f_1, f_2)-space has the shape of a hexagon (easily identified in Figure A.2 b) and is defined by

$$-f_N \leq f_1,\, f_2 \leq f_N \text{ and } -f_N \leq f_1 + f_2 \leq f_N\,. \tag{A.7}$$

The sum of the real part of the bispectrum is equal to the third moment of the time series of $\zeta(t)$

$$\mathbf{E}\left[\zeta^3(t)\right] = \sum_n \sum_l \Re\{B(f_n, f_l)\}\,. \tag{A.8}$$

Due to the symmetry relations

$$B(f_1, f_2) = B^*(-f_2, f_1 + f_2) = B^*(-f_1, f_1 + f_2)\,, \tag{A.9}$$

the real part of the bispectrum can be described by its values within a triangle in the (f_1, f_2)-space with vertices at $(f_1 = 0, f_2 = 0)$, $(f_1 = f_N/2, f_2 = f_N/2)$ and $(f_1 = f_N, f_1 = 0)$. Therefore, the skewness Sk of the time series $\zeta(t)$ can be derived by considering the part below the diagonal of the first quarter twelve times and the diagonal of the first quarter six times

$$Sk_\zeta = \left[12 \sum_n \sum_l \Re\{B(f_n, f_l)\} + 6 \sum_n \Re\{B(f_n, f_n)\}\right] \Big/ \sigma^3\,, \tag{A.10}$$

where $n > l$. Furthermore, the bispectrum of $\mathcal{H}[\zeta(t)]$ is equal to $-i$ times the bispectrum of $\zeta(t)$. This implies that the asymmetry As of the time series $\zeta(t)$ can be derived from the imaginary part enclosed by the triangle

$$As_\zeta = \left[12 \sum_n \sum_l \Im\{B(f_n, f_l)\} + 6 \sum_n \Im\{B(f_n, f_n)\}\right] \Big/ \sigma^3\,. \tag{A.11}$$

The normalized sum of the bispectrum can than be given by

$$B_\zeta = Sk_\zeta + i\, As_\zeta\,. \tag{A.12}$$

Note that when the frequency specification is omitted, the symbol B represents the normalized sum of the bispectrum; a possible subscript denotes the symbol of the time series.

Since the bispectrum is complex it can be written as [3]

$$B(f_1, f_2) = |B(f_1, f_2)| \exp\{-i\beta(f_1, f_2)\}\,, \tag{A.13}$$

[3] A complex number $z = x + iy$ can graphically be represented as a point where the real part ($\Re\{z\} = x$) is represented by the horizontal axis and the imaginary part ($\Im\{z\} = y$) by the vertical axis. The length of the connection from the axes origin to point z is called the amplitude (or modulus) and is equal to $|z| = \sqrt{x^2 + y^2}$ (Pythagoras' theorem). The angle enclosed by this connection and the x-axis is called the argument and equal to $\alpha = \arctan \frac{y}{x}$. This implies that $z = |z|(\cos\alpha + i \sin\alpha)$. Using Euler's formula, $z = |z| \exp\{i\alpha\}$.

where the biphase $\beta\left(f_1, f_2\right)$ is given by

$$\beta\left(f_1, f_2\right) = \arctan\left[\frac{\Im\{B\left(f_1, f_2\right)\}}{\Re\{B\left(f_1, f_2\right)\}}\right] . \tag{A.14}$$

Similarly, the Fourier coefficients A_n can be written as

$$A_n = |A_n| \exp\left\{-i\theta_n\right\} \tag{A.15}$$

where $|A_n|$ is the amplitude and θ_n is the phase of the frequency component f_n. The relation between the biphase and the corresponding phases is given by (Kim et al., 1980)

$$\beta(f_i, f_j) = \theta\left(f_i\right) + \theta\left(f_j\right) - \theta\left(f_i + f_j\right) . \tag{A.16}$$

The biamplitude and biphase can also be expressed as aggregated parameters for the complete time series (i.e. considering all frequencies). From Equation A.12 it follows that the normalized biamplitude and biphase are given respectively by

$$|B_\zeta| = \sqrt{Sk_\zeta^2 + As_\zeta^2}\,, \tag{A.17}$$

$$\beta_\zeta = \arctan\left[\frac{As_\zeta}{Sk_\zeta}\right] . \tag{A.18}$$

A.3. Description of a waveform

Based on the work of Drake and Calantoni (2001), Abreu et al. (2010) defined waveforms described by the function

$$u(t) = \Im\left\{U_1 \sum_{n=1}^{N} b^{n-1} \exp i[n\omega_1 t + (n-1)\,\Phi]\right\} \tag{A.19}$$

where Φ is the so-called waveform parameter and n is the harmonic index. Note that Eq. A.19 is the imaginary part of the complex waveform that described a sinus. Often the real part is chosen which describes a series of cosines. When a signal is described by Equation A.19, the waveform parameter is equal to the biphase with the exception of a sign change

$$\beta\left(f_i, f_j\right) = -\Phi\ . \tag{A.20}$$

When we let the waveform parameter be frequency dependent Φ_n (subscript indicates the harmonic index), the biphase and the waveform parameter are related through

$$\beta(\omega_i, \omega_j) = (i-1)\Phi_i + (j-1)\Phi_j - (i+j-1)\Phi_{i+j}\ . \tag{A.21}$$

Abreu et al. (2010) showed that by using geometric series with $N = \infty$, Equation A.19 can be exactly given by

$$u(t) = f\frac{\sin\omega t - b\sin\Phi}{1 + b^2 - 2b\cos\left(\omega t - \Phi\right)} \tag{A.22}$$

where f ensures normalization. Building on the findings of Abreu et al. (2010), Malarkey and Davies (2012) showed that, also by using geometric series with $N = \infty$, the skewness and asymmetry of Equation A.19 can be expressed as

$$Sk = \frac{3b \sin \Phi}{\sqrt{2\,(1 - b^2)}}\,, \tag{A.23}$$

$$As = \frac{3b \cos \Phi}{\sqrt{2\,(1 - b^2)}}\,. \tag{A.24}$$

Furthermore, when these expression of Sk and As are substituted in the equation for the aggregated normalized biamplitude $|B|$, Equation. A.17, we can express b as a function of $|B|$

$$b^2 = \frac{2|B|^2}{9 + 2|B|^2}\,. \tag{A.25}$$

B

The power of velocity

The effect when the velocity is raised to the power of α becomes apparent when we expand the term $u|u|^{\alpha-1}$ with a Fourier cosine series (see also Dean and Dalrymple, 1991, Section 5.6)

$$u|u|^{\alpha-1} = a_0 + \sum_{n=1}^{\infty} a_n \cos n\omega t \tag{B.1}$$

Evaluating the coefficients reveals that the even coefficients $(a_0, a_2, a_4 \ldots)$ are zero and the odd coefficients $(a_1, a_3, a_5 \ldots)$ are nonzero. The ratio of a_3/a_1 depends on α and can be found numerically.

C

Duck94 field experiment

In 1994 the Duck94 field experiment was carried out at the U.S. Army Corps of Engineer's Field Research Facility (FRF) near Duck, North Carolina, US. During the experiment a single bar profile developed where the bar crest migrated shorewards from 22 to 27 September while the bathymetry was relatively long-shore uniform (Gallagher et al., 1998; Ruessink et al., 2001). The beach is characterized by sand with median grain diameter of $200 \pm 50\,\mu m$ and a tidal range in the order of 1 m.

A pressure sensor array at 8 m depth captured the directional wave spectra. There was a tide station located at the seaward end of the FRF pier. The overall bottom topography was regularly (interval of a few days) measured with the Coastal Research Amphibious Buggy (CRAB) that drove cross-shore transects. A cross-shore array extended over the single bar profile consisting of co-located sonar altimeters, pressure sensors, and current meters. These data were sampled at 2 Hertz.

Sonar `s13` was located on the shoreward side of the bar crest. Here, the overall bed level increased 0.5 m. The bed level changes over the concerning period showed two type of positive trends. The first trend was from 22 to 25 September where the bed level change was consistently positive and eventually tapered off. The second trend started on 26 September and had significant diurnal oscillations that included positive and negative bed level changes.

Sonar `s15` was located on the seaward side of the bar crest. Here, the overall bed level decreased 0.2 m. Similar to sonar `s13`, the bed level changes tapered off towards 25 September and started again on 26 September. Contrary to sonar `s13`, only negative bed level changes were observed.

Two successive wave events with normal incident waves can be identified from the directional wave spectra data. The first event was characterized by a mixed sea with a significant wave height of 0.8 m, a peak period of 8 to 10 s and died out on the 25th of September. The following day a new swell arrived that was relatively narrow-banded with a significant wave height of 0.8 to 1 m and a peak period of 11 to 15 s.

The diurnal oscillations of the flow velocity and the bed level at the shoreward

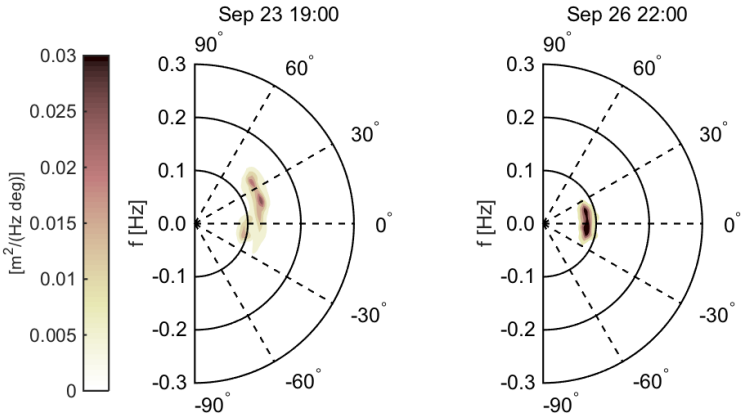

Figure C.1: Duck94 directional wave spectra.

side of the bar crest during the second wave event were synced with the water levels of the tide. Higher (lower) water levels corresponded with smaller (larger) offshore velocities and higher (lower) bed levels. The bed level at sonar `s13` increased consistently during the high waters. Moreover, most of the accretion at `s13` occurred over a total of six high waters (referred to as A-F in Fig C.3).

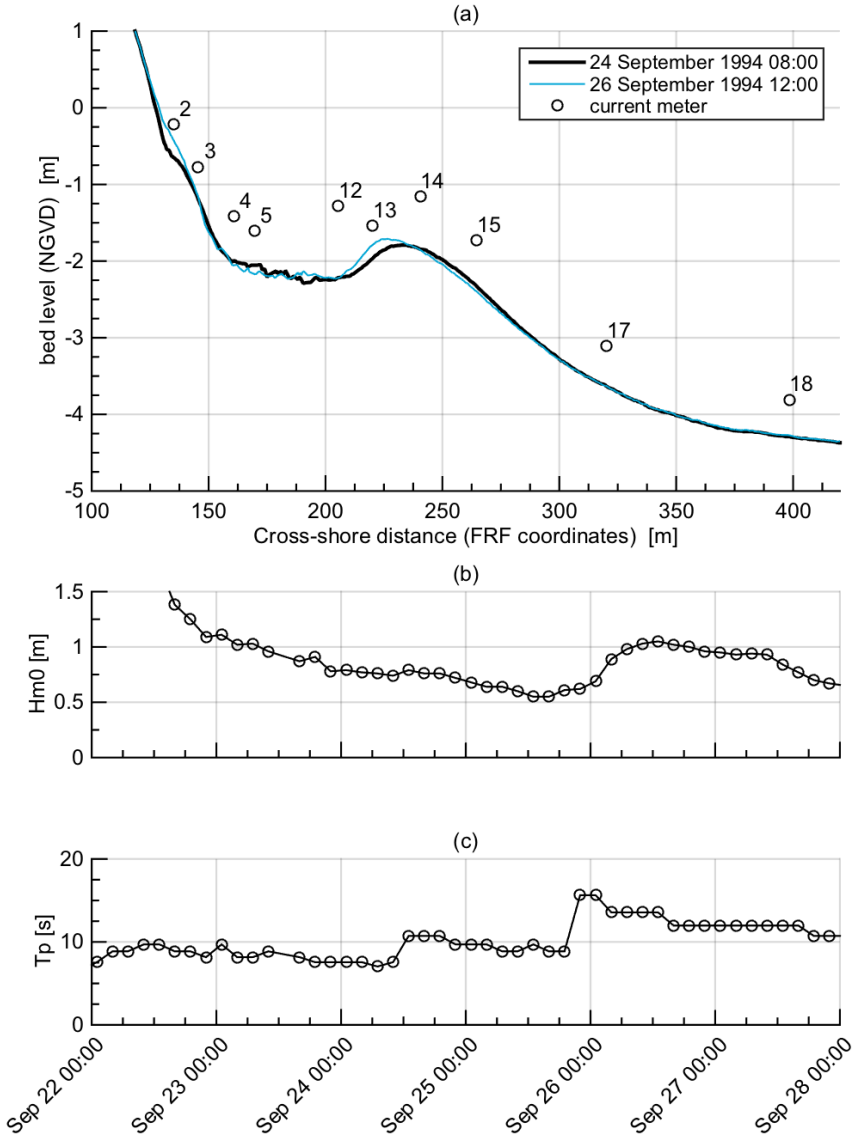

Figure C.2: Brief overview of the Duck94 experiment. (a) Bottom profiles derived from CRAB measurements and locations of current meters that had co-located sonars. (b) Significant wave height. (c) Peak wave period.

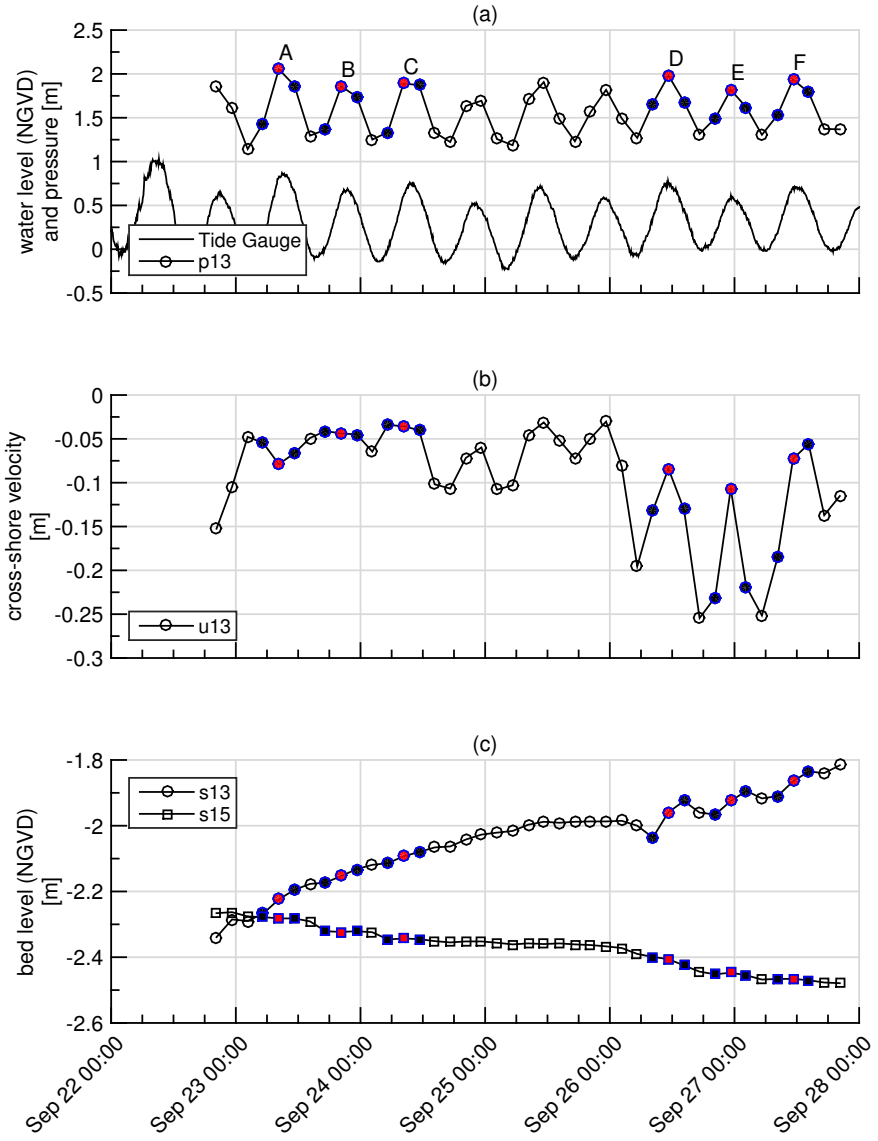

Figure C.3: Time series during Duck 94 of (a) pressure, (b) velocity and (c) bed level

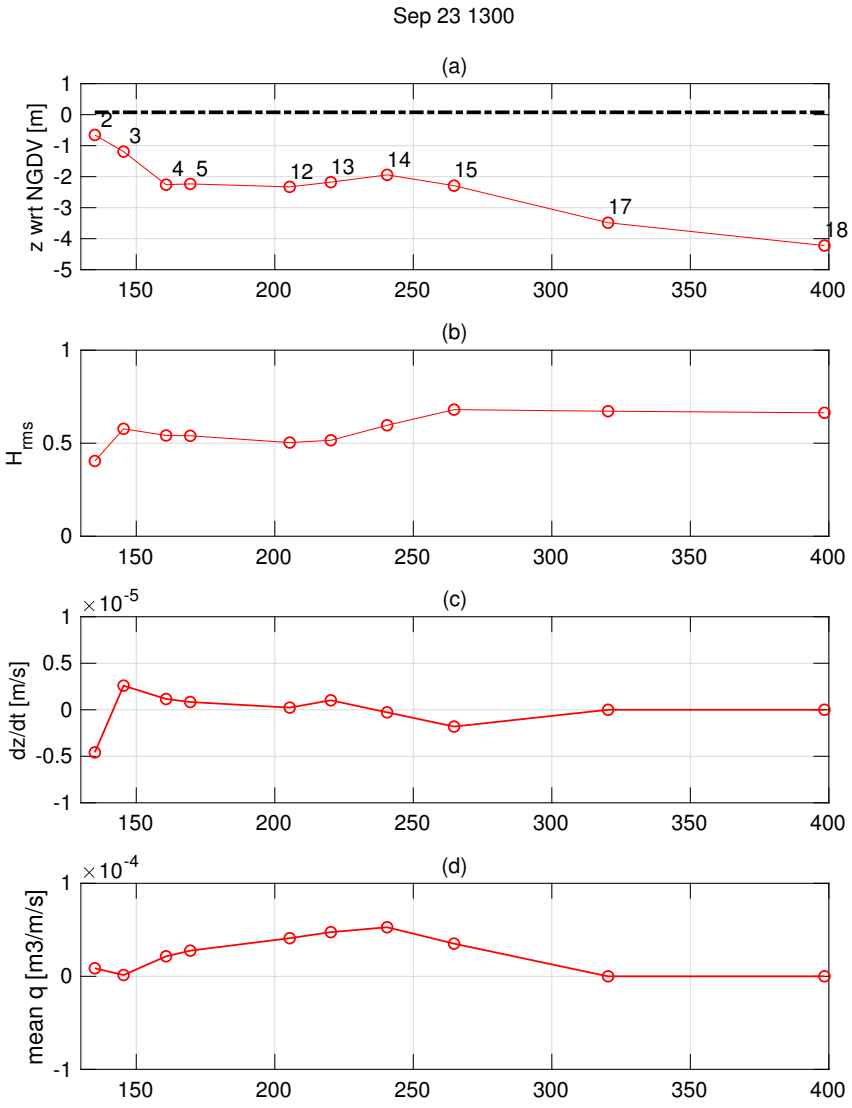

Figure C.4: DUCK94 23 September 13:00 (low tide)

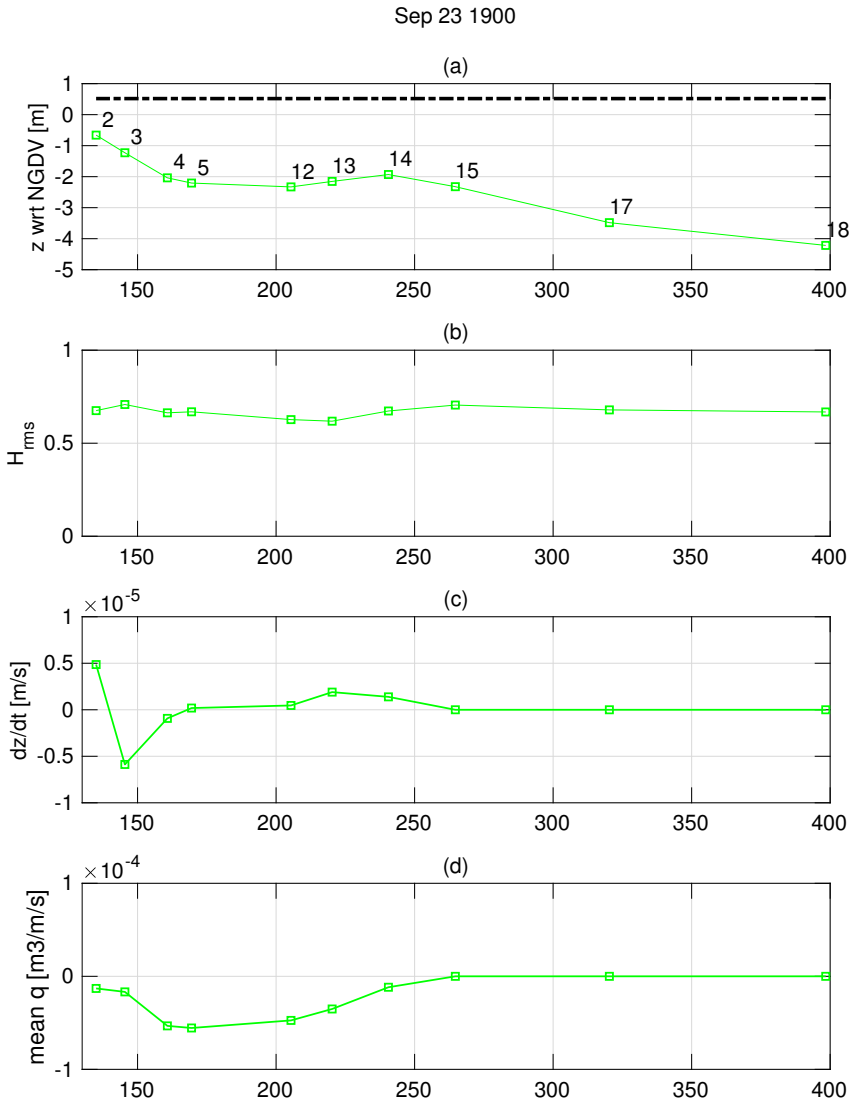

Figure C.5: DUCK94 23 September 19:00 (high tide)

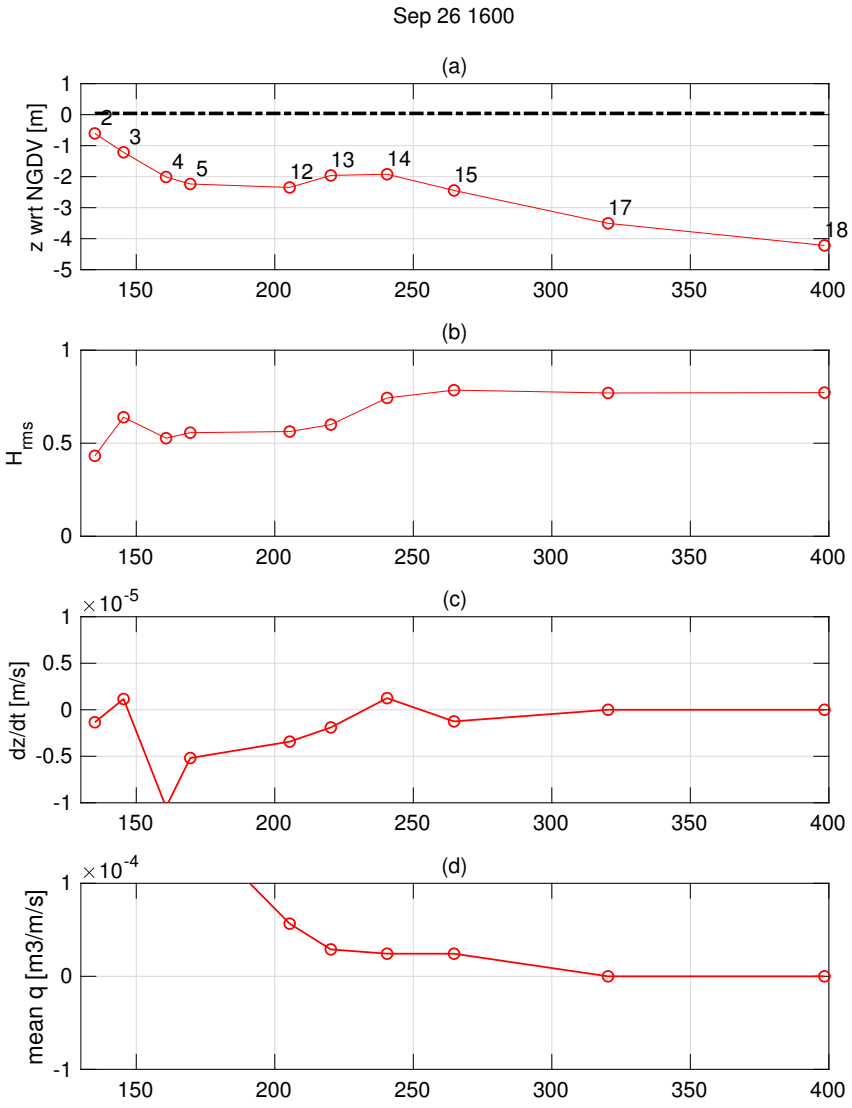

Figure C.6: DUCK94 26 September 16:00 (low tide)

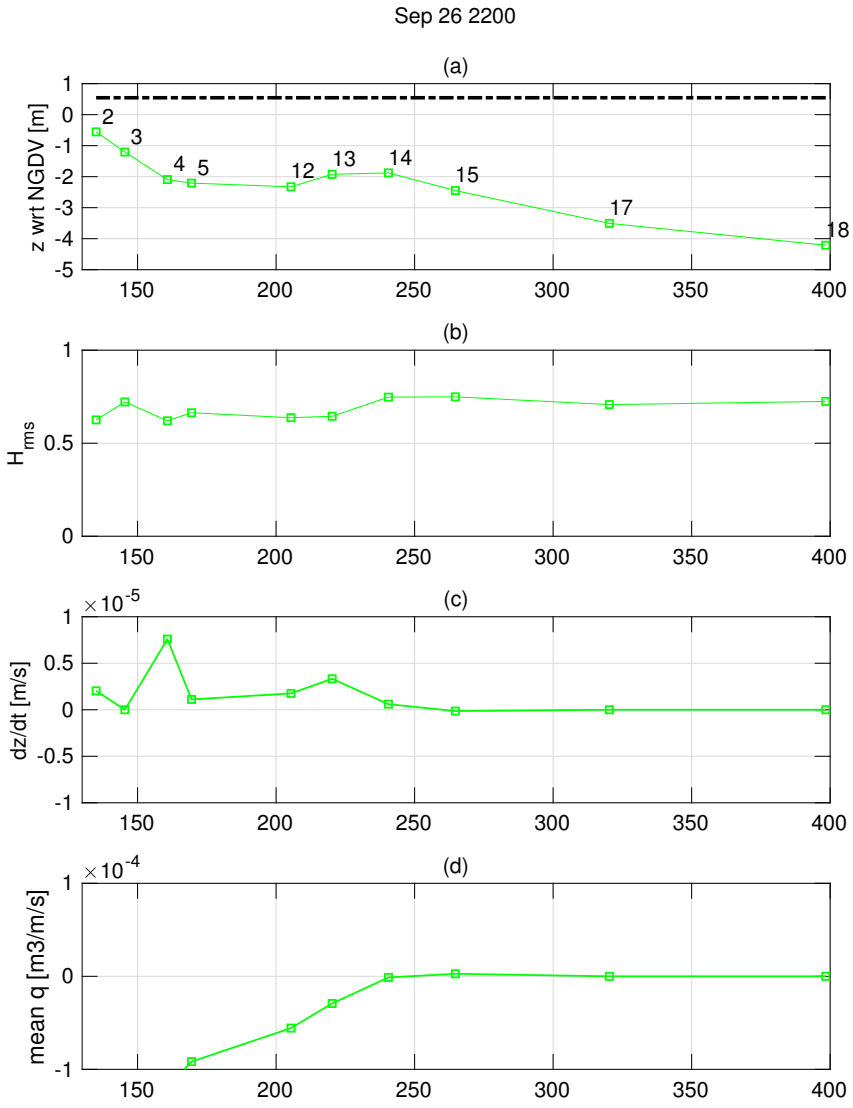

Figure C.7: DUCK94 26 September 22:00 (high tide)

References

Abreu, T., Michallet, H., Silva, P. A., Sancho, F., Ruessink, B., et al. (2013). Bed shear stress under skewed and asymmetric oscillatory flows. *Coastal Engineering*, 73:1–10.

Abreu, T., Silva, P. A., Sancho, F., and Temperville, A. (2010). Analytical approximate wave form for asymmetric waves. *Coastal Engineering*, 57(7):656–667.

Akhavan, R., Kamm, R. D., and Shapiro, A. H. (1991). An investigation of transition to turbulence in bounded oscillatory stokes flows part 1. experiments. *Journal of Fluid Mechanics*, 225:395–422.

Aubrey, D. G. (1979). Seasonal patterns of onshore/offshore sediment movement. *Journal of Geophysical Research: Oceans*, 84(C10):6347–6354.

Bagnold, R. (1966). An approach to the sediment transport problem. *General Physics Geological Survey, Prof. paper*.

Bailard, J. A. (1981). An energetics total load sediment transport model for a plane sloping beach. *Journal of Geophysical Research: Oceans (1978–2012)*, 86(C11):10938–10954.

Bailard, J. A. (1982). Modeling on-offshore sediment transport in the surfzone. *Coastal Engineering Proceedings*, 1(18).

Bailard, J. A. and Inman, D. L. (1981). An energetics bedload model for a plane sloping beach: local transport. *Journal of Geophysical Research: Oceans (1978–2012)*, 86(C3):2035–2043.

Batchelor, G. (1967). An introduction to fluid dynamics.

Batchelor, G. K. (2000). *An Introduction to Fluid Dynamics*. Cambridge University Press.

Battjes, J. and Janssen, J. (1978). Energy loss and set-up due to breaking of random waves. *Coastal Engineering Proceedings*, 1(16).

Beji, S. and Battjes, J. (1993). Experimental investigation of wave propagation over a bar. *Coastal Engineering*, 19(1):151–162.

Berni, C., Barthélemy, E., and Michallet, H. (2013a). Surf zone cross-shore boundary layer velocity asymmetry and skewness: An experimental study on a mobile bed. *Journal of Geophysical Research: Oceans*, 118(4):2188–2200.

Berni, C., Barthélemy, E., and Michallet, H. (2013b). Surf zone cross-shore boundary layer velocity asymmetry and skewness: an experimental study on a mobile bed. *Journal of Geophysical Research: Oceans*, pages n/a–n/a.

Boers, M. (2005). Surf zone turbulence.

Bowen, A. (1980). Simple models of nearshore sedimentation. *Beach profiles and longshore bars. The Coastline of Canada, ed. SB McCann. Geological Survey of*, pages 1–11.

Calantoni, J. and Puleo, J. A. (2006). Role of pressure gradients in sheet flow of coarse sediments under sawtooth waves. *Journal of Geophysical Research*, 111:10 PP.

Carstensen, S., Sumer, B. M., and FredsøE, J. (2010). Coherent structures in wave boundary layers. part 1. oscillatory motion. *Journal of Fluid Mechanics*, 646:169.

Chassagneux, F. X. and Hurther, D. (2014). Wave bottom boundary layer processes below irregular surfzone breaking waves with light-weight sheet flow particle transport. *Journal of Geophysical Research: Oceans*, 119(3):1668–1690.

Dalrymple, R. A., MacMahan, J. H., Reniers, A. J., and Nelko, V. (2011). Rip currents. *Annual Review of Fluid Mechanics*, 43:551–581.

De Vriend, H. and Stive, M. (1987). Quasi-3d modelling of nearshore currents. *Coastal Engineering*, 11(5-6):565–601.

Dean, R. G. and Dalrymple, R. A. (1991). *Water wave mechanics for engineers and scientists*, volume 2. World Scientific Publishing Co Inc.

Doering, J. and Bowen, A. (1995). Parametrization of orbital velocity asymmetries of shoaling and breaking waves using bispectral analysis. *Coastal Engineering*, 26(1):15–33.

Dohmen-Janssen, C. M. and Hanes, D. M. (2002). Sheet flow dynamics under monochromatic nonbreaking waves. *Journal of Geophysical Research: Oceans*, 107(C10).

Drake, T. G. and Calantoni, J. (2001). Discrete particle model for sheet flow sediment transport in the nearshore. *Journal of Geophysical Research*, 106(C9):868.

Dubarbier, B., Castelle, B., Marieu, V., and Ruessink, G. (2015). Process-based modeling of cross-shore sandbar behavior. *Coastal Engineering*, 95:35–50.

Duncan, J. (1981). An experimental investigation of breaking waves produced by a towed hydrofoil. *Proc. R. Soc. Lond. A*, 377(1770):331–348.

Dyhr-Nielsen, M. and Sorensen, T. (1970). Sand transport phenomena on coasts with bars. pages 855–865. ASCE.

Elgar, S., Gallagher, E. L., and Guza, R. T. (2001). Nearshore sandbar migration. *Journal of Geophysical Research: Oceans*, 106(C6):11623–11627.

Elgar, S. and Guza, R. (1985). Observations of bispectra of shoaling surface gravity waves. *Journal of Fluid Mechanics*, 161:425–448.

Fernández-Mora, A., Calvete, D., Falqués, A., and Swart, H. (2015). Onshore sandbar migration in the surf zone: New insights into the wave-induced sediment transport mechanisms. *Geophysical research letters*, 42(8):2869–2877.

Flores, N. Z. and Sleath, J. F. (1998a). Mobile layer in oscillatory sheet flow. *Journal of Geophysical Research: Oceans*, 103(C6):12783–12793.

Flores, N. Z. and Sleath, J. F. A. (1998b). Mobile layer in oscillatory sheet flow. *Journal of Geophysical Research*, 103:12783–12793.

Foster, D., Beach, R., and Holman, R. (2000). Field observations of the wave bottom boundary layer. *Journal of Geophysical Research: Oceans*, 105(C8):19631–19647.

Foster, D., Holman, R., and Beach, R. (1994). Sediment suspension events and shear instabilities in the bottom boundary layer. In *Proceedings Coastal Dynamics '94*, pages 712–726.

Foster, D. L., Bowen, A. J., Holman, R. A., and Natoo, P. (2006). Field evidence of pressure gradient induced incipient motion. *Journal of Geophysical Research*, 111.

Fredsøe, J. and Deigaard, R. (1992). *Mechanics of coastal sediment transport*. World Scientific.

Gallagher, E., Elgar, S., and Guza, R. (1998). Observations of sand bar evolution on a natural beach. *Journal of Geophysical Research*, 103(C2):3203–3215.

Hallegatte, S., Green, C., Nicholls, R. J., and Corfee-Morlot, J. (2013). Future flood losses in major coastal cities. *Nature climate change*, 3(9):802.

Hasselman, K., Munk, W., and MacDonald, G. (1963). Bispectra of ocean waves. *Time Series Analysis*, pages 125–139.

Henderson, S. M., Allen, J. S., and Newberger, P. A. (2004). Nearshore sandbar migration predicted by an eddy-diffusive boundary layer model. *Journal of Geophysical Research*, 109:15 PP.

Henriquez, M., Reniers, A., Ruessink, B., and Stive, M. (2014). Piv measurements of the bottom boundary layer under nonlinear surface waves. *Coastal Engineering*, 94:33–46.

Henriquez, M., Reniers, A., Ruessink, G., and Stive, M. (2011). Wave boundary layer hydrodynamics during onshore bar migration. *Coastal Engineering Proceedings*, 1(32):2.

Henriquez, M., Stive, M., Reniers, A., Ruessink, B., Stanton, T., and Foster, D. (2008). On the scaling of sediment transport in the nearshore. In *International Conference on the Application of Physical Modelling to Port and Coastal Protection (Coastlab 2008 Conference)*, pages 193–204.

Hillen, R. and Roelse, P. (1995). Dynamic preservation of the coastline in the netherlands. *Journal of Coastal Conservation*, 1(1):17–28.

Hinze, J. (1975). Turbulence mcgraw-hill. *New York*, 218.

Hoefel, F. and Elgar, S. (2003). Wave-induced sediment transport and sandbar migration. *Science*, 299(5614):1885–1887.

Hofland, B. (2005). Rock and roll: Turbulence-induced damage to granular bed protections.

Hofland, B. and Booij, R. (2004). Measuring the flow structures that initiate stone movement. In *Proceedings of River Flow*.

Holmedal, L. E. and Myrhaug, D. (2009). Wave-induced steady streaming, mass transport and net sediment transport in rough turbulent ocean bottom boundary layers. *Continental Shelf Research*, 29(7):911–926.

Hsu, T.-J., Elgar, S., and Guza, R. (2006). Wave-induced sediment transport and onshore sandbar migration. *Coastal Engineering*, 53(10):817–824.

Hsu, T.-J. and Hanes, D. M. (2004). Effects of wave shape on sheet flow sediment transport. *Journal of Geophysical Research*, 109:15 PP.

Hughes, S. A. (1993). *Physical models and laboratory techniques in coastal engineering*. World Scientific.

Jackson, P. (1981). On the displacement height in the logarithmic velocity profile. *Journal of Fluid Mechanics*, 111:15–25.

Jensen, B. L., Sumer, B. M., and Fredsøe, J. (1989). Turbulent oscillatory boundary layers at high reynolds numbers. *Journal of Fluid Mechanics*, 206:265.

Jeong, J. and Hussain, F. (1995). On the identification of a vortex. *Journal of Fluid Mechanics*, 285(-1):69.

Jonsson, I. (1966). Wave boundary layers and friction factors. In *Proceedings of the 10th International Conference on Coastal Engineering*, pages 127–148.

Jonsson, I. G. (1980). A new approach to oscillatory rough turbulent boundary layers. *Ocean Engineering*, 7(1):109–152.

Jonsson, I. G. and Carlsen, N. A. (1976). Experimental and theoretical investigations in an oscillatory turbulent boundary layer. *Journal of Hydraulic Research*, 14(1):45–60.

Kamphuis, J. W. (1975). Friction factor under oscillatory waves. *Journal of the Waterways, Harbors and Coastal Engineering Division*, 101(2):135–144.

Kim, Y., Beall, J., Powers, E., and Miksad, R. (1980). Bispectrum and nonlinear wave coupling. *Physics of Fluids (1958-1988)*, 23(2):258–263.

Koehl, M. A. R. (1982). The Interaction of Moving Water and Sessile Organisms. *Sci Am*, 247(6):124–134.

Kranenburg, W. M., Ribberink, J. S., Schretlen, J. J. L. M., and Uittenbogaard, R. E. (2013). Sand transport beneath waves: The role of progressive wave streaming and other free surface effects. *Journal of Geophysical Research: Earth Surface*, pages n/a–n/a.

Kranenburg, W. M., Ribberink, J. S., Uittenbogaard, R. E., and Hulscher, S. J. (2012). Net currents in the wave bottom boundary layer: On waveshape streaming and progressive wave streaming. *Journal of Geophysical Research: Earth Surface*, 117(F3).

Kuriyama, Y. (2002). Medium-term bar behavior and associated sediment transport at hasaki, japan. *Journal of Geophysical Research: Oceans*, 107(C9):15–1–15–12.

Lara, J., Cowen, E., and Sou, I. (2002). A depth-of-field limited particle image velocimetry technique applied to oscillatory boundary layer flow over a porous bed. *Experiments in fluids*, 33(1):47–53.

Launder, B. E. and Spalding, D. B. (1974). The numerical computation of turbulent flows. *Computer methods in applied mechanics and engineering*, 3(2):269–289.

Lofquist, K. (1986). Drag on naturally rippled beds under oscillatory flows. misc. Technical report, Paper CERC-86-13, US Army Corps of Engineers.

Longuet-Higgins, M. S. (1953). Mass transport in water waves. *Philosophical Transactions of the Royal Society of London. Series A, Mathematical and Physical Sciences*, 245(903):535 –581.

Madsen, O. (1974). Stability of a sand bed under breaking waves. In *Proceedings of the 14th International Conference on Coastal Engineering*, volume 14, page 776.

Malarkey, J. and Davies, A. (2012). Free-stream velocity descriptions under waves with skewness and asymmetry. *Coastal Engineering*, 68:78–95.

Meyer-Peter, E. and Müller, R. (1948). Formulas for bed-load transport. IAHR.

Mirfenderesk, H. and Young, I. R. (2003). Direct measurements of the bottom friction factor beneath surface gravity waves. *Applied Ocean Research*, 25:269–287.

Nichols, C. S. and Foster, D. L. (2007). Full-scale observations of wave-induced vortex generation over a rippled bed. *Journal of Geophysical Research*, 112:17 PP.

Nielsen, P. (1992). *Coastal bottom boundary layers and sediment transport*, volume 4. World Scientific Publishing Co Inc.

Nielsen, P. (2002). Shear stress and sediment transport calculations for swash zone modelling. *Coastal Engineering*, 45(1):53–60.

Nikora, V., Goring, D., McEwan, I., and Griffiths, G. (2001). Spatially averaged open-channel flow over rough bed. *Journal of Hydraulic Engineering*, 127(2):123–133.

Phillips, O. (1977). *The dynamics of the upper ocean.* Cambridge University Press, Cambridge ;;New York, 2d ed. edition.

Reniers, A., Thornton, E., Stanton, T., and Roelvink, J. (2004a). Vertical flow structure during sandy duck: observations and modeling. *Coastal Engineering*, 51(3):237–260.

Reniers, A. J. H. M., Battjes, J. A., Falqués, A., and Huntley, D. A. (1997). A laboratory study on the shear instability of longshore currents. *Journal of Geophysical Research*, 102:8597–8609.

Reniers, A. J. H. M., Roelvink, J. A., and Thornton, E. B. (2004b). Morphodynamic modeling of an embayed beach under wave group forcing. *Journal of Geophysical Research: Oceans*, 109(C1):n/a–n/a.

Ribberink, J. (1995). Sheet flow and suspension of sand in oscillatory boundary layers. *Coastal Engineering*, 25(3-4):205–225.

Ribberink, J. (1998). Bed-load transport for steady flows and unsteady oscillatory flows. *Coastal Engineering*, 34(1-2):59–82.

Ribberink, J. S. and Al-Salem, A. A. (1995). Sheet flow and suspension of sand in oscillatory boundary layers. *Coastal Engineering*, 25(3-4):205–225.

Ribberink, J. S. and Chen, Z. W. (1993). Sediment transport of fine sand under asymmetric oscillatory flow. Technical Report H840, Part VII, January, Delft Hydraulics.

Ribberink, J. S., Dohmen-Janssen, C. M., Hanes, D. M., McLean, S. R., and Vincent, C. (2000). Near-bed sand transport mechanisms under waves:. pages 254–254. ASCE.

Rienecker, M. and Fenton, J. (1981). A fourier approximation method for steady water waves. *Journal of Fluid Mechanics*, 104:119–137.

Rodi, W. (1987). Examples of calculation methods for flow and mixing in stratified fluids. *Journal of Geophysical Research: Oceans*, 92(C5):5305–5328.

Roelvink, J. and Reniers, A. (1994). Upgrading of a quasi-3d hydrodynamic model. In *Abstracts-in-depth, MAST G8-M overall workshop, Gregynog.*

Roelvink, J. A. and Reniers, A. (1995). *LIP 11D Delta Flume experiments: a dataset for profile model validation*. WL/Delft Hydraulics.

Roelvink, J. A. and Stive, M. J. F. (1989). Bar-generating cross-shore flow mechanisms on a beach. *Journal of Geophysical Research*, 94(C4):4785–4800.

Ruessink, B., Kuriyama, Y., Reniers, A., Roelvink, J., and Walstra, D. (2007a). Modeling cross-shore sandbar behavior on the timescale of weeks. *Journal of Geophysical Research: Earth Surface*, 112(F3).

Ruessink, B., Ramaekers, G., and Van Rijn, L. (2012a). On the parameterization of the free-stream non-linear wave orbital motion in nearshore morphodynamic models. *Coastal Engineering*, 65:56–63.

Ruessink, B., Van den Berg, T., and Van Rijn, L. (2009). Modeling sediment transport beneath skewed asymmetric waves above a plane bed. *Journal of Geophysical Research: Oceans*, 114(C11).

Ruessink, B., van Enckevort, I., Kingston, K., and Davidson, M. (2000). Analysis of observed two- and three-dimensional nearshore bar behaviour. *Marine Geology*, 169(1–2):161–183.

Ruessink, B. G., Kuriyama, Y., Reniers, A. J. H. M., Roelvink, J. A., and Walstra, D. J. R. (2007b). Modeling cross-shore sandbar behavior on the timescale of weeks. *Journal of Geophysical Research*, 112(F3).

Ruessink, B. G., Miles, J. R., Feddersen, F., Guza, R. T., and Elgar, S. (2001). Modeling the alongshore current on barred beaches. *Journal of Geophysical Research: Oceans*, 106(C10):22451–22463.

Ruessink, B. G., Ramaekers, G., and van Rijn, L. C. (2012b). On the parameterization of the free-stream non-linear wave orbital motion in nearshore morphodynamic models. *Coastal Engineering*, 65:56–63.

Sánchez-Arcilla, A., Cáceres, I., van Rijn, L., and Grüne, J. (2011). Revisiting mobile bed tests for beach profile dynamics. *Coastal Engineering*, 58(7):583–593.

Schlicke, E., Coleman, S., and Nikora, V. (2005). A PIV investigation into the interaction between wave motion and sediment ripples. In *4th IAHR symposium on river, coastal and estuarine morphodynamics, Urbana*, pages 4–7.

Sleath, J. (1987). Turbulent oscillatory flow over rough beds. *Journal of Fluid Mechanics*, 182:369–409.

Stive, M. J. and De Vriend, H. J. (1994). Shear stresses and mean flow in shoaling and breaking waves. *Coastal Engineering Proceedings*, 1(24).

Stokes, G. G. (1851). *On the effect of the internal friction of fluids on the motion of pendulums*, volume 9. Pitt Press.

Svendsen, I. A. (1984). Mass flux and undertow in a surf zone. *Coastal Engineering*, 8(4):347–365.

Swart, D. H. (1974). *Offshore sediment transport and equilibrium beach profiles*. PhD thesis, TU Delft, Delft University of Technology.

Terrile, E., Reniers, A., and Stive, M. (2009a). Acceleration and skewness effects on the instantaneous bed-shear stresses in shoaling waves. *Journal of Waterway, Port, Coastal, and Ocean Engineering*, 135(5):228–234.

Terrile, E., Reniers, A. J., and Stive, M. J. (2009b). Acceleration and skewness effects on the instantaneous bed-shear stresses in shoaling waves. *Journal of waterway, port, coastal, and ocean engineering*, 135(5):228–234.

Trowbridge, J. and Madsen, O. S. (1984). Turbulent wave boundary layers 2. second-order theory and mass transport. *Journal of Geophysical Research*, 89:7999–8007.

Uittenbogaard, R. and Klopman, G. (2001). Numerical simulation of wave-current driven sediment transport. In *Coastal Dynamics' 01*, pages 568–577.

van der A, D. A., O'Donoghue, T., Davies, A. G., and Ribberink, J. S. (2009). EFFECTS OF ACCELERATION SKEWNESS ON ROUGH BED OSCILLATORY BOUNDARY LAYER FLOW. In *Proceedings of the 31st International Conference on Coastal Engineering*, volume 1-5, pages 1583–1595. World Scientific Publishing Co. Pte. Ltd.

van der A, D. A., O'Donoghue, T., Davies, A. G., and Ribberink, J. S. (2011). Experimental study of the turbulent boundary layer in acceleration-skewed oscillatory flow. *Journal of fluid mechanics*, 684:251–283.

van Rijn, L. (2007). Unified view of sediment transport by currents and waves. i: Initiation of motion, bed roughness, and bed-load transport. *Journal of Hydraulic Engineering*, 133(6):649–667.

Walstra, D., Reniers, A., Ranasinghe, R., Roelvink, J., and Ruessink, B. (2012). On bar growth and decay during interannual net offshore migration. *Coastal Engineering*, 60:190–200.

Westerweel (1993). *Digital particle image velocimetry: theory and application*. Delft University Press.

Wilson, K. C. (1987). Analysis of bed-load motion at high shear stress. *Journal of Hydraulic Engineering*, 113(1):97–103.

Wright, L. and Short, A. D. (1984). Morphodynamic variability of surf zones and beaches: a synthesis. *Marine geology*, 56(1-4):93–118.

Curriculum Vitæ

Martijn Henriquez

31-01-1979	Born in Willemstad, Curaçao

Education

1991–1996	HAVO, The Stuyvesant College, Curaçao
1996–1997	VWO, The Stuyvesant College, Curaçao
1997–2004	MSc Coastal Engineering, Delft University of Technology

Employment

2005–2011	PhD researcher at Delft University of Technology
2012–2016	Postdoctoral researcher at Delft University of Technology
2017–2019	Civil engineer at TNO Caribbean, Aruba

List of selected publications

- Henriquez, M., Reniers, A. J. H. M., Ruessink, B. G., and Stive, M. (2014). PIV measurements of the bottom boundary layer under nonlinear surface waves. *Coastal Engineering*, 94:33–46.
- Rodríguez-Abudo, S., Foster, D. L. and Henriquez, M. (2013). Spatial variability of the wave bottom boundary layer over movable rippled beds. *Journal of geophysical research: oceans*, 118(7), pp.3490-3506.
- Henriquez, M., Reniers, A. J. H. M., Ruessink, B. G. and Stive, M. J. F.(2012). Vortex tubes in the wave bottom boundary layer. *NCK-days 2012*, p.143.
- Henriquez, M., Reniers, A. J. H. M., Ruessink, B. G., and Stive, M. J. F. (2011). Wave boundary layer hydrodynamics during onshore bar migration. *Coastal Engineering Proceedings*, 1(32):2.
- MacMahan, J., Brown, J., Brown, J., Thornton, E., Reniers, A. J. H. M., Stanton, T., Henriquez, M., Gallagher, E., Morrison, J., Austin, M. J. and Scott, T. M. (2010). Mean Lagrangian flow behavior on an open coast rip-channeled beach: A new perspective. *Marine Geology*, 268(1-4), pp.1-15.
- Reniers, A. J. H. M., MacMahan, J. H., Thornton, E. B., Stanton, T. P., Henriquez, M., Brown, J. W., Brown, J. A. and Gallagher, E. (2009). Surf zone surface retention on a rip-channeled beach. *Journal of Geophysical Research: Oceans*, 114(C10).
- Henriquez, M., Reniers, A. J. H. M., Ruessink, B. G., Stive, M. J. F., Stanton, T. P., and Foster, D. L. (2008). On the scaling of sediment transport in the nearshore. In *International Conference on the Application of Physical Modelling to Port and Coastal Protection (Coastlab 2008 Conference)*, Bari, Italy.